A rigorous computational framework for investigating the transmission and focusing of light in biological tissue

Jake Bewick

A dissertation submitted in partial fulfillment

of the requirements for the degree of

Doctor of Philosophy

of

University College London.

Department of Medical Physics and Biomedical Engineering

University College London

September 26, 2025

I, Jake Bewick, confirm that the work presented in this thesis is my own. Where information has been derived from other sources, I confirm that this has been indicated in the work.

Abstract

The scattering of visible and near-infrared light in biological tissue limits the penetration depth of many optical imaging modalities. Wavefront shaping offers a way to overcome this constraint by spatially modulating the incident field to generate an optical focus deep within scattering media. However, existing *in silico* approaches are either computationally prohibitive or insufficiently rigorous, limiting their ability to model wavefront shaping at experimentally relevant depths.

To address the challenge, a rigorous and efficient simulation framework has been developed by coupling the T-matrix method for calculating light propagation with discrete-particle representations of bespoke media, including biological tissue. The framework has been extensively validated and enables full-wave modelling of light propagation across ballistic, quasi-ballistic, and diffusive regimes. To demonstrate the method, scattered light propagation and focusing are simulated in and around a titanium dioxide phantom and a $\sim$1 mm thick biological tissue section.

By enabling deterministic coherent optics simulations across a range of physically relevant length scales, the computational framework presented in this thesis provides a tool that can aid the development of various techniques exploiting coherent phenomena in scattering media.

Impact Statement

This thesis presents a computational framework for simulating light propagation through bespoke scattering media. This framework is validated and applied to model wavefront shaping and other coherent phenomena. Its contributions lie at the intersection of optics, biomedical imaging, and high-performance computational modelling.

The immediate academic impact of this work is the development of a physically rigorous and computationally efficient modelling framework capable of simulating light scattering through deep tissue-like media. This advances the state of the art in optical modelling by enabling studies of light propagation at scales previously only accessible to less physically rigorous techniques.

From a translational perspective, this work supports the design and optimisation of novel imaging and therapeutic systems. In particular, the framework is applicable to emerging techniques such as photoacoustic-guided wavefront shaping, optical neuromodulation, or photodynamic therapy, where precise light delivery through scattering media is essential.

The techniques developed here may contribute to reducing experimental overheads, improving the efficiency of light-based medical technologies, and guiding new discoveries in optical wave control. As coherent imaging and therapeutic methods continue to expand in clinical and research settings, the ability to simulate and understand light–tissue interactions will become increasingly valuable.

Acknowledgements

I would like to thank my three supervisors, Jamie Guggenheim, Peter Munro, and Simon Arridge, for their support and guidance throughout the PhD. The indefatigable support of my primary supervisor, Jamie Guggenheim, has been particularly necessary over the past two (uniquely disruptive) years. I would like to thank my mother, nan, brother and wife for their tireless love. This work would not have been possible without them.

Contents

1 Introduction **17**

1.1 Motivation 17

1.2 Problem statement 19

1.3 Aims 19

1.4 Objectives 19

1.5 Report structure 20

2 Background **22**

2.1 Light propagation through biological tissue 22

2.1.1 Scattering theory 23

2.1.2 Absorption theory 25

2.1.3 Inimical effects of scattering 26

2.2 Wavefront shaping 28

2.2.1 Fundamentals of wavefront shaping 28

2.2.2 Transmission matrix theory 34

2.2.3 Optimisation of input modes 35

2.2.4 Applications of wavefront shaping 35

2.2.5 Limitations and challenges of wavefront shaping 39

2.3 Computational modelling of wavefront shaping 40

2.3.1 Advantages of computational modelling 40

2.3.2 Existing attempts to model wavefront shaping 42

2.3.3 Methods of modelling biological tissue 43

2.3.4 Requirements of a model of biological tissue to simulate wavefront shaping . . . 51
2.3.5 Methods of modelling light propagation . . . 52
2.3.6 Requirements of a model of light propagation to simulate wavefront shaping . . . 58
2.4 Chapter summary . . . 58

3 Simulating light transport using the T-matrix method 60
3.1 Background . . . 61
3.2 Model theory . . . 63
3.2.1 Constructing a system of linear equations . . . 63
3.2.2 N-sphere system . . . 67
3.2.3 Calculating the scattered field . . . 67
3.2.4 System dimensionality and numerical considerations . . . 68
3.3 Implementation . . . 70
3.3.1 T-matrix solvers . . . 70
3.3.2 Available computational hardware . . . 72
3.3.3 Placing spheres to create discrete particle volume . . . 73
3.3.4 Initial code modification . . . 75
3.3.5 Initial simulations of light propagation . . . 77
3.4 Validation . . . 85
3.4.1 Field comparison vs Mie . . . 85
3.4.2 Field comparison vs FDTD . . . 86
3.5 Chapter summary . . . 90

4 Designing T-matrix-optimised sphere-based replica turbid media 92
4.1 Background . . . 93
4.1.1 Modelling generic tissue optical properties . . . 93
4.1.2 The theory of Mie theory . . . 97
4.1.3 Mie theory and discrete particles in phantom design . . . 101
4.1.4 Optical property measurement with Inverse Adding Doubling 102

4.1.5 Macroscale validation techniques . . . 103
4.2 Methods . . . 104
4.2.1 Defining generic tissue optical properties . . . 104
4.2.2 Generating discrete particle domains . . . 106
4.2.3 Measuring, reflectance, transmittance and ballistic light . . . 109
4.3 Validation . . . 111
4.3.1 Creating titanium dioxide validation phantoms . . . 111
4.3.2 Inverse adding doubling . . . 114
4.3.3 Monte Carlo . . . 118
4.3.4 Memory effects . . . 120
4.4 Optimisation of discrete particle domains . . . 122
4.4.1 Optimising the sphere design . . . 123
4.4.2 Optimising the medium width . . . 126
4.5 Chapter summary . . . 131

5 Modelling light focusing via wavefront shaping 133
5.1 Background . . . 134
5.1.1 Modelling input modes . . . 135
5.1.2 Modelling the transmission matrix . . . 136
5.1.3 Modelling output modes . . . 136
5.2 Methods . . . 137
5.2.1 Applying the computational framework . . . 137
5.2.2 Angular spectrum modelling of input modes . . . 138
5.2.3 Optimising incident light . . . 139
5.2.4 Spatially modulating input modes . . . 140
5.3 Modelling light focussing . . . 141
5.3.1 Light propagation through a titanium dioxide domain . . . 141
5.3.2 Focusing through and inside a titanium dioxide domain . . . 144
5.3.3 Evaluating enhancement . . . 152
5.3.4 Future work . . . 157
5.4 Chapter summary . . . 158

6 Modelling light propagation and focusing in tissue 160

6.1 Designing a tissue-like medium 161

6.2 Propagating light through a tissue-like medium 162

6.2.1 Speckle analysis 164

6.3 Focusing inside a thin tissue-like layer 168

6.4 Focusing inside deep tissue 170

6.4.1 Constructing a deep tissue medium 170

6.4.2 Modelling input modes 171

6.4.3 Focusing inside deep tissue 173

6.5 Modelling photoacoustic wavefront shaping 177

6.5.1 Motivation 177

6.5.2 Background 177

6.5.3 Results 179

6.5.4 Discussion 181

6.6 Chapter summary 183

7 General conclusions 184

7.1 Summary of contributions 184

7.2 Future directions 186

7.3 Synopsis 188

Appendices 189

A Research outputs 189

B Colophon 190

Bibliography 192

List of Figures

2.1 Schematic overview of light-tissue interaction mechanisms. 22
2.2 Trade-off between penetration depth and resolution for various optical imaging modalities. 27
2.3 Illustration of light shaping in biological tissue. 29
2.4 Diagram of wavefront shaping being used to generate a focus through a scattering medium. 31
2.5 Radar plot for evaluating the tissue-likeness of computational models. 44

3.1 Scaling behaviour demonstrated using Big $\mathcal{O}$ notation. 69
3.2 Example realisations of 3D discrete particle domains. 74
3.3 MSTM is used to simulate the propagation of light through various discrete particle volumes. 78
3.4 Histogram plot of a speckle pattern generated using 500 spheres. . . 79
3.5 MSTM is used to simulate the propagation of light through a 100 μm^3 discrete particle volume. 80
3.6 MSTM is used to simulate the propagation of light through a 100 μm^3 discrete particle volume. 82
3.7 Free space plane wave and Gaussian beam propagation simulated using MSTM. 83
3.8 Correcting the concentric ring artefact in MSTM by applying a scaling fix. 84
3.9 Validation of T-matrix simulation against analytic Mie theory. . . . 85
3.10 Comparing fields calculated using MSTM and FDTD. 88
3.11 Comparing fields calculated using CELES and FDTD. 89

4.1 Optical properties of biological tissue constituents. 94
4.2 Contributions of Mie and Rayleigh scattering to the reduced scattering coefficient in biological tissue. 96
4.3 Using Mie theory to determine the scattering coefficient and anisotropy of a titanium dioxide domain. 108
4.4 How the reflectance, transmittance, and unscattered transmittance are measured *in silico*. 110
4.5 Designing geometrically optimised simulation media for IAD validation. 112
4.6 Titanium dioxide discrete particle domain. 114
4.7 The transmittance, reflectance and ballistic profile for a Gaussian beam incident on a scattering medium calculated using the T-matrix method. 115
4.8 Validating the medium design process by simulating material characterisation experiments. 117
4.9 Simulation of Gaussian beam propagation through a diffusive layer. 119
4.10 Angular memory effect simulations through a tissue-like medium. . 121
4.11 Candidate discrete particle domains with tissue-like optical properties. 126
4.12 Monte Carlo simulation of a pencil beam propagating through a *"tissue-like"* volume. 128
4.13 Graphs from which the photons retained metric can be derived. . . . 129

5.1 Diagram of the proposed simulation framework. 138
5.2 Diagram showing focusing through a highly scattering layer. 140
5.3 Electric field magnitudes resulting from plane wave propagation through a titanium dioxide domain. 142
5.4 Simulation of light transmission and focusing through and inside a turbid layer. 145
5.5 Modelling focus generation with a variety of spatial modulations. . . 148
5.6 Simulating the focusing of light into target regions of different radii. 150

5.7 3D visualisation of the focus generated through a titanium dioxide slab. 151
5.8 Plotting enhancement vs the number of elements (N) used to generate a focus through a titanium dioxide layer. 152
5.9 Plot of five simultaneous foci and their enhancement vs the number of input modes. 153
5.10 Measuring the contributions of individual input modes to each focus in a simulation of WFS generating two foci. 155

6.1 Simulation of light transmission through a 800 μm deep tissue-like medium. 163
6.2 Speckle analysis at selected depths inside the simulated tissue-like domain. 166
6.3 Evolution of speckle size and speckle contrast with propagation depth inside the simulated tissue. 167
6.4 Simulation of focusing 100 μm inside a tissue-like layer. 169
6.5 Schematic illustration of the two methods used to model input modes. 172
6.6 Diagram showing focusing through into a tissue-like medium using random matrix modelling of input modes. 173
6.7 Simulation of the generation of an optical focus inside a tissue-like medium. 175
6.8 Side-view profile of optimised optical focus in a tissue-like medium. 176
6.9 Transverse intensity profiles of optical foci for varying target region sizes. 179
6.10 Investigating the enhancement of an acoustically confined focus inside tissue. 180

List of Tables

3.1 Definitions of terms in the T-matrix system and whether they are known or unknown 67
3.2 Comparing three different T-matrix codes. 71

4.1 Volume fraction adjusted absorption coefficients for various biological tissue constituents. 105
4.2 IAD derived optical properties for the geometrically optimised validation. 116

5.1 Maximum enhancement achievable using various spatial modulation methods. 137

Acronyms

2PFM Two-photon fluorescence microscopy

AME Angular memory effect

BEM Boundary element method

BiCGSTAB Biconjugate gradient stabilised

CCD Charge-coupled device

CPU CUDA-accelerated electromagnetic scattering for large ensembles of spheres

CPU Central processing unit

DMD Digital micromirror device

DOPC Digital optical phase conjugation

DOT Diffuse optical tomography

FastMM Fast superposition T-matrix method

FDTD Finite-difference time-domain

FEM Finite element method

FFT Fast Fourier transform

FMM Fast multipole method

FWHM Full width at half maximum

GB Gaussian beam

GLMT Generalised Lorenz-Mie theory

GMM Generalized multi-particle mie

GMRES Generalized minimal residual

GPU Graphics processing unit

IAD Inverse adding doubling

IR Infrared

LSFM Light sheet fluorescence microscopy

MC Monte Carlo

MPI Message passing interface

MSE Mean squared error

MSTM Multiple sphere T-Matrix

NA Numerical aperture

NIR Near-infrared

OCM Optical coherence microscopy

OCT Optical coherence tomography

OpenMP Open multi-processing

PA Photoacoustic

PAI Photoacoustic imaging

PALM Photoactivated localisation microscopy

PAT Photoacoustic tomography

PSF Point spread function

PSTD Pseudospectral time-domain

RAM Random-access memory

RMSE Root mean square error

ROI Region of interest

SIM Structured illumination microscopy

SLM Spatial light modulator

SNR Signal-to-noise ratio

SOFI Super-resolution optical fluctuation imaging

STED Stimulated emission depletion

T-matrix Transfer matrix

TM Transmission matrix

TMFP Transport mean free path

WFS Wavefront shaping

Chapter 1

Introduction

1.1 Motivation

The propagation of visible or near-infrared (NIR) light through biological tissue is fundamental to many diagnostic and therapeutic modalities, including microscopy [1], NIR spectroscopy [2], optical coherence tomography (OCT) [3], photoacoutic (PA) imaging (PAI) [4], photodynamic therapy [5], and optogenetic modulation [6]. However, biological tissue strongly scatters this propagating light, resulting in a significant reduction in intensity and a loss of coherence over depth. As a result, various imaging methods are limited to imaging superficial tissues only a few millimetres deep.

The nature of light propagation may give the impression that scattering is a stochastic and ultimately uncontrollable process. However, the microscale refractive index inhomogeneities that scatter incident light, and the subsequent interference interactions of this scattered light, are fundamentally deterministic processes. This deterministic nature of scattering gives rise to many interesting (and exploitable) optical phenomena.

Wavefront shaping (WFS) [7] spatially modulates light incident onto a scattering medium to cause scattered light to interfere constructively to produce an optical focus at depth. Under ideal circumstances, it has been demonstrated that this optical

focus can be generated at depths as significant as 9.6cm [8]. Other achievements of WFS include the use of shaped light to generate PA images of a bee wing that overcome the acoustic diffraction limit [9], endoscopic imaging through a multi-mode fibre [10], imaging around corners and through scattering media by exploiting speckle correlations [11], improved free space optical signal transmission [12], and and improved cryptographic algorithm design [13]

Other optical phenomena that have the potential to enhance biomedical imaging include tilt and angular memory effects [14], transmission matrix engineering [15], the existence of open scattering channels [16], and scattering invariant modes of light [17].

Experimental investigation of such coherent phenomena, including WFS, is often constrained by what can be summarised as a lack of control. In contrast to computational techniques, experimental methods cannot easily resolve both amplitude and phase information, cannot easily evaluate the field inside a given medium, and cannot comprehensively and dynamically control the medium with respect to optical properties or geometry. Consequently, the ability to reliably simulate coherent light propagation through biological tissue has the potential to shed light on some unanswered questions regarding WFS. For example, how does shaped light propagate through a medium? Is this propagation different through various biological tissues? What are the limits of focused light concerning both depth and the degree of control over the incident field? What are the most effective methods to generate an optical focus? How does the signal-to-noise ratio (SNR) affect this focus?

However, current computational approaches to simulate light propagation through biological tissue are either too computationally intensive to model volumes of at least the transport mean free path (TMFP) or too incomplete to model the underlying deterministic scattering and interference processes accurately.

1.2 Problem statement

At present, there are no computational methods able to rigorously simulate visible and near-infrared light propagation through biological tissue at large enough scales. This stymies investigation of WFS and other coherent phenomena.

1.3 Aims

The broad aim of this PhD is to develop a rigorous and efficient framework for simulating coherent light propagation through bespoke scattering media, including *tissue-like* media. This framework must be able to rigorously simulate coherent light propagation through millimetre-scale tissues. Both the underlying *in silico* representation of biological tissue and the computational method of light propagation must be exhaustively validated.

Following validation, this method is used to simulate coherent phenomena that have the potential to facilitate deep tissue imaging. Specifically, this thesis is focused on modelling WFS due to its applicability across a range of imaging modalities [18]. Consequently, one major aim is to simulate the generation of an optical focus inside and through bespoke scattering media.

To demonstrate the applications of the proposed simulation framework, new aims are defined. These include replicating the seminal Vellekoop and Mosk demonstration of WFS by focusing light through a titanium dioxide domain [7] and investigating the formation of a focus inside tissue using a PA feedback mechanism.

1.4 Objectives

The objectives of this thesis are to:

- Evaluate existing methods for simulating coherent light propagation. Implement a full-wave approach that is computationally efficient enough with regard to time and memory to simulate domains of at least a TMFP.
- Design an appropriate *"tissue-like"* scattering medium. The method of mod-

elling turbid media must be designed to have bespoke optical properties, such that various media can be represented *in silico*.

- Validate the model to ensure that the method simulates the scattering of light physically realistically and that the macroscale characterisation of this scattering matches theory.

- Model light focusing via WFS by generating an optical focus through and inside a scattering titanium dioxide phantom. Ensure physical accuracy by investigating WFS phenomena like multiple foci and enhancement.

- Model light propagation and focusing inside a tissue-like domain. Demonstrate the applications of the model by investigating the design requirements of a photoacoustic wavefront shaping (PAWS) system.

1.5 Report structure

The main body of this thesis begins with a background description of the physics of light propagation through biological tissue in the micro and macroscales, concluding with a discussion on the inimical effects of scattering. The theory of WFS is then explored - how spatially modulated light can be designed to constructively interfere to produce desired optical fields and overcome scattering. The first chapter ends with a discussion on the existing computational attempts to model WFS. This includes a review of select methods of modelling light propagation and the scattering medium. Critically, the requirements of the computational framework are defined, and an appropriate modelling framework is identified.

The next chapter describes the first component of this framework - specifically, how the T-matrix method is used to simulate light propagation through discrete particle media. This includes a review of the T-matrix method and existing T-matrix codes. The process of implementing and modifying these T-matrix codes on available hardware is described, and the codes are validated using Mie theory and the Finite-Difference Time-Domain (FDTD) method.

The following chapter is concerned with the second component of the computational framework - namely, how the discrete particle method is used to construct models of bespoke scattering media. The relevant background theory of the method is first discussed. A method of constructing discrete particle media is created and validated using Inverse Adding Doubling (IAD), Monte Carlo, and memory effects. The discrete particle media is then optimised to maximise efficiency when coupled with the T-matrix method - both with respect to the design of the constituent spheres and the bounding medium.

The next chapter focuses on the final aspect of the computational framework - the modelling of WFS. The theory of WFS is reviewed, and a method of modelling WFS is constructed, using an angular spectrum decomposition of the incident light field or random instances of the scattering medium. The method is used to model the generation of an optical focus through a titanium dioxide layer, replicating the seminal Vellekoop and Mosk paper on WFS. The scaling of the enhancement of said focus as a function of the number of input modes is quantified and validated against theory. Then a focus is generated inside the medium, something that was not achievable using Vellekoop and Mosk's original experimental approach.

Moving on from titanium dioxide phantoms, light is propagated and focused through and inside a *"tissue-like"* medium. The method is then used to investigate PAWS. This begins by describing the theory and motivation behind using PA feedback to shape light. To determine the requirements of a theoretical PAWS system, the enhancement of an acoustically constrained focus is modelled as a function of focus size, and various enhancement thresholds are plotted as a function of the number of input modes and focus size.

The thesis concludes with a summary of the contribution made to the field and a discussion of potential future applications of the proposed model.

Chapter 2

Background

2.1 Light propagation through biological tissue

Light propagating through biological tissue is subject to both scattering and absorption [19]. These processes limit the performance of optical imaging techniques by reducing resolution and restricting penetration depth [20]. A clear understanding of scattering and absorption (and their relative contributions to overall attenuation) is essential for developing realistic computational models of light transport. Figure 2.1 provides an overview of light–tissue interaction mechanisms.

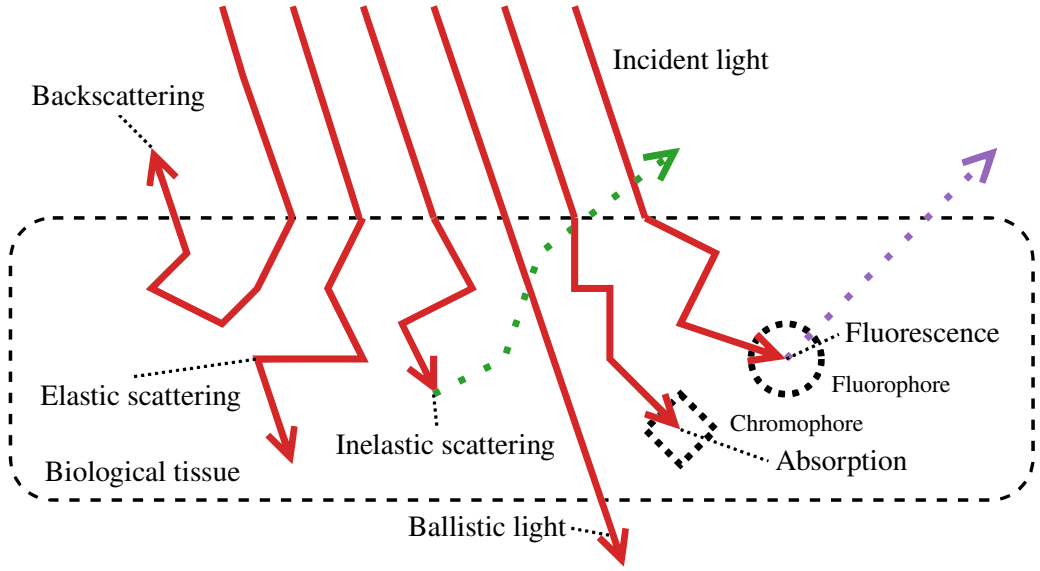

Figure 2.1: Schematic overview of light-tissue interaction mechanisms. Incident light propagating through biological tissue undergoes elastic and inelastic scattering, absorption by chromophores, and fluorescence emission.

Light-tissue interactions can be broadly categorised into two macroscale mechanisms: scattering and absorption [19]. Each mechanism contributes differently to the perturbation and attenuation of the propagating light, and must be modelled appropriately in any computational method. Below, each process is defined.

2.1.1 Scattering theory

Scattering arises due to microscopic refractive index inhomogeneities within biological tissue - such as cell membranes, organelles, and collagen fibrils [21]. These scattering events can be broadly classified into elastic and inelastic processes, depending on whether the energy (and hence frequency) of the scattered photon is conserved.

In elastic scattering, photons interact with the medium without any change in energy. The direction of propagation is altered, but the wavelength remains unchanged. The physical mechanism behind elastic scattering is the re-radiation of light by small particles in response to an incident electromagnetic wave [22]. These inhomogeneities act as dielectric scatterers, meaning they can be polarised, which is when the incident electric field excites bound electrons, temporarily inducing a separation of positive and negative charge (a dipole moment). This oscillating charge distribution emits scattered light at the same frequency as the incident light. The scattered light's directionality and intensity depend on the particle's size, geometry, refractive index, and spatial arrangement within the medium.

Particle size is particularly noteworthy, as elastic scattering can be further classified based on the size parameter, x, which is a dimensionless quantity that compares the physical size of a scattering particle to the wavelength of the incident light:

$$x = \frac{2\pi r}{\lambda}$$

where r is the radius of the scatterer and λ is the wavelength of light. The size parameter defines the nature of the elastic scattering:

- *Rayleigh scattering:* $x \ll 1$ Scattering by particles much smaller than the wavelength.

- *Mie scattering:* $x \sim 1$ Scattering by particles comparable to the wavelength.

- Geometric scattering: $x \gg 1$. Scattering by particles much greater than the wavelength.

These classifications are important as they determine the nature of the scattering that occurs and set limits on the modelling approach.

In contrast to elastic scattering, inelastic scattering involves an exchange of energy between the incident photon and the medium, resulting in a change in the photon's wavelength. Unlike elastic processes, where the scattered photon retains the same energy and frequency as the incident light, inelastic scattering produces photons with either lower (Stokes shift) or higher (anti-Stokes shift) energy, depending on the energy transfer direction.

Both elastic and inelastic scattering can be understood in terms of the paths photons take as they propagate through tissue. In the most straightforward case, photons travel without any scattering events - these are known as ballistic photons. They retain their original direction and coherence.

Photons that undergo a small number of low-angle scattering events are referred to as snake photons. While they deviate slightly from their original path, they still preserve a degree of directional information.

In contrast, photons that undergo multiple scattering events with large angular deviations are known as diffuse photons. These photons follow complex, randomised paths, losing both spatial and temporal coherence.

The proportion of each photon type is a function of depth: ballistic photons dom-

inate at shallow depths but are rapidly attenuated, snake photons extend imaging capability slightly deeper, and diffusely scattered photons become dominant in bulk tissue. This transition fundamentally limits the penetration depth and resolution of optical imaging techniques.

A multitude of the individual scattering events described above combine to form the aggregate scattering behaviour of the medium, which can be characterised using a set of macroscopic optical parameters.

The scattering coefficient, μ_s, quantifies the probability of a scattering event per unit distance travelled by a photon and is typically measured in mm^{-1}. It reflects the density and cross-sectional area of scattering centres within the medium.

The scattering phase function, $p(\theta, \psi)$, describes the angular probability distribution of a single scattering event, where θ is the polar angle and ψ is the azimuthal angle. To simplify this angular dependence, the anisotropy factor, $g = \langle \cos(\theta) \rangle$, is defined, which represents the average cosine of the scattering angle. This value ranges from 0 (isotropic scattering) to 1 (pure forward scattering).

A commonly used derived quantity is the reduced scattering coefficient, $\mu_s' = \mu_s(1-g)$, which accounts for both the frequency and angular deviation of scattering events. It quantifies the rate at which photons lose their directionality.

These parameters also define characteristic length scales. For example, the transport mean free path, $l^* = 1/\mu_s'$, represents the average distance over which the direction of photon propagation becomes fully randomised. This scale marks the transition from quasi-ballistic to diffusive light transport.

2.1.2 Absorption theory

Absorption is the process by which the energy of an incident photon is transferred to the medium, typically resulting in heat generation or photochemical effects. Unlike

scattering, which redirects photons, absorption removes them from the propagating light field.

In biological tissue, absorption occurs when photons interact with specific chromophores - molecules or structures that have wavelength-dependent absorption properties. Common chromophores include haemoglobin, water, melanin, and lipids, each with distinct absorption spectra.

Once absorbed, the photon's energy is dissipated through various pathways. Most commonly, it is converted into heat. Alternatively, absorbed light can cause rapid thermal expansion and generate an acoustic wave, as exploited in photoacoustic imaging [4].

Sometimes, absorbed photons can lead to fluorescence, where a molecule re-emits part of the absorbed energy as light. In this case, the molecule is excited to a higher electronic state and then relaxes to a lower state by emitting a photon at a longer wavelength. Unlike scattering, this is a two-step absorption–emission process, typically with a characteristic delay and loss of coherence.

The extent of absorption is characterised by the absorption coefficient, μ_a, which describes the probability of photon absorption per unit length of propagation. Absorption contributes directly to attenuation of the optical field and defines key imaging parameters such as contrast and signal decay with depth.

2.1.3 Inimical effects of scattering

The scattering of light within biological tissue imposes fundamental constraints on both the penetration depth and spatial resolution of optical imaging techniques. As light propagates, its interaction with microscopic refractive index inhomogeneities causes repeated scattering events that rapidly degrade spatial coherence. This presents a trade-off: modalities that achieve high spatial resolution are restricted to shallow depths, while those capable of imaging deeper into tissue have a lower

resolution. This compromise is illustrated in Figure 2.2, which plots the resolution and penetration depth of various biomedical imaging methods.

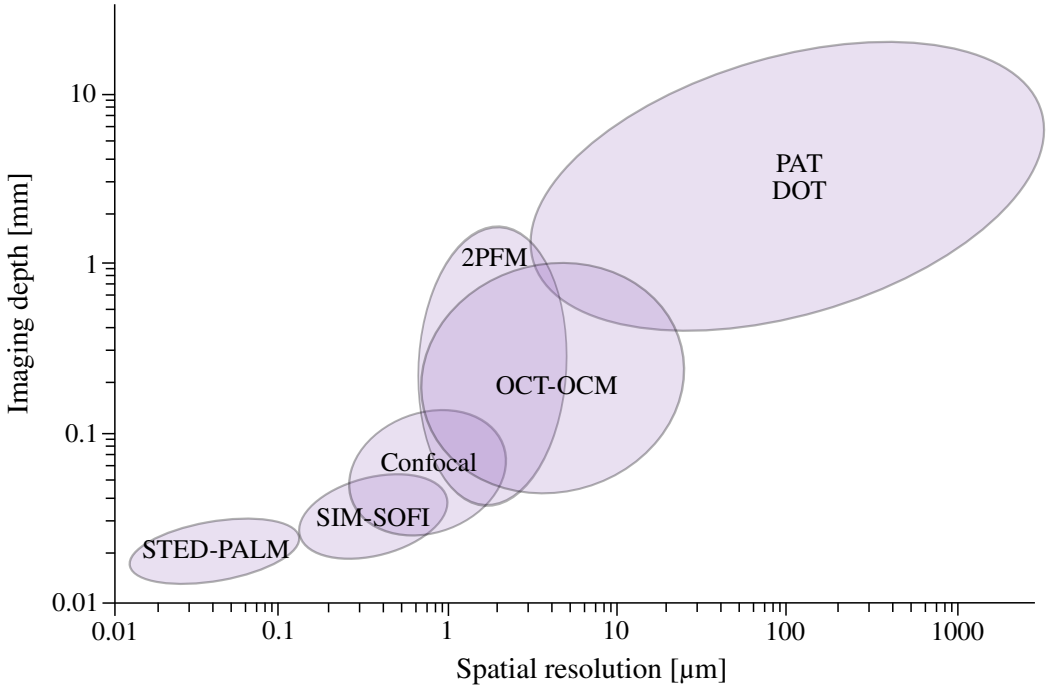

Figure 2.2: Trade-off between penetration depth and resolution for various optical imaging modalities. Modalities with higher spatial resolution typically suffer from limited imaging depths due to scattering, while those capable of deeper imaging often compromise on resolution. Imaging modalities featured are stimulated emission depletion (STED) [23], photoactivated localisation microscopy (PALM) [24], structured illumination microscopy (SIM) [25], super-resolution optical fluctuation imaging (SOFI) [26], confocal microscopy [27], two-photon fluorescence microscopy (2PFM) [28], optical coherence tomography OCT [3], optical coherence microscopy (OCM) [29]; diffuse optical tomography (DOT) [30], photoacoustic tomography (PAT) [4]. Adapted from Gigan [31].

Techniques that operate within the quasi-ballistic regime, typically less than a few transport mean free paths (1–2 mm in most soft tissues), include confocal microscopy [27], 2PFM [28], OCT [3] and the various super-resolution microscopy techniques (some of which can be found in Figure 2.2). These modalities rely on the detection of ballistic or snake photons that have experienced minimal scattering and thus retain directional and phase information necessary for high-resolution image formation. However, because unscattered photons are rapidly attenuated, the depth range of such methods is limited.

Beyond this superficial layer, photons undergo multiple scattering events, and the light field becomes increasingly diffuse. To image at greater depths, other modalities such as DOT [30] and PAT [4] make direct or indirect measurements of the intensity of the scattered light. For example, DOT directly measures highly scattered diffuse light and compares measurements to a photon transport model based on the diffusion equation to create tomographic maps of the tissue's optical properties [30]. On the other hand, PA techniques measure a pressure wave that is generated when absorbed light causes rapid thermal expansion in tissue [4]. These methods extend the penetration depth to centimetre scales; however, the loss of spatial coherence means these systems cannot directly resolve fine structures.

Scattering also imposes significant constraints on therapeutic modalities that rely on the targeted delivery of light. In photodynamic therapy, for instance, light must activate photosensitising agents within tumours, but scattering severely limits the fluence at depth, reducing efficacy [5, 32]. Similarly, in optogenetics, where precise light delivery is needed to stimulate neurons, scattering limits selectivity and necessitates invasive light delivery (e.g. endoscopes) [6, 18, 33].

To overcome these penetration and resolution limitations, researchers have explored methods to reverse or exploit scattering. One such approach is WFS, which modulates the spatial phase and/or amplitude of the incident light such that the scattered light constructively interferes to form a focus within or beyond a turbid medium.

2.2 Wavefront shaping

2.2.1 Fundamentals of wavefront shaping

Light propagating through biological tissue is scattered, resulting in a loss of coherence and a decrease in intensity as a function of depth [20]. As established in Chapter 2.1, the aggregate scattering behaviour of propagating light is the result

of a multitude of individual scattering events, each caused by naturally occurring refractive index inhomogeneities within tissue. These scattering events and the resulting interference are deterministic, and can be controlled to shape light inside the tissue for beneficial purposes, as shown in Figure 2.3. This process of shaping light is known as wavefront shaping (WFS). With WFS, it is possible to compensate for the inimical effects of scattering discussed in Section 2.1.3.

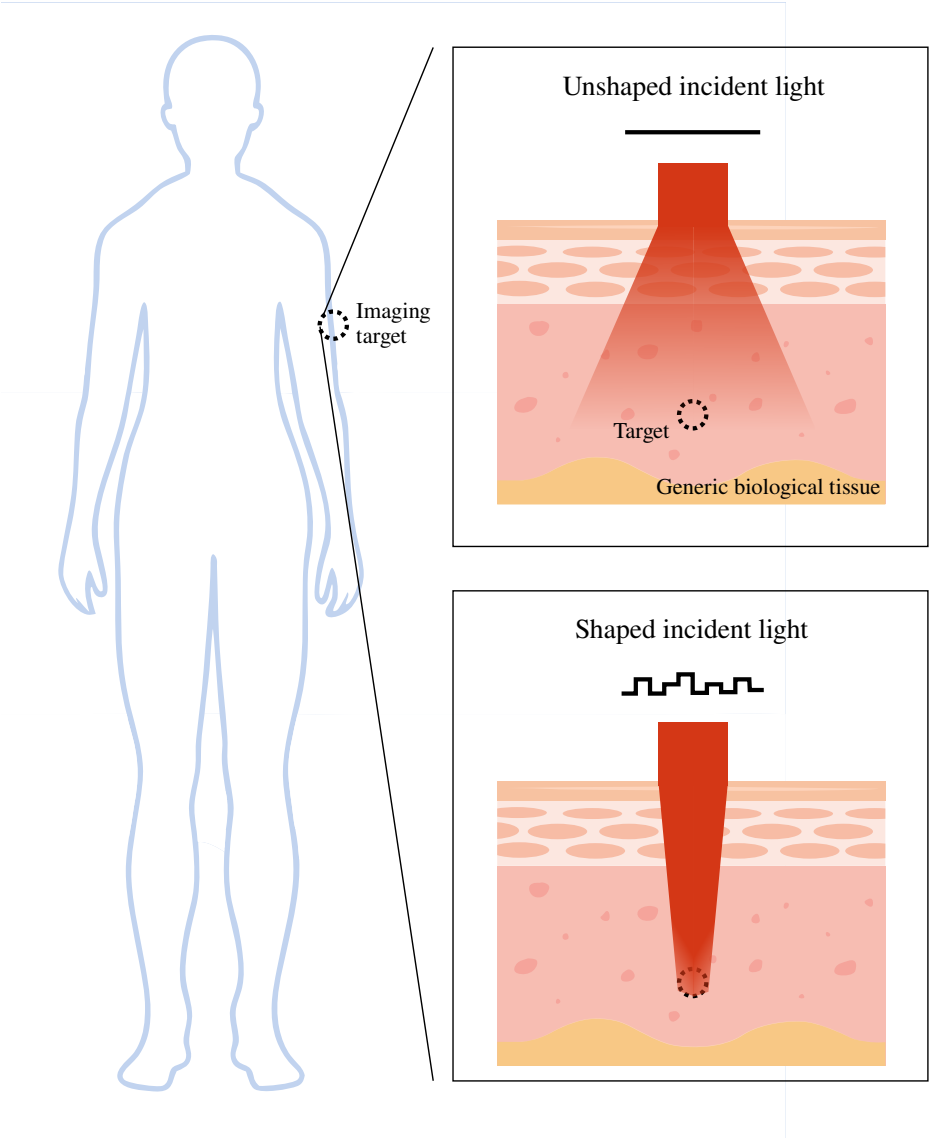

Figure 2.3: Illustration of light shaping in biological tissue. Consider a therapeutic or imaging target located over a transport mean free path deep. Unshaped incident light is scattered by refractive index inhomogeneities in the tissue, resulting in loss of coherence and low intensity across the target region. In contrast, shaped incident light is engineered to compensate for scattering, allowing constructive interference at the target region, generating an optical focus.

To control the propagation of light through biological tissue, WFS modulates the phase and/or amplitude of the incident light. As shown in Figure 2.3, this process involves shaping the wavefront such that the scattered light constructively interferes at a target location. In practice, this is achieved using programmable devices such as spatial light modulators (SLMs) or digital micromirror devices (DMDs), which impose specific phase delays (or amplitude variations) across the incident light's spatial profile.

There are several approaches to determining the appropriate wavefront modulation. These can be broadly categorised into four main strategies: iterative, digital optical phase conjugation (DOPC), transmission matrix (TM), and model-based methods.

2.2.1.1 Iterative methods

Iterative methods shape a wavefront gradually using feedback mechanisms. For example, to generate an optical focus, a feedback-based system might iterate through each element on an SLM, shifting the phase between 0 and 2π while measuring the resultant intensity at a target region [7]. Such a setup is shown in Figure 2.4. Other, more sophisticated, techniques and algorithms for iteratively optimising the incident field exist, and will be covered in Section 2.2.3.

The first demonstration of WFS was achieved in 2007 by Vellekoop and Mosk [7]. They directly measured intensity across a plane of scattered light behind a turbid titanium dioxide phantom. They showed that by iteratively adjusting an SLM, it was possible to focus scattered light into a defined target region [7]. This feedback-based wavefront optimisation produced a focal spot over 1000 times brighter than the diffuse background [7].

Direct intensity measurements are straightforward when shaping through a turbid medium with accessible output planes: the focal plane can be projected directly

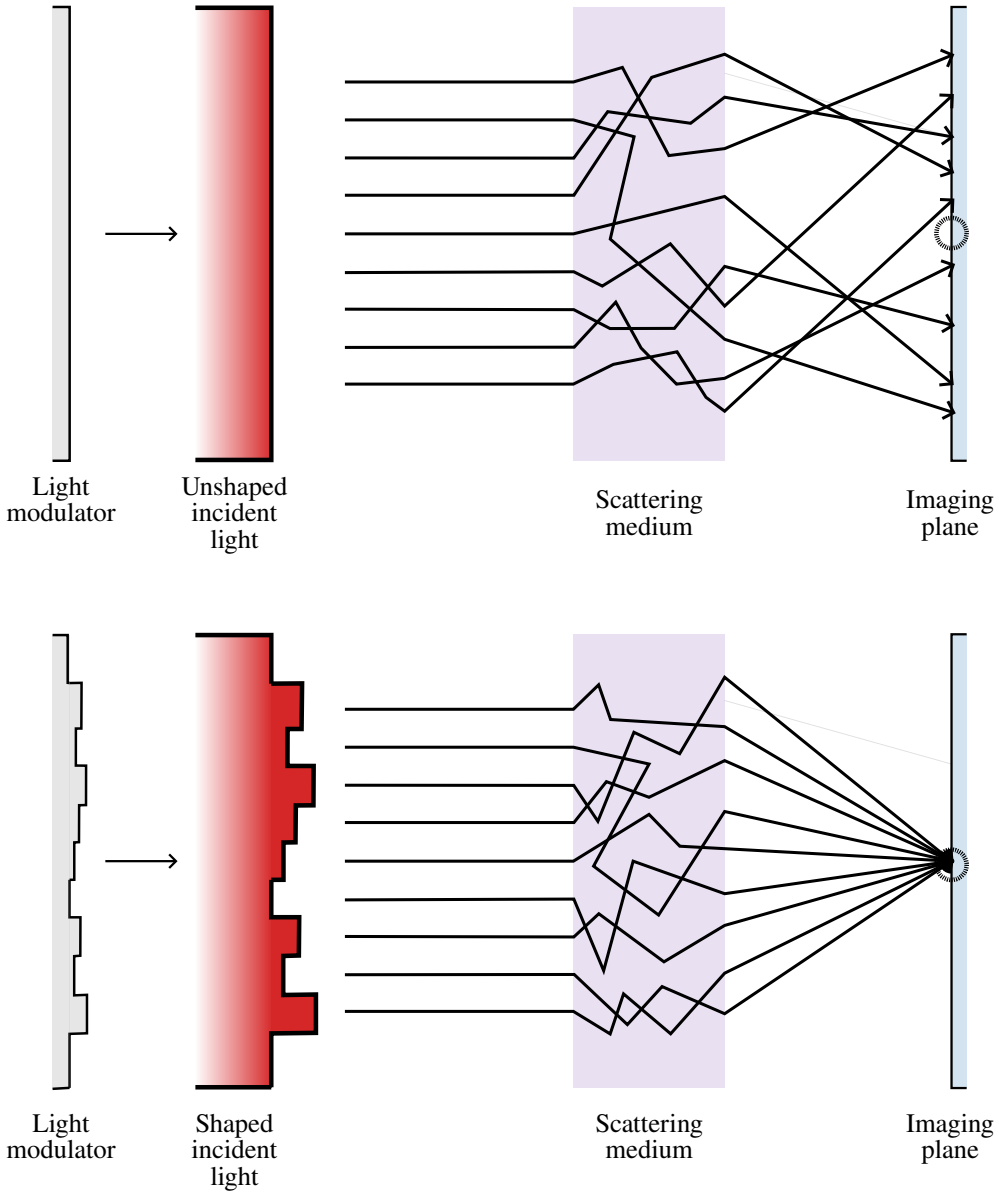

Figure 2.4: Illustration of iterative WFS to generate an optical focus through a scattering medium. A light modulator (e.g. an SLM or DMD) is used to shape the incident light field. The particular spatial modulation (e.g. the phase and/or amplitude mask) is optimised using iterative feedback from the imaging plane and an associated algorithm. The optimised light field can generate an optical focus behind the medium at a desired target.

onto a charge-coupled device (CCD) [34]. However, when generating a focus inside a scattering medium, direct measurement becomes impossible. Instead, guidestar-based methods must be employed to estimate the focus indirectly [35].

Guidestars provide an indirect measurement of the field inside a scattering medium. For example, consider a nanoscale fluorescent bead embedded within a turbid medium. The bead is illuminated by a light field that can be spatially modulated. Initially, only scattered light reaches the bead, producing a weak but detectable fluorescent signal. Modulating the wavefront of the incident light and measuring the resultant change in intensity of the fluorescent signal provides an indirect measure of how effectively incident light is being focused onto the bead [36].

Guidestars do not have to be physical beads - non-invasive alternatives include measuring the strength of the ultrasond signal generated via the photoacoustic effect [37], or detecting a two-photon fluorescence signal [38].

2.2.1.2 Digital optical phase conjugation (DOPC)

The second major approach is digital optical phase conjugation (DOPC), which exploits the time-reversibility of scattering. Since scattering in biological tissue is deterministic, the phase conjugate of a scattered wave retraces its original path, refocusing at its source [39].

To perform DOPC, the scattered light originating from a guidestar (e.g., a fluorescent source inside the medium) is recorded using interferometry. The phase-conjugated version of this wavefront is then reconstructed using an SLM to reintroduce the light field in reverse, effectively refocusing the beam.

Like iterative methods, DOPC requires guidestars to generate measurable scattered fields. These can largely be physical or virtual in nature. Examples of physical guidestarts include fluorescent beads [40], nonlinear nanoparticles [41], or magnetic particles [42]. Examples of virtual guidestarts include ultrasound-tagged photons [43], photoacoustic emissions [37], or two-photon fluorescent signals [38].

2.2.1.3 Transmission matrix approaches

The third method to optimising incident light fields is called the transmission matrix (TM) approach, and was introduced by Popoff *et al.* in 2010 [44]. The TM method creates a linear mapping between the input incident light field and the output (see Section 2.2.2 for TM theory). Determining the TM makes it possible to deterministically calculate the correct spatial modulation of the incident light to generate a desired output field. For example, it can be used to transmit entire images through scattering layers [45].

Calculation of this TM is fairly slow, but once determined, it means further linear mappings between desired output fields and optimised input fields require no laborious iterative optimisation. Note that the scattering medium must be static - dynamic movement causes the transmission matrix to change.

2.2.1.4 Model-based method

Recent advances in computational optics have led to the emergence of new methods for optimising incident wavefronts. These techniques can be termed model-based methods, as they rely on an *a priori* understanding of the physics of light propagation through the scattering medium.

Conventional iterative approaches and DOPC rely on direct feedback or guidestar measurements to focus light into a given target - ultimately, some signal must be directly or indirectly measured. Measuring this signal can be challenging, requiring careful calibration of the detector, constraints on the location and stability of the guidestar, and often invasive access to the target region. *In vivo*, these requirements can be difficult to satisfy. Model-based methods have the potential to circumvent some of these limitations by constructing a *in silico* duplicate of the scattering system. This model can then be used to computationally compute the input wavefront that will produce a desired focus or image, rather than searching for it iteratively using feedback.

Early model-based approaches employed data-driven machine learning, treating the medium as a black box. Neural networks were trained to infer the correct wavefront modulation from measured speckle patterns or target locations. For instance, Li *et al.* and Turpin *et al.* used speckle patterns as training data to construct convolutional neural networks able to reconstruct images through a scattering medium [46, 47]. While effective under stable conditions, these early methods typically required large training datasets tailored to each specific medium and, as such, were not particularly generalisable.

To improve generalisability, recent methods have aimed to model the propagation of light more rigorously. For example, D'Arco *et al.* built a *"physics-based"* neural network whose layers and connectivity are designed to mimic scattering within an optical system [48]. Meanwhile, Thendiyammal *et al.* do not use deep learning - instead using a beam propagation method to simulate light propagation. They demonstrate a 2x improvement in the two-photon fluorescence signal detected at depth compared to non-model-based WFS methods [48].

2.2.2 Transmission matrix theory

WFS is ultimately a linear optical phenomenon, and consequently can be constructed using a simple matrix formalisation [34], relating the incident field (E_{in}) to the transmitted scattered field (E_{out}) through the transmission matrix, $\mathbf{T}$:

$$E_{\text{out}} = \mathbf{T} \cdot E_{\text{in}} \tag{2.1}$$

An arbitrarily complex input field can be decomposed into a series of input modes, which are orthogonal spatial components of the incident wavefront (e.g., elements on a spatial light modulator). Conversely, output modes can be defined to spatially discretise the transmitted scattered light (e.g., pixels captured on an imaging system). Therefore, the transmission matrix can be considered a characterisation of the scattering behaviour of a given system, describing the linear transformation from input modes to output modes - each element of the transmission matrix represents

the complex amplitude coupling between an input mode and an output mode.

2.2.3 Optimisation of input modes

As previously mentioned, iterative WFS methods rely on feedback-based algorithms to optimise the incident wavefront [49]. Several optimisation algorithms have been developed for this purpose.

The stepwise sequential algorithm modulates each element independently and stores the modulation that results in the largest increase in intensity. This process is guaranteed to find the optimal phase or amplitude map, though it is computationally slow and sensitive to noise [50, 51].

Partition-based methods improve convergence speed by randomly selecting and simultaneously modulating subsets of elements. This parallel modulation results in faster initial intensity growth but typically plateaus as iterations increase [49, 51].

Genetic algorithms take a stochastic approach, generating and evaluating random phase and/or amplitude maps. The best-performing maps are linearly combined and mutated (meaning some elements are randomly altered). The process is repeated iteratively. Genetic algorithms tend to converge quickly and are highly resistant to noise, though they do not guarantee a global optimum [52, 51].

2.2.4 Applications of wavefront shaping

WFS allows for deeper coherent light penetration into tissue, and as such has the potential to directly benefit many biomedical imaging and treatment modalities. The following section summarises notable applications of WFS.

2.2.4.1 Photoacoustic Imaging

Photoacoustic imaging (PAI) relies on pulsed laser light to generate ultrasonic waves via the photoacoustic effect. These waves are detected by surface transducers and used to form an image [53]. PAI relies on endogenous chromophores to generate the photoacoustic signal, and as such has high contrast and specificity.

The two primary forms of PAI include photoacoustic tomography (PAT) and photoacoustic microscopy (PAM) [54, 4]. PAT uses wide field illumination and array detection for deep tissue imaging, and PAM uses focused light for high-resolution imaging of superficial structures.

WFS can extend the imaging depth by generating optical foci within scattering tissue, thereby improving the resolution and signal-to-noise ratio (SNR) of PA images [9]. Lai *et al.* utilised the Grueneisen memory effect to surpass the acoustic diffraction limit [55], while Conkey *et al.* demonstrated high-resolution imaging of biological structures using sub-diffraction limited focusing [9]. Chaigne *et al.* approached focus generation by measuring the PA transmission matrix, enabling multi-output optimisation without iterative feedback [56, 57].

2.2.4.2 Optical Coherence Tomography

Optical coherence tomography (OCT) provides high-resolution (< 10 μm) images by detecting singly backscattered light via low-coherence interferometry [3, 58]. However, multiple scattering events reduce penetration and contrast [59].

By shaping the incident light, WFS can refocus multiply scattered light to constructively interfere at depth, enhancing both the SNR and imaging depth [60]. Yu *et al.* demonstrated this in both fibrin phantoms and biological tissues [61]. Kim *et al.* later performed a computational simulation of WFS-enhanced OCT using the FDTD method, demonstrating increased resolution and penetration depth [62].

2.2.4.3 Light Sheet Fluorescence Microscopy

Light sheet fluorescence microscopy (LSFM) illuminates samples with a thin planar sheet of light perpendicular to the detection axis [63]. This orthogonal illumination improves contrast by reducing background excitation [64].

WFS can be used to correct aberrations and refocus scattered light into a uniform sheet, thus maintaining sectioning quality. Dalgarno *et al.* demonstrated this with an SLM, dynamically switching between Gaussian and Bessel beam illumi-

nation [65]. Similarly, Schneider *et al.* used an optimisation algorithm to create a robust light sheet through a turbid medium [66].

2.2.4.4 Endoscopic Imaging

Endoscopic imaging employs fibre bundles for minimally invasive access to internal tissue [67]. While single-mode fibres retain imaging capabilities, multimode fibres scramble the light, producing speckle patterns [18].

WFS can reverse this scrambling, allowing imaging through multimode fibres. Papadopoulos *et al.* initially achieved focusing using optical phase conjugation [68], later extending this to image transfer [69]. Optimisation-based methods have been proposed to overcome the limitations of phase conjugation in dynamic scenarios [70]. This technique has been coupled with photoacoustic imaging to enable endoscopic photoacoustic tomography [71].

2.2.4.5 Photodynamic Therapy

Photodynamic therapy (PDT) uses light to activate photosensitising agents that produce cytotoxic radicals for targeted cancer treatment [5, 32]. However, tissue scattering confines treatment to superficial depths.

WFS offers a solution by generating deep optical foci to activate these agents non-invasively. Efforts to improve SLM speed [72] and algorithm performance [52] aim to enable real-time focus generation in dynamic tissue environments [73].

2.2.4.6 Optogenetics

Optogenetics modulates neural activity using light-sensitive ion channels, allowing precise control of individual neurons [74, 75]. This helps researchers map neural connections *in vivo*.

WFS facilitates cell-specific stimulation by focusing light through scattering tissue. Yoon *et al.* demonstrated optogenetic control through the intact mouse skull, eliminating the need for invasive probes and minimising tissue damage [18].

2.2.4.7 Optical Tweezing

Optical tweezers trap and manipulate microscopic particles using a tightly focused laser beam [76].

WFS can tailor the phase profile of the trapping beam, increasing trap stiffness and improving manipulation. Taylor *et al.* enhanced optical traps using phase modulation and later improved the optimisation speed [77, 78].

2.2.4.8 Super-Resolution Lenses

Conventional optics are diffraction-limited in resolution, typically constrained to about half the wavelength of light used [79]. Super-resolution techniques aim to overcome this barrier and allow imaging of sub-wavelength structures.

WFS can create sub-diffraction-limited foci using shaped beams transmitted through scattering media, termed *"scattering super-lenses"* [80]. Vellekoop and Park both demonstrated such lenses using nanoparticle-based turbid layers [81, 80], offering an alternative to other super-resolution approaches.

2.2.4.9 Cryptography

Turbid media can function as physically unclonable cryptographic keys due to their inherent complexity [82].

WFS enhances this by further increasing complexity or decrypting such systems. Goorden *et al.* used two SLMs and a low-photon-count beam to create a quantum-secure key, immune to emulation attacks [83, 84]. Conversely, Liao *et al.* demonstrated that WFS could be used to iteratively decrypt optical keys without prior system characterisation [85].

2.2.4.10 Signal Transmission

Free-space optical (FSO) systems offer high-bandwidth wireless communication alternatives but suffer from line-of-sight and atmospheric constraints [86].

WFS can redirect optical beams via shaped reflections to overcome these limitations. Kaina and Najafi proposed using SLMs as adaptive reflectors for microwave and infrared beams, respectively [87, 88]. Cao *et al.* extended this by integrating the SLM into the transmitter itself, though the approach remains limited by optimisation speed [12].

2.2.5 Limitations and challenges of wavefront shaping

As Section 2.2.4 demonstrates, WFS is a promising technique with a wide range of applications. However, significant challenges remain that limit its application, particularly in biological tissues.

One major limitation arises from the dynamic nature of biological tissue. Small-scale motion and thermal fluctuation can cause decorrelation of the scattering medium, significantly reducing the time during which an optimised wavefront remains valid. Typically, this decorrelation time is on the order of 0.1–10 milliseconds [89]. As WFS methods often require thousands of measurements or iterations, this time constraint severely limits the depth and stability of optical focusing *in vivo*.

Technical constraints also limit the real-world performance of WFS systems. The number of independently controllable input modes is determined by the spatial resolution of the wavefront modulator. Meanwhile, the number of independently resolvable output modes is governed by the spatial resolution of the feedback mechanism, such as a CCD camera or PA detector. As enhancement scales with the ratio of input to output modes (N/M), the achievable focal intensity is often limited by system design (e.g. the necessity of a guidestar with a fixed resolution).

Experimental investigation of WFS is also limited by what can be measured. It is not possible to directly evaluate the amplitude and phase of the field inside a scattering medium. Instead, researchers must rely on indirect feedback mechanisms - guidestars such as fluorescent or PA signals. These mechanisms offer only partial information and cannot fully characterise how light propagates inside tissue. This

limitation makes it difficult to study fundamental questions about focus formation, or the spatial structure of speckle patterns.

There is a growing consensus that better modelling is needed. A recent roadmap on WFS explicitly highlights the development of fast and accurate light propagation simulations as a critical challenge in the field [90].

2.3 Computational modelling of wavefront shaping

2.3.1 Advantages of computational modelling

Experimental investigation of WFS and related coherent phenomena can be complemented by computational approaches. This is because computational models have the following advantages:

- **Access to internal fields:** Computational models can evaluate both amplitude and phase inside a scattering medium.
- **Complete control over optical properties:** The geometry, refractive index, and spatial distribution of scatterers can be precisely defined.
- **High reproducibility:** Simulations are deterministic and repeatable, allowing exploration of parameters without noise or variability.
- **Isolation of effects:** Individual factors (e.g. anisotropy, depth, speckle size, detector resolution) can be independently varied and studied in isolation.

As a consequence, applying computational methods to model coherent phenomena such as WFS could be used to:

Improve existing model-based wavefront shaping techniques: Thendiyammal et al. have demonstrated increased light penetration of model-based wavefront-shaped light, but their technique has only been applied to microscopy where scattering is weak [91]. This is due to the physically unrealistic beam propagation method they employ for modelling light propagation [91]. The research group intends to

implement a more physically rigorous model they have developed [92], as explained in a recent roadmap [90].

Directly observe light propagation inside scattering media: Experimental methods rely on indirect feedback (e.g., guidestars) and cannot measure the optical field inside the medium [35]. Computational models can directly evaluate amplitude and phase at arbitrary points within the medium, allowing for detailed analysis of speckle formation and focus evolution. One application of this is the study of open scattering channels - special input modes that lead to high transmission through turbid media [93, 16]. These channels are theoretically predicted to exist but are difficult to research experimentally, as they require full knowledge of the transmission matrix and internal fields.

Test the effect of changing tissue properties: The optical properties of biological tissue govern the aggregate statistical behaviour of light propagation. Computational methods allow precise control over these properties, as well as simulation geometry. One application of computational modelling would be for investigating the memory effect, which refers to the persistence of correlations in the scattered light when the input wavefront is tilted or translated [94, 95]. Angular memory correlations have been used to image through scattering layers [96], but the range over which these correlations persist is very narrow. It has been theorised that the angular memory range is expected to be higher in biological tissue, which is highly anisotropic [97]. Moreover, it has been discovered that new shift memory effects have been measured in tissue [98]. Existing phase mask simulations of memory correlations do not model the propagation of light rigorously, and underestimate memory effect ranges [97]. It is believed that more physically rigorous simulations of light propagation might be able to model the underlying physics more accurately, and better match theory [99].

Compare shaping algorithms under identical conditions: Experimental studies of WFS are affected by noise, motion artefacts, thermal drift, etc. In contrast, computational models can isolate these effects as desired. By doing so, it becomes possible to investigate WFS phenomena such as the performance of various shaping

algorithms. For example, Fayyaz *et al.* used simple random phase screen models to [100, 51] quantify how five different WFS algorithms were able to generate an optical focus through turbid media, creating plots of focus enhancement vs iteration count. They were then able to add noise to the model, investigating the resilience of each algorithm to noisy data. However, simple models of light propagation might not work on the newer physics and/or deep learning-based techniques to generate a focus (see Section 2.2.1.4).

Evaluate performance limits under ideal conditions: Computational models allow researchers to simulate WFS under idealised conditions that are difficult or impossible to achieve experimentally. For example, Yang *et al.* used an angular spectrum-based random phase screen model to simulate DOPC through scattering media [91]. They investigated how the peak-to-background ratio of the resulting optical focus depends on the SNR of the detection camera. This work demonstrates how computational modelling can define practical limits for experimental WFS systems, such as required detector performance. While the model used was not physically rigorous, more advanced full-wave simulations could extend these investigations to include realistic tissue-like scattering.

Having established the value of computational modelling for investigating WFS and related coherent phenomena, the remainder of the chapter discusses the theory and design of models of WFS and light propagation. This begins with an evaluation of the existing attempts to model WFS.

2.3.2 Existing attempts to model wavefront shaping

Existing computational models are limited in either efficiency or accuracy, and while viable at answering particular research questions, they may struggle when applied to others.

For example, coherent Monte Carlo has been used to render speckle and investigate correlations through turbid media [101]. Likewise, random phase screens have been used to investigate how imaging system parameters affect the peak-to-background

ratio of a generated focus [102]. However, neither method rigorously models turbid media, relying either on second-order statistical descriptions of the medium to describe light propagation or confining scattering to discrete two-dimensional planes. It is difficult to quantify the impact of these simplifications as propagating light fields cannot be visualised experimentally. Instead, derived metrics are used to describe both the medium (optical properties) and light propagation (speckle statistics). Therefore, simplified models of light propagation may be unreliable at modelling coherent phenomena that are heavily reliant on complex interference interactions through a medium, such as WFS or internal speckle analysis.

Conversely, the full-wave FDTD method has been used to explore how WFS could increase the penetration depth of OCT [62]. The FDTD method is physically rigorous but computationally inefficient, and as such has been applied to model an imaging modality that operates at a depth of a few hundred microns. Moreover, at these depths (less than a transport mean free path), it is unlikely that true WFS is required to generate a focus; instead, adaptive optics can be used to correct aberration in a focused beam.

Ultimately, there remains a challenge to rigorously simulate coherent visible and NIR light propagation through *"tissue-like"* media of specific optical properties to model light focusing or speckle correlations.

2.3.3 Methods of modelling biological tissue

2.3.3.1 What makes a model *"tissue-like"*?

Scattering in biological tissue arises from microscopic inhomogeneities in the refractive index, such as cell membranes, organelles, and extracellular structures (see Section 2.1). In principle, the most physically rigorous way to model light propagation through tissue would be to use a complete three-dimensional volumetric map of the refractive index distribution. However, despite recent advances such as using neural fields to generate volumetric refractive index maps [103], generating such maps with sufficient resolution and accuracy remains challenging. Consequently,

it is necessary to develop generalisable models of tissue that do not rely on exact structural data but can still reproduce the aggregate scattering behaviour observed in biological media.

However, by what standard is it possible to claim a model is sufficiently *"tissue-like"*? To this end, 10 key criteria have been identified to help define how accurate a model is at representing biological tissue. These criteria can be seen in Figure 2.5.

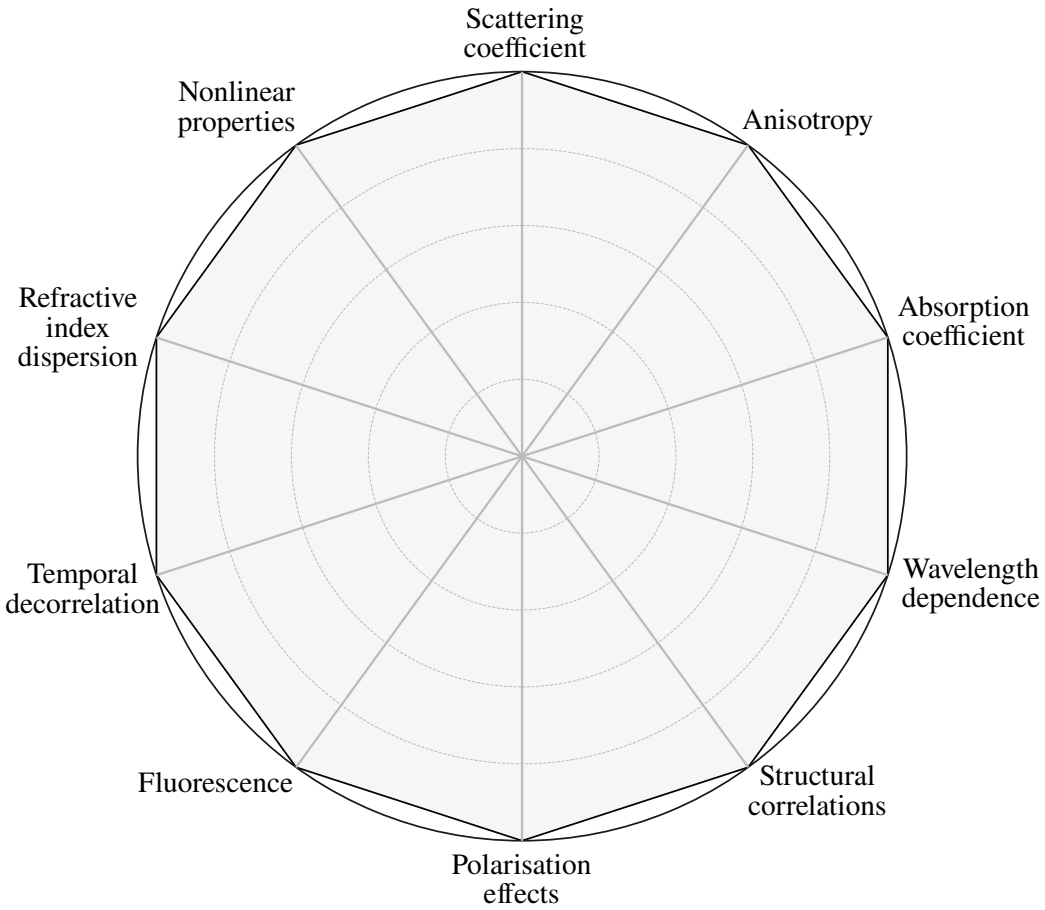

Figure 2.5: Radar plot template for evaluating the *"tissue-likeness"* of computational models across multiple optical dimensions. Each axis represents a distinct physical property relevant to light–tissue interaction. This plot can be used to assess how well a given model captures key features such as scattering, absorption, structural organisation, and dynamic behaviour.

The definitions for these criteria are stated below:

- **Scattering coefficient**
  - *What it is:* Describes how frequently light is scattered per unit distance in a medium.
  - *Why it matters:* Essential for predicting how far light penetrates tissue before becoming diffuse.
  - *How to assess:* Model reproduces measured μ_s values from experimental tissue data.
- **Anisotropy**
  - *What it is:* Describes the average direction of scattering; $g = 0$ is isotropic, $g \to 1$ is forward-scattering.
  - *Why it matters:* Strongly affects angular scattering distribution and transport mean free path.
  - *How to assess:* Model reproduces measured g values from experimental tissue data.
- **Absorption coefficient**
  - *What it is:* The amount of light absorbed per unit distance, typically due to chromophores like haemoglobin or melanin.
  - *Why it matters:* Essential for functional imaging, photoacoustics, and determining fluence distribution in tissue.
  - *How to assess:* Model reproduces measured μ_a values from experimental tissue data.
- **Wavelength dependence**
  - *What it is:* Variation of optical properties (μ_s, μ_a and g) with wavelength.
  - *Why it matters:* Real tissue is dispersive and wavelength-selective; multispectral imaging requires this behaviour.

  - *How to assess:* Model reproduces known spectral behaviour over visible and NIR range, consistent with empirical data.

- **Structural correlations**

  - *What it is:* Spatial relationships between scatterers (e.g. clustering, alignment, layering, size distributions).
  - *Why it matters:* Influences speckle patterns, coherence phenomena. Modelling inhomogeneous tissues.
  - *How to assess:* Model captures realistic speckle statistics and spatial autocorrelation observed in coherent imaging modalities.

- **Polarisation effects**

  - *What it is:* Changes to the polarisation state of light as it propagates through tissue (e.g. depolarisation, birefringence).
  - *Why it matters:* Important for polarisation sensitive OCT and polarimetric sensing.
  - *How to assess:* Model retains or depolarises polarised light in a way consistent with tissue-specific measurements.

- **Fluorescence**

  - *What it is:* Light emission from fluorophores in response to absorption of the incident light.
  - *Why it matters:* Contrast mechanism in fluorescence microscopy and molecular imaging. Potential guidestar.
  - *How to assess:* Model includes realistic fluorophore distributions with proper emission profiles.

- **Temporal decorrelation**

  - *What it is:* Changes in the optical scattering environment over time, due to motion, flow, etc.

  - *Why it matters:* Affects WFS focus stability, speckle correlation, and time-resolved techniques like diffuse correlation spectroscopy.
  - *How to assess:* Model produces realistic decorrelation timescales.

- **Refractive index dispersion**
  - *What it is:* Wavelength-dependent variation in the refractive index across the medium.
  - *Why it matters:* Impacts chromatic aberrations, phase shifts, and coherent interference in broadband systems.
  - *How to assess:* Model applies realistic dispersion laws for biological media.

- **Nonlinear properties**
  - *What it is:* Optical response that depends nonlinearly on field, e.g. two-photon excitation.
  - *Why it matters:* Essential for simulating specific nonlinear imaging modalities.
  - *How to assess:* Model includes accurate nonlinear effects and interactions.

Ultimately, the threshold for determining whether a model is sufficiently *"tissue-like"* is not absolute, but rather depends on the specific research questions being addressed. For example, studies investigating fluorescence or polarisation-resolved imaging require models that accurately represent these optical phenomena. Conversely, if the aim is to investigate the development of speckle or memory effects, structural correlation and anisotropy become more critical. The ten criteria outlined above provide a systematic framework for evaluating the strengths and limitations of different models. In the following section, this framework is applied to assess several existing modelling approaches and define the requirements of a model suitable for investigating WFS.

2.3.3.2 Random phase screens

One of the simplest representations of a scattering medium is the random phase screen [104, 105]. In this model, the internal structure of biological tissue is abstracted as a series of sequential two-dimensional planes of spatially varying phase delays. These phase screens introduce randomised optical path differences that generate speckle-like behaviour in the transmitted field.

The spacing between phase screens, and the spatial variation and distribution of phase delays across each screen, is arbitrary and often generated using model fitting. For example, Yang *et al.* tuned the standard deviation of refractive index fluctuations in each phase screen layer to control the scattering strength [102]. They did this by fitting the model to a desired transport mean free path by measuring the decay of the ballistic component in the simulated k-space intensity distribution [102]. The medium doesn't have a true scattering coefficient and anisotropy, and absorption is not modelled.

Random phase screens are used because they couple well with computationally efficient light propagation simulations (see Section 2.3.5). As such, they are often used to model speckle formation and focus generation [102], and memory effects [106]. However, the model lacks physical realism and cannot be tuned to match the bulk optical properties of real tissue, limiting the generalisability and constraining what research questions can be answered.

2.3.3.3 Macroscale statistical models

A common approach to representing biological tissue is to treat it as a statistically homogeneous medium described by bulk optical properties. In this representation, the microscopic structure of the tissue is not modelled explicitly; instead, tissue is characterised by parameters such as the scattering coefficient, anisotropy, and absorption coefficient.

These parameters are measured experimentally and assumed to be broadly homo-

geneous across the medium. These models are the basis of radiative transport and diffusion models, including the Monte Carlo method [107]. In such computational methods, bulk scattering is treated as probabilistic, rather than the deterministic result of a multitude of individual scattering events arising from refractive index inhomogeneities (see Section 2.1).

When evaluated against the previously established criteria, these models perform well at matching μ_s, g, and μ_a. However, they lack any structural correlation, do not support interference, and are unable to model polarisation, fluorescence, or decorrelation. As such, they are well-suited for modelling energy transport and diffuse optical imaging, but are limited in applications that depend on phase, like WFS. The methods used to simulate light transport through such bulk-property domains are discussed in Section 2.3.5.

2.3.3.4 Continuum model

In the continuum model, tissue is represented as a volumetric refractive index distribution discretised over a 3D simulation domain [108]. Scattering arises from random fluctuations in the refractive index, which perturb the phase and direction of incident light as it propagates through the medium. The spatial distribution of these refractive index inhomogeneities (both in size and smoothness) describes the macroscale nature of scattering inside the medium. For example, models based on the Kolmogorov spectrum of frozen turbulence [109] can be used to generate refractive index fields with realistic spatial structure.

Continuum models are particularly well suited to simulating large, inhomogeneous domains, where gradual refractive index variations may better reflect the mesoscale organisation of tissue compared to discrete models. Moreover, these models are compatible with polarisation and coherence-sensitive simulations. This is because they can be coupled with full-wave simulations of light propagation, as discussed in Section 2.3.5.

However, a key limitation is that the parameters defining the refractive index distribution (e.g., standard deviation, size) are not directly tied to macroscale tissue optical properties, such as the scattering coefficient or anisotropy. Instead, these domains must be carefully optimised, often through model fitting, to reproduce biological tissue as a pseudorandom assembly of individual scattering particles, typically spheres, although other axisymmetric geometries have been used. This fitting process must be repeated if the simulation geometry is changed, and no convenient mapping exists between continuum parameters and optical measurements.

2.3.3.5 Discrete particle model

The discrete particle model represents biological tissue as a pseudorandom assembly of individual scattering particles, typically spheres, although other axisymmetric geometries have been used [110, 111]. Unlike continuum models, where refractive index varies continuously, the discrete particle model assigns refractive indices to each particle, and tunes bulk optical properties by varying the particle's radii, refractive index contrast, and spatial density [20].

A major advantage of this approach is that the parameters defining the domain are analytically coupled to key optical properties (such as scattering coefficient and anisotropy) via Mie theory [112]. This enables researchers to construct domains with bespoke *"tissue-like"* scattering characteristics without iterative model fitting. For this reason, discrete particle models have been widely used in the design of physical phantoms that mimic biological tissue [113].

To more accurately represent the scattering behaviour of real tissue, particle size distributions can be introduced in place of fixed radii. It has been shown that any target scattering phase function can, in theory, be approximated by selecting an appropriate distribution of particle sizes and refractive indices [114]. One well-known implementation is the skewed log-normal distribution model proposed by Schmitt and Kumar, which reproduces not only realistic values of μ_s and g, but also captures their wavelength dependence [115].

Evaluated against the criteria in Figure 2.5, discrete particle models perform well at reproducing scattering and anisotropy, and can incorporate spectral dependence by combining Mie theory with size and index dispersion [115]. They can also approximate structural correlation, depending on how particles are spatially arranged, and are compatible with full-wave simulation methods that support polarisation and coherent interference (see Section 2.3.5). Dynamic decorrelation can be simulated by moving select particles - although model fitting is needed to relate this motion to *"tissue-like"* decorrelations. However, discrete particle methods do not account for fluorescence and may struggle to resolve microscale features in the biological tissue.

2.3.4 Requirements of a model of biological tissue to simulate wavefront shaping

A computational simulation of WFS is only as valid as the domain through which light is propagated. Accurately modelling WFS and other coherent phenomena requires that the simulation domain captures not only the appropriate scattering statistics but also the underlying physics that govern coherent light–tissue interactions. As discussed in Section 2.3.3, evaluation criteria for determining a model's *"tissue-likeness"* were created and multiple methods of representing biological tissue were discussed.

To evaluate a given model, it must be decided which of the 10 evaluation criteria are relevant. To do this, the research questions defined in Section 2.3.1 are considered. E.g. how can computational modelling help WFS? Ultimately, this model intends to simulate the formation and propagation of speckle, generate optical foci inside and through bespoke scattering media, and evaluate focus quality and enhancement. Therefore, the following requirements are defined:

1. The model must support the design of domains with bespoke optical properties, including a specified scattering coefficient μ_s and anisotropy factor g.

Absorption can be neglected for now, as $\mu_s \gg \mu_a$ (see Section 2.1). While this thesis focuses on these properties, other applications may demand additional characteristics, such as chirality, polarisability, or nonlinear effects.

2. To maintain physical realism, scattering within the domain must arise from microscale refractive index inhomogeneities. Models that treat scattering statistically (e.g., through bulk transport parameters or phase functions) without resolving the underlying structure are excluded. The goal is to enable a first-principles treatment of light propagation where phase, interference, and local field effects are preserved.

3. The model must allow for spatially unconstrained scattering. Refractive index inhomogeneities must be distributed throughout the volume, rather than confined to discrete interfaces or planes, so that volumetric scattering and focus formation can be realistically simulated.

4. The model must be geometrically flexible. Although the computational burden increases with complexity, the method must support domains of arbitrary shape and size in principle, enabling simulations in heterogeneous geometries where appropriate.

These criteria define our minimum level of physical rigour required for a model of biological tissue to simulate WFS.

2.3.5 Methods of modelling light propagation

Understanding the nature of light propagation through scattering media is a fundamental challenge in biomedical optics. A variety of numerical methods have been developed to simulate this process, each with differing assumptions, computational requirements, and physical rigour. These methods range from full-wave electromagnetic solvers that directly solve Maxwell's equations, to statistical transport models that track photon propagation stochastically, to simplified phase screen approaches that approximate light scattering through thin layers.

The choice of computational method depends strongly on the simulation domain (see Section 2.3.3). Not every computational method is compatible with every domain. Other considerations can also be related to Figure 2.5, namely, how physically rigorous must the overall model be to answer the desired research questions? Full-wave methods are typically required when coherent effects such as interference, speckle formation, or phase conjugation are important. In contrast, statistical or transport-based models are better suited for simulating diffuse light transport in large volumes, where individual scattering events are not resolvable.

This section provides an overview of the main modelling approaches used to simulate light propagation through biological tissue.

2.3.5.1 FDTD, FEM and BEM

The finite-difference time-domain (FDTD) method, the finite element method (FEM), and the boundary element method (BEM) [116] are all rigorous full-wave solvers that directly solve Maxwell's equations [116]. Given sufficient computational resources, these methods could, in principle, model infinitely large continuum and discrete particle systems. While highly accurate and generalisable, these methods differ in how they discretise space and manage computational resources.

FDTD discretises space and time using Yee cells and solves the equations explicitly in time [117, 118]. The method scales linearly with grid size [119]. Techniques such as perfectly matched layers have been developed, allowing the simulation to absorb outgoing waves without reflection [120]. However, FDTD requires a fine grid resolution - typically 8–16 cells per wavelength [121]. This makes it prohibitively computationally expensive to simulate light propagation through larger domains at visible and NIR wavelengths. However, pseudospectral methods somewhat circumvent this constraint, requiring only two cells per wavelength [122]. As Yee cells are cubic, they perform poorly when representing curved geometries, limiting their applicability to discrete particle models [123].

The FEM offers an alternative approach. It works by subdividing the computational domain into arbitrarily shaped finite elements, such as tetrahedra or pyramids, and solving the governing equations by minimising the weighted residuals across each element [124]. The FEM is better suited to handle complex geometries using unstructured meshing [125]. FEM is typically formulated in the frequency domain, although time-domain formulations do exist [124]. Unlike FDTD, FEM generally produces a system of linear equations that must be solved, which increases computational complexity. FEM is also more readily integrated with other physics solvers (e.g., thermal or mechanical models), making it attractive for multiphysics applications.

In contrast to both FDTD and FEM, the BEM is an integral method that solves Maxwell's equations on the surface of the computational domain rather than throughout the entire volume [126]. This surface-only discretisation makes BEM highly efficient for homogeneous domains with simple internal structure and low surface-area-to-volume ratios (e.g. simulating antennae) [119]. However, the BEM is poorly suited for modelling complex, inhomogeneous volumes such as biological tissue.

These full-wave methods prioritise physical rigour over computational efficiency. This restricts their practical application to small domains or idealised problems.

2.3.5.2 T-matrix method

The T-matrix method is an extension of classical Mie theory, enabling the simulation of light scattering from a collection of spherical particles [127]. While Mie theory describes the scattering of a plane wave by a single sphere, the T-matrix method generalises this to multiple scatterers by accounting for the interactions between each sphere [127]. The method can also be adapted to accommodate non-spherical particles [111].

The central idea of the T-matrix method is that the total electromagnetic field

within the domain can be expressed as a superposition of the incident field and the fields scattered by all other particles. This leads to a system of linear equations that describes the mutual scattering interactions between particles [128]. This system of linear equations can be solved directly for small systems (e.g. LU decomposition) or using iterative methods (e.g., generalised minimal residual (GMRES) or the biconjugate gradient stabilised method (BiCGSTAB)) for larger systems. Preconditioners [129] or fast multipole techniques [130] can be used to accelerate this solution.

The T-matrix method has several important advantages over other full-wave solvers. The majority of the computation is analytical (Mie theory), which enables high numerical accuracy [131]. Moreover, the method only requires solving for the unknown coefficients on the surfaces of the particles. The space between spheres does not need to be simulated, resulting in reduced memory usage and lower CPU demand compared to volume-discretisation methods like FDTD or FEM [132].

Another valuable property of the T-matrix approach for WFS applications is that the solved T-matrix for a given domain remains valid for any incident field. This means that arbitrary wavefronts can be simulated without recomputing the domain-specific scattering matrices, enabling efficient evaluation of multiple input modes and incident directions [131]. This makes the T-matrix method especially well-suited for studying focus formation and optimisation in static scattering domains.

2.3.5.3 Monte Carlo method

Unlike full-wave solvers, which construct optical properties from the geometry and refractive index of individual scatterers, the Monte Carlo method takes a statistical approach by modelling light transport through bulk optical properties [107]. Rather than solving Maxwell's equations, the Monte Carlo method estimates the macroscopic behaviour of photons propagating through a medium using probabilistic rules.

In a typical Monte Carlo simulation, photon packets are launched into a scattering medium. Each photon propagates a random distance, determined by the extinction coefficient, before undergoing an interaction. Here, the photon may be partially absorbed and scattered into a new direction [133]. This process is repeated iteratively until the photon is either absorbed completely or exits the domain. By tracking a large number of photon paths, it becomes possible to estimate the transmission of light through scattering media.

Conventional Monte Carlo methods do not capture interference or coherence effects. Because the scattering medium is treated statistically and not resolved at the microscale, phenomena such as speckle formation, coherent backscattering, and WFS cannot be simulated.

To address this limitation, Bar *et al.* proposed a Monte Carlo framework capable of synthesising speckle patterns based on statistical speckle correlations [101]. Their method allows for the generation of speckle patterns and can reproduce memory effects, all while remaining significantly faster than full-wave techniques. While this method provides a useful approximation, it lacks a direct physical connection to the underlying microstructure and the distribution of refractive indices. As a result, there is a risk that the method may not generalise to scenarios where the statistical model deviates from actual *in vivo* scattering behaviour.

2.3.5.4 The angular spectrum method

The angular spectrum method simulates light propagation by decomposing an incident wavefront into a spectrum of plane waves using a Fourier transform [134]. Each plane wave component is then independently propagated through space. An inverse Fourier transform is subsequently applied to reconstruct the light field at a given propagation depth [134]. This sequence of Fourier and inverse Fourier transforms allows the method to model free-space propagation and diffraction with high computational efficiency.

When a refractive index variation is introduced into the medium, each plane wave accumulates a different phase shift as it propagates. Over multiple steps, these phase shifts interfere to produce a speckle pattern. This behaviour has been used to simulate scattering through *"tissue-like"* media, including large domains up to 8 mm thick [102].

However, the method does not simulate scattering in a physically realistic manner. Rather than deriving scattering from microstructural refractive index inhomogeneities, refractive index variations are introduced statistically across a plane. These spatially varying indices are usually defined by sampling from a Gaussian distribution and model fitting. For example, the standard deviation of this distribution is optimised such that the propagation of light resembles light propagating a transport mean free path [102]. This model fitting is not directly tied to physical structure or any actual refractive index distributions. Instead, it is determined by angular spectrum-specific design parameters such as the spacing between propagation planes and the discretisation used in the Fourier transforms.

As a result, while the angular spectrum method can model scattering and WFS in large domains, it does so by sacrificing physical rigour. This limits its applicability in studies requiring accurate phase interactions or structural correlations.

2.3.5.5 Modified Born series

The Modified Born Series (MBS) is a frequency-domain method for solving the inhomogeneous Helmholtz equation, designed to simulate light propagation through large, strongly scattering media [92]. Unlike finite-difference methods, MBS uses a Fourier-based approach that avoids numerical dispersion and converges rapidly.

However, the MBS only simulates scalar fields and does not account for vectorial effects such as polarisation. Work on the MBS is still ongoing, and recent developments have dramatically lowered the memory requirements of the simulation by decomposing the problem over smaller sub-domains [135].

2.3.6 Requirements of a model of light propagation to simulate wavefront shaping

There is a need to develop a computational model for WFS that is accurate, tractable, and efficient, combining the best qualities of full-wave and ansatz modelling approaches. Such a model of WFS would be directly useful for model-based wavefront shaping [91], but could also be used to answer fundamental questions about the nature of WFS, such as limitations of generating optical foci or visualisation of shaped fields inside turbid media (see Section 2.3.1).

To answer such questions in deep tissues, a model of WFS must have particular design requirements. First, such a model should respect the wave nature of light by preserving phase, considering WFS is an interference-based phenomenon. Similarly, light propagation should be simulated rigorously, acknowledging that macroscale scattering behaviour is a result of microscale refractive index inhomogeneities. To ensure generalisability, the model should be capable of representing arbitrary scattering media. Moreover, this computational method should also be capable of efficiently modelling large volumes, allowing simulations at depths equal to or exceeding the transport mean free path of a medium of interest. This is the limit where light propagation becomes diffuse, and WFS holds the greatest potential benefit to biomedical imaging.

2.4 Chapter summary

As defined in Section 1.3, the broad aim of this thesis is to construct a new computational framework for simulating coherent light propagation through bespoke scattering media (including biological tissue) and then using this framework to model WFS.

To this end, this chapter began with a discussion on the nature of light propagation through biological tissue. The theory used to quantify the optical properties of tissue was described and defined for a generic tissue. The deleterious effects of

scattering were then discussed. This led to a discussion on a promising method to mitigate the effects of scattering - WFS. The theory of WFS was reviewed, as well as the applications and challenges of the method.

The computational modelling of WFS was then discussed. This required first defining the methods of representing biological tissue *in silico*, and the requirements of the model used to construct the proposed computational framework. Similarly, existing computational methods of modelling light propagation were also discussed. A literature review was undertaken on the existing attempts to model WFS. This led to the requirements of the computational framework being defined.

In the next chapter, a method of simulating light propagation was selected that meets the requirements defined in Section 2.3.6 - known as the T-matrix method. The method is explained, and the process of implementing the existing T-matrix codes is documented. The method is validated against Mie theory and the FDTD.

Chapter 3

Simulating light transport using the T-matrix method

A computational framework capable of modelling WFS must first be able to model light propagation through scattering media. This, in turn, requires two things: a method of modelling the propagation of light, and a method of modelling the scattering media. The requirements of these two methods are defined by the research questions being asked of the computational framework, which are defined in Sections 2.3.4 and 2.3.6 respectively.

This chapter focuses on the first framework component - the ability to model light propagation. The requirements of this model are defined in Section 2.3.6. The T-matrix method was selected because it is physically rigorous enough to model WFS and other interference-based coherent phenomena, while also being computationally efficient enough to simulate visible and NIR light propagation through media at least a TMFP thick. This is because, unlike approximate models, it explicitly solves Maxwell's equations, preserving the phase information essential for interference-based processes such as speckle formation and WFS. At the same time, by exploiting analytic solutions for single spheres and coupling them through VSWFs, the method avoids the volumetric discretisation required by approaches such as FDTD or FEM. This makes it tractable for simulating domains at or beyond a TMFP while still resolving the full electromagnetic field.

Structurally, this chapter begins with a background section that introduces the T-matrix method, before formalising the theory behind the method. Specifically, to model WFS, this requires explaining how the T-matrix method is capable of solving Maxwell's equations to calculate scattered near-fields. The chapter then presents the process of implementing existing T-matrix solvers, including the numerical considerations and modifications made to support the simulations in this thesis. This is followed by a validation section, where results are compared against Mie theory and FDTD solutions. The chapter concludes with a summary of contributions and a discussion of how the framework may be extended in the future.

3.1 Background

The T-matrix (transition matrix) method is a computational approach for wave scattering that originated in the mid-1960s. It was introduced by Peter C. Waterman, who in 1965 formulated a matrix-based method for solving electromagnetic scattering problems [128]. Waterman's 1965 paper established the core idea of expanding fields in spherical wave functions and relating the incident and scattered field coefficients via a *"transition matrix"* [136, 137].

Over the past decades, the T-matrix method has found application across various disciplines. In atmospheric science, it has been used to compute the scattering of aerosols [138], cloud droplets [139], and ice crystals [140]. In astrophysics, it has supported the study of cosmic dust [141], and planetary regoliths [142]. A reference database article is published annually, documenting new advances and applications of the T-matrix method [143, 144, 145, 146, 147, 148, 149, 150, 151, 152].

The T-matrix method itself is built on an analytical expansion of electromagnetic fields. In this formalism, both the incident and scattered fields are represented in a basis of vector spherical wave functions (VSWFs) [136]. The relation between the expansion coefficients of the incident field and those of the scattered field is linear,

with the linear operator given by the transition matrix. Effectively, the transition matrix connects how an incoming wave is transformed into a scattered wave by the presence of an object, with its elements (called scattering coefficients, not to be confused with μ_s) determined by the scatterer's properties (shape, size, and refractive index).

This scattering object can be an arbitrarily shaped particle. A significant branch of T-matrix research is concerned with determining novel methods for treating these non-spherical scatterers [131]. Extensions of the original formalism have incorporated spheroids, cylinders, spheroidal aggregates, and even irregular geometries through numerical surface discretisation. These advances exploit either the direct computation of non-spherical single-particle T-matrices or hybrid methods that couple T-matrix expansions with finite-element or boundary-element solvers. Some T-matrix solvers, such as SMARTIES (Spheroids Modelled Accurately with a Robust T-matrix Implementation for Electromagnetic Scattering) [153], are designed to model non-spherical particles. However, this thesis focuses on spherical scatterers. The reasons for this will become clearer in Chapter 4, which discusses the second component of the modelling framework - representing scattering media.

Critically for this thesis, the T-matrix method was later extended through the superposition T-matrix formalism, which enables modelling of clusters of particles. In this framework, each particle is represented by its own T-matrix, and multiple scattering between particles is incorporated through translation addition theorems. This allows the total scattered field of an ensemble to be computed by solving a coupled system of equations. The superposition approach is central to modelling dense, turbid media such as those studied in this thesis.

Note that in some literature, the T-matrix formalisation used in this thesis is referred to as the Generalised Multi-particle Mie (GMM) solution or Generalised Lorenz-Mie Theory (GLMT) [154, 155]. This is because, in the case of spheri-

cal scatterers, the eponymous transition matrix is not calculated using one of the methods described before, but instead derived directly from Mie theory, which is a semi-analytical solution to calculate the scattering of a plane wave by a sphere [112, 156]. In this thesis, the transition matrix is never actually calculated. Understandably, there is some division in the literature over the appropriate terminology for simulations of light propagation through multiple spherical scatterers - can such approaches be considered T-matrix simulations if the T-matrix is not calculated? This thesis uses the terminology and notation of Mackowski and Mishchenko [157], and as such considers spherical simulations as a subset of the greater T-matrix formalism (for example, the use of coefficients to represent the scattering particle, or the expansions using VSWFs).

3.2 Model theory

3.2.1 Constructing a system of linear equations

For this thesis, it is convenient to consider the T-matrix method as a generalisation of Mie theory to clusters of spheres [127]. As mentioned, this method exploits the linearity of Maxwell's equations to construct a system of linear equations that maps the scattered field from each sphere to every other sphere. A more comprehensive mathematical formalisation of the T-matrix method is provided by Mackowski and Mishchenko [158, 159, 160].

The total scattered field $\mathbf{E}_{\text{total}}$ is given by the superposition of the incident field and the scattered fields $\mathbf{E}^i_{\text{sca}}$ from each sphere i in the system [159] with N_s spheres:

$$\mathbf{E}_{\text{total}} = \mathbf{E}_{\text{inc}} + \sum_{i=1}^{N_s} \mathbf{E}^i_{\text{sca}} \tag{3.1}$$

To solve the scattering problem, the electromagnetic fields are expanded in a basis of vector spherical wave functions (VSWFs) centred at each particle (these are sometimes referred to as vector spherical harmonics (VSH) in literature). Around

each sphere i, the incident and scattered fields are written as:

$$\mathbf{E}^i_{\text{inc}}(\mathbf{r}) = \sum_{n=1}^{\infty} \sum_{m=-n}^{n} \left[p^i_{mn} \mathbf{M}^{(1)}_{mn}(k\mathbf{r}^i) + q^i_{mn} \mathbf{N}^{(1)}_{mn}(k\mathbf{r}^i) \right] \tag{3.2}$$

$$\mathbf{E}^i_{\text{sca}}(\mathbf{r}) = \sum_{n=1}^{\infty} \sum_{m=-n}^{n} \left[a^i_{mn} \mathbf{M}^{(3)}_{mn}(k\mathbf{r}^i) + b^i_{mn} \mathbf{N}^{(3)}_{mn}(k\mathbf{r}^i) \right] \tag{3.3}$$

Here:

- $\mathbf{r}^i = \mathbf{r} - \mathbf{r}_i$ is the position vector relative to the center of sphere i,
- $\mathbf{M}^{(1)}_{mn}$, $\mathbf{N}^{(1)}_{mn}$ and $\mathbf{M}^{(3)}_{mn}$, $\mathbf{N}^{(3)}_{mn}$ are regular and outgoing VSWFs respectively,
- p^i_{mn}, q^i_{mn} are incident field expansion coefficients,
- a^i_{mn}, b^i_{mn} are unknown scattered field coefficients.

The unknown scattered coefficients a^i_{mn}, b^i_{mn} are linearly related to the incident coefficients p^i_{mn}, q^i_{mn} through the single-particle T-matrix $\mathbf{T}_i$. This matrix encodes the full scattering response of particle i, including its size, shape, and refractive index, and acts on the incoming VSWF modes to produce the scattered modes:

$$\begin{bmatrix} a^i_{mn} \\ b^i_{mn} \end{bmatrix} = \mathbf{T}_i \begin{bmatrix} p^i_{mn} \\ q^i_{mn} \end{bmatrix} \tag{3.4}$$

Which are expanded using VSWF to:

$$\begin{pmatrix} a^i_{mn} \\ b^i_{mn} \end{pmatrix} = \sum_{n'=1}^{\infty} \sum_{m'=-n'}^{n'} \mathbf{T}^i_{mn,m'n'} \begin{pmatrix} p^i_{m'n'} \\ q^i_{m'n'} \end{pmatrix} \tag{3.5}$$

For spherical particles, the T-matrix $\mathbf{T}^i$ is diagonal, and its non-zero elements correspond to the standard Mie coefficients:

$$\mathbf{T}^i_{mn,mn} = \begin{pmatrix} \bar{a}_n & 0 \\ 0 & \bar{b}_n \end{pmatrix} \tag{3.6}$$

Where $\bar{a}_n$ and $\bar{b}_n$ are the electric and magnetic Mie scattering coefficients of sphere i, defined in terms of spherical Bessel and Hankel functions. For spherical particles, these coefficients are directly calculable from Mie theory.

In a system of multiple spheres, each particle not only scatters the external incident field but also the fields scattered by all other particles. To account for this, the total incident field on sphere i must include contributions from all other scattered fields, translated into the coordinate system centred at $\mathbf{r}_i$.

This translation is achieved using the addition theorem for VSWFs, which allows outgoing modes from one centre to be expressed as regular modes at another. The addition theorem gives the total incident mode coefficients at sphere i as:

$$\begin{pmatrix} p^i_{mn} \\ q^i_{mn} \end{pmatrix} = \begin{pmatrix} p^{(0),i}_{mn} \\ q^{(0),i}_{mn} \end{pmatrix} + \sum_{j \neq i} \sum_{k,l} \mathbf{U}^{ij}_{mn,kl} \begin{pmatrix} a^j_{kl} \\ b^j_{kl} \end{pmatrix} \tag{3.7}$$

Here, $\mathbf{U}^{ij}_{mn,kl}$ is the translation matrix that maps outgoing modes from sphere j to regular modes centred on sphere i, and $\mathbf{p}^{(0),i}$ is the external field incident on sphere i.

By combining the single-particle T-matrix relation with the translated contributions from other particles, a coupled system of equations for the scattered field coefficients a^i_{mn}, b^i_{mn} of all spheres is obtained.

Substituting Equation (3.7) into the single-particle scattering relation (Equation (3.5)) gives:

$$\begin{pmatrix} a^i_{mn} \\ b^i_{mn} \end{pmatrix} = \sum_{m',n'} \mathbf{T}^i_{mn,m'n'} \left[\begin{pmatrix} p^{(0),i}_{m'n'} \\ q^{(0),i}_{m'n'} \end{pmatrix} + \sum_{j \neq i} \sum_{k,l} \mathbf{U}^{ij}_{m'n',kl} \begin{pmatrix} a^j_{kl} \\ b^j_{kl} \end{pmatrix} \right] \tag{3.8}$$

To compactly represent the coupled system for all N_s spheres, a single linear system can be constructed containing all coefficients.

First, the scattered field vector $\mathbf{x}$ is defined as the vector that concatenates the unknown scattered coefficients from all spheres:

$$\mathbf{x} = \begin{bmatrix} \mathbf{x}^{(1)} \\ \mathbf{x}^{(2)} \\ \vdots \\ \mathbf{x}^{(N_s)} \end{bmatrix} \quad \text{with} \quad \mathbf{x}^{(i)} = \begin{bmatrix} a_{mn}^{i} \\ b_{mn}^{i} \end{bmatrix} \tag{3.9}$$

Secondly, the incident field vector is defined as the vector containing the VSWF expansions of the external field at each particle:

$$\mathbf{p}^{(0)} = \begin{bmatrix} \mathbf{p}^{(0),1} \\ \mathbf{p}^{(0),2} \\ \vdots \\ \mathbf{p}^{(0),N} \end{bmatrix} \quad \text{with} \quad \mathbf{p}^{(0),i} = \begin{bmatrix} p_{mn}^{(0),i} \\ q_{mn}^{(0),i} \end{bmatrix} \tag{3.10}$$

$\mathbf{T}$ and $\mathbf{U}$ are defined as block-diagonal matrices of the single-particle T-matrices and translation operators between spheres, respectively:

$$\mathbf{T} = \begin{bmatrix} \mathbf{T}_1 & 0 & \cdots & 0 \\ 0 & \mathbf{T}_2 & \cdots & 0 \\ \vdots & \vdots & \ddots & \vdots \\ 0 & 0 & \cdots & \mathbf{T}_N \end{bmatrix} \quad \mathbf{U} = \begin{bmatrix} 0 & \mathbf{U}^{12} & \cdots & \mathbf{U}^{1N} \\ \mathbf{U}^{21} & 0 & \cdots & \mathbf{U}^{2N} \\ \vdots & \vdots & \ddots & \vdots \\ \mathbf{U}^{N1} & \mathbf{U}^{N2} & \cdots & 0 \end{bmatrix} \tag{3.11}$$

Using these vectors and matrices, it is possible to rewrite Equation 3.8 as a system of linear equations in compact matrix form:

$$\mathbf{x} = \mathbf{T}\left(\mathbf{p}^{(0)} + \mathbf{U}\mathbf{x}\right) \tag{3.12}$$

Rearranging Equation 3.12 gives a matrix in the $Ax = B$ form:

$$(\mathbf{I} - \mathbf{T}\mathbf{U})\,\mathbf{x} = \mathbf{T}\mathbf{p}^{(0)} \tag{3.13}$$

The following Table is used to summarise the terms of the matrix system and whether they are known or unknown:

Table 3.1: Definitions of terms in the T-matrix system and whether they are known or unknown

Symbol	Description	Status
$\mathbf{I}$	Identity matrix	Known
$\mathbf{T}$	Single-particle T-matrices	Known (Mie theory)
$\mathbf{U}$	Translation matrix	Known (calculated by solver)
$\mathbf{x}$	Scattered field coefficients $[a^i_{mn}, b^i_{mn}]$	**Unknown**
$\mathbf{p}^{(0)}$	Incident field expansion coefficients	Known (for simple waves)

3.2.2 N-sphere system

For a system of two spheres, the matrix Equation 3.13 becomes:

$$\begin{bmatrix} \mathbf{I} & -\mathbf{T}_1\mathbf{U}^{12} \\ -\mathbf{T}_2\mathbf{U}^{21} & \mathbf{I} \end{bmatrix} \begin{bmatrix} \mathbf{x}^{(1)} \\ \mathbf{x}^{(2)} \end{bmatrix} = \begin{bmatrix} \mathbf{T}_1\mathbf{p}^{(0),1} \\ \mathbf{T}_2\mathbf{p}^{(0),2} \end{bmatrix} \tag{3.14}$$

While for a general system of N_s spheres, the matrix system (Equation 3.13) takes the form:

$$\begin{bmatrix} \mathbf{I} & -\mathbf{T}_1\mathbf{U}^{12} & \cdots & -\mathbf{T}_1\mathbf{U}^{1N_s} \\ -\mathbf{T}_2\mathbf{U}^{21} & \mathbf{I} & \cdots & -\mathbf{T}_2\mathbf{U}^{2N_s} \\ \vdots & \vdots & \ddots & \vdots \\ -\mathbf{T}_{N_s}\mathbf{U}^{N_s1} & -\mathbf{T}_{N_s}\mathbf{U}^{N_s2} & \cdots & \mathbf{I} \end{bmatrix} \begin{bmatrix} \mathbf{x}^{(1)} \\ \mathbf{x}^{(2)} \\ \vdots \\ \mathbf{x}^{(N_s)} \end{bmatrix} = \begin{bmatrix} \mathbf{T}_1\mathbf{p}^{(0),1} \\ \mathbf{T}_2\mathbf{p}^{(0),2} \\ \vdots \\ \mathbf{T}_{N_s}\mathbf{p}^{(0),N_s} \end{bmatrix} \tag{3.15}$$

3.2.3 Calculating the scattered field

Once the scattered coefficients a^i_{mn}, b^i_{mn} have been obtained for each sphere i, the total electric field at any spatial point $\mathbf{r}$ is given by the sum of the external incident field and the scattered fields from all particles (see Equation 3.1).

In practice (e.g., in T-matrix solvers like MSTM or CELES), the near-field is evaluated by numerically computing the VSWFs at desired field points and summing the contribution of each mode. Care must be taken near particle surfaces to

ensure convergence of the expansion.

One feature of the T-matrix method is that once the scattered coefficients have been solved, they can be stored and reused to compute the electromagnetic field at any desired location without re-solving the system. This contrasts with time-domain methods such as FDTD, which require a full re-simulation to obtain the field at different spatial locations or frequencies.

3.2.4 System dimensionality and numerical considerations

The size of the linear system in the T-matrix method depends on the number of spheres N_s and the truncation order L_s used in the VSWF expansions. The truncation order L_s defines the maximum multipole degree $n \in [1, L_s]$ included in the field expansions for each particle.

L_s can be estimated using the empirically derived Wiscombe's criterion [161]:

$$L_s = \begin{cases} x + 4x^{1/3} + 1, & 0.02 \leq x \leq 8 \\ x + 4.05x^{1/3} + 2, & 8 \leq x \leq 4200 \\ x + 4x^{1/3} + 2, & 4200 \leq x \leq 20000 \end{cases} \tag{3.16}$$

Where x is the size parameter of the constituent spheres, $x = \frac{2\pi r}{\lambda}$.

Each multipole order n contributes $2n+1$ azimuthal modes $m \in [-n, n]$, so the total number of modes per polarisation (either TE or TM) per sphere is:

$$M = \sum_{n=1}^{L_s} (2n+1) = L_s(L_s+2) \tag{3.17}$$

Including both polarisations, each sphere contributes:

$$2M = 2L_s(L_s+2) \tag{3.18}$$

unknown coefficients a_{mn}, b_{mn} to the system. For a system of N_s spheres, the total number of unknowns is:

$$T = 2N_s L_s(L_s + 2) \tag{3.19}$$

Where T is ultimately the total number of linear equations in the scattering system. These linear equations are what T-matrix solvers like MSTM and CELES spend the most computational resources solving.

Using Big $\mathcal{O}$ notation, Equation 3.19 scales as $\mathcal{O}(N_s^2 L_s^4)$. The scaling behaviour of different complexity classes is illustrated in Figure 3.1.

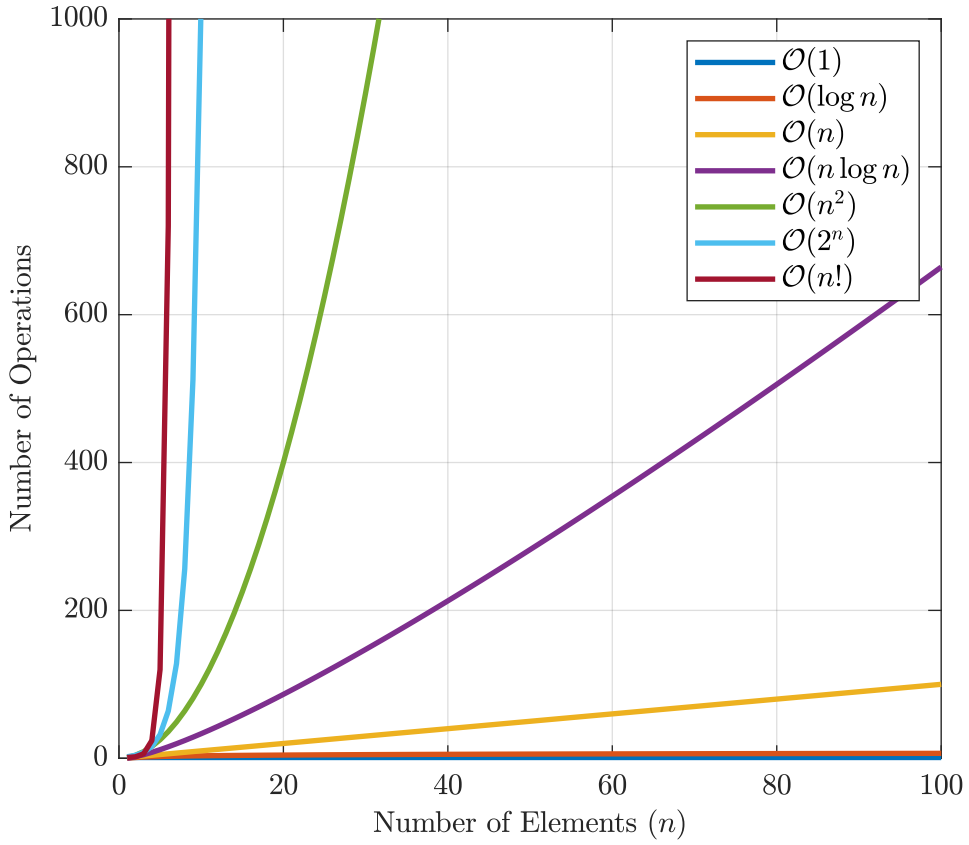

Figure 3.1: Illustration of common computational complexity classes using Big $\mathcal{O}$ notation. Each curve shows how the number of operations grows with input size (n). Big $\mathcal{O}$ notation characterises the upper bound of an algorithm's runtime or memory usage, helping to compare the scalability of different computational approaches.

As the number of particles increases, the global matrix becomes both dense and large, making direct inversion impractical. Instead, the system is typically solved using iterative Krylov-subspace methods such as GMRES or BiCGSTAB. This is the role of computational T-matrix solvers such as MSTM [138] and CELES [129].

Some T-matrix solvers, such as the most recent implementation of MSTM [162] and FastMM [163], incorporate the Fast Multipole Method (FMM) or similar techniques to reduce the scaling behaviour from $\mathcal{O}(N_s^2)$ to approximately $\mathcal{O}(N_s \log N_s)$. Others, such as CELES [129], use GPU acceleration and preconditioners to speed convergence. Specific T-matrix codes will be discussed in Section 3.3.1.

3.3 Implementation

3.3.1 T-matrix solvers

In general, a T-matrix simulation requires four categories of inputs:

1. the optical properties and positions of the scattering particles, typically specified as a list of spheres with defined radii, refractive indices, and 3D coordinates

2. the parameters of the incident light field, such as the type (plane wave, Gaussian beam, etc), width, wavelength, and incident angle

3. the spatial positions where the scattered or total field is to be evaluated, such as a near-field observation plane

4. simulation-specific parameters, including convergence thresholds, the number of multipole orders used in the expansions, numerical precision settings, and solver tolerances

As of 2025, there are multiple T-matrix codes available. The three most popular T-matrix codes are: the multiple sphere T-matrix (MSTM) [160], the CUDA-accelerated electromagnetic scattering by large ensembles of spheres (CELES) [129], and the fast superposition T-matrix method (faSTMM) [163].

Broadly speaking, the T-matrix method is less popular than other computational methods, and as such, these codes are not as well validated or feature-rich as solvers for other computational methods (e.g. Lumerical for FDTD or MCX for Monte Carlo). Existing codes are highly specialised in answering the research questions of interest to the authors. For example, the authors of faSTMM (Markkanen and Yuffa) are focused on astrophysics and wrote the software to simulate scattering by planetary and cometary regoliths [164, 165, 166]. Consequently, faSTMM has no functionality to calculate near fields or model incident Gaussian beams.

A table comparing the three codes is shown below. Note that a new version of MSTM was released in 2023 [162] that implements a Fourier-based acceleration method that achieves $\mathcal{O}(n \log n)$ scaling. However, there was insufficient time to validate this version of MSTM, and as such, it will not be discussed in this thesis.

T-matrix code	Language	Near field	Gaussian beams	Scaling	Parallelisation
MSTM	FORTRAN	Yes	Yes	$\mathcal{O}(n^2)$	MPI
CELES	MATLAB	Yes	Yes	$\mathcal{O}(n^2)$	OpenMP, CUDA
faSTMM	FORTRAN	No	No	$\mathcal{O}(n \log n)$	OpenMP

Table 3.2: Comparing the features of three different T-matrix codes: MSTM [160], CELES [129] and faSTMM [163]. Language is the primary programming language used to write the software. Near field calculation is the ability to evaluate the field at arbitrary locations. Gaussian beams refer to the ability to model the incident light field as a Gaussian beam. Shared memory parallelisation architectures like OpenMP are efficient for single machines with multicore CPUs. Multi-node clusters work better with MPI, where the memory can be distributed throughout the cluster.

Some functionality implications are immediately obvious from Table 3.2. For example, faSTMM does not have the ability to calculate near fields or model Gaussian beams. If these features are required to answer specific research questions, the functionality must be added by modifying the software.

Another practical implication is the software's programming language. I had experience with MATLAB, but was unfamiliar with FORTRAN, meaning any potential modifications would be more difficult.

An additional difference between the software was the method of parallelisation each employed. T-matrix simulations quickly exceed the capacity of a single CPU core, requiring parallelisation. Two models commonly used are MPI (Message Passing Interface) and OpenMP (Open Multi-Processing). MPI uses distributed memory: each process has its own memory allocation and communicates via message passing. Meanwhile, OpenMP uses shared memory: threads run within a single process and access the same memory.

MPI is well-suited to large simulations running on multi-cluster nodes, but incurs communication overhead. Conversely, OpenMP is efficient on multi-core workstations, with minimal communication costs, but is limited by the memory available on a single node.

CELES uses a unique method of parallel computing compared to MSTM and faSTMM, as some operations are performed on GPUs via NVIDIA's CUDA framework. The authors claim this improves the computational performance of the software relative to CPU-exclusive calculation. Obviously, this creates the requirement of a CUDA-compatible GPU to be able to run CELES.

Therefore, the computational hardware, both with respect to CPU and multi-node architecture and GPU availability, determines the viability of each T-matrix code.

3.3.2 Available computational hardware

Large-scale T-matrix simulations are computationally demanding. The superposition method involves solving dense, coupled linear systems whose size scales with both the number of particles and the maximum multipole order per particle, as described in Section 3.2.4. For ensembles approaching thousands of scatterers,

the number of unknowns can easily exceed 10^6, making simulations intractable on conventional desktop hardware. Moreover, near-field calculations require storing and evaluating field expansions at numerous observation points, which further increases both memory usage and runtime. In practice, efficient execution therefore relies on access to high-memory compute nodes and, for CELES, dedicated CUDA-compatible GPUs.

For this thesis, three systems were employed:

Zeus A workstation equipped with two Intel Xeon Gold 6148 CPUs (2.40 GHz), 128 GB RAM, and a NVIDIA Quadro P6000 GPU.

Mnemosyne A workstation with two Intel Xeon Gold 6148 CPUs (2.40 GHz), 512 GB RAM, and a NVIDIA Quadro P4000 GPU.

Myriad A high-performance cluster at UCL that offers multiple node types:

- Standard compute nodes (H, D): 36 cores, 192 GB RAM.
- High-memory nodes (I, B): 36 cores, 1.5 TB RAM.
- GPU nodes (J, E, F, L): 36 cores, 192GB RAM with attached GPUs.
  - J-type nodes include two Tesla P100s
  - E- and F-type nodes include two Tesla V100s
  - L-type nodes include four A100s

The CPUs on Myriad vary between Intel Xeon Gold 6140 (2.30 GHz) and Xeon Gold 6240 (2.60 GHz), depending on node type.

3.3.3 Placing spheres to create discrete particle volume

T-matrix codes require input data specifying the sphere origins, radii, and refractive indices. The implications of the placement of spheres and their properties will be

discussed in Chapter 4. For the purposes of testing the T-matrix method of modelling light propagation, a programme is needed to create a custom discrete particle volume and to format the input data appropriately for each T-matrix code.

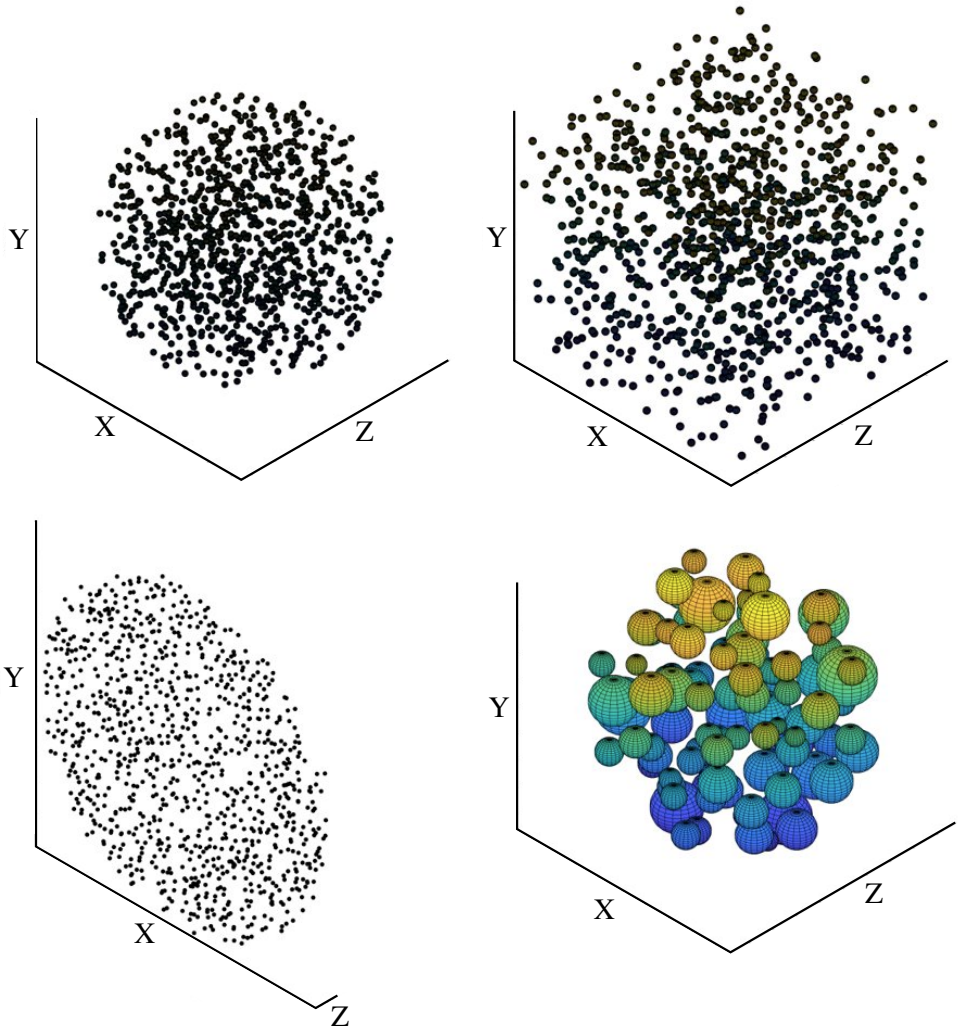

Figure 3.2: Example realisations of 3D discrete particle domains. Spheres are randomly placed in a bounding volume with a minimum separation to prevent overlaps and improve matrix conditioning. The sphere radius, density, refractive index, total sphere count, and constraining geometry can all be specified. Although not modelled in this thesis, different distributions can be used to define sphere radii. Shown in the bottom right is the lognormal distribution used by Schmitt and Kumar to model biological tissue [115].

Individual spheres were positioned manually for the most basic tests (for example, a 1 μm radius sphere located at the origin with a refractive index of 2. Full discrete particle volumes are constructed by pseudorandomly placing spheres at

non-overlapping locations within a 3D domain. This was achieved using a home-made algorithm that sequentially generated candidate sphere positions and rejected any that violated a minimum distance constraint. The constraint was set to prevent sphere overlaps and to ensure that the resulting T-matrix system was well-conditioned; when spheres are placed too close together, the translation matrices become poorly conditioned and numerical instabilities may arise. Sample domains generated using this technique are shown in Figure 3.2.

3.3.4 Initial code modification

All three T-matrix codes contained limitations or bugs that required modification before full simulations of light propagation could be performed.

For MSTM, the principal issue encountered was a concentric ring artefact when the background refractive index was set to any value greater than 1. The issue was corrected with the help of MSTM author Mackowski by applying a consistent scaling factor to either the particle radii and positions or the wavelength, equal to the background refractive index. This scaling factor was then reversed when calculating the near-field.

Most simulations in Mnemosyne and Zeus were performed using MSTM, which has a distributed memory architecture (MPI). This is suboptimal, as Zeus and Mnemosyne are single-node machines, and MPI is better suited to running simulations over multiple nodes. Initially, it was possible to brute force the bloated memory usage with Mnemosyne, which has a significant amount of RAM available. However, the near-field evaluation step became a bottleneck in both time and memory. Early in the PhD, runaway memory use caused Zeus to crash and terminate some of the group's already running simulations.

Therefore, an OpenMP-based parallelisation of the near-field calculation was implemented, which significantly reduced memory requirements. It also allowed for a more controllable allocation of threads to each process. As described in Section

3.2.3, near-field calculation is a post-processing step distinct from the determination of the scattered field coefficients. Moreover, near-field calculations are highly parallelisable; each thread can be assigned to calculate the field at a different set of coordinates using the solved scattered field coefficients and requires no communication with other threads. It was discovered that MSTM was using the same thread count and memory limitations for the calculation of the scattered field components as for the near-field computation. The OpenMP modification of the near-field function allowed for more threads to be assigned to the calculation, without the ballooning memory demands necessitated by MPI.

For CELES, early testing revealed three primary limitations or bugs. Firstly, there is an undocumented inability to model extremely large Gaussian beams beyond > 200 μm. This bug was discovered during a parameter space exploration and was not fixed, as there was no need to simulate Gaussian beams of this width. Secondly, a shadow-like artefact would be seen in the near-field around sphere boundaries when CELES' preconditioner option was used. This will be discussed in Section 3.4.2. Finally, the near-field could only be evaluated at 2D planes. A simple modification was performed to enable the calculation of near-field at multiple 3D positions throughout the medium, and to cache and reuse the scattered field coefficients from a given simulation if additional near-field calculations were ever required later.

Despite being considered, faSTMM was not used during the PhD beyond some early testing. This was because, despite having the best scaling behaviour, faSTMM does not have a method for generating near-fields or modelling Gaussian beams. To align it with the functionality of MSTM and CELES, a script was created to compute near-fields at arbitrary points from the solved scattered coefficients. This was done by passing the scattered coefficients to the CELES module used to calculate near-fields. Using existing CELES MATLAB code was deemed easier than working with the unfamiliar faSTMM FORTRAN code. However, further use of faSTMM stopped when access to Myriad became available. This was because

the GPU parallelisation with CELES was sufficiently efficient, and implementing Gaussian beam incident light seemed a prohibitive time sink in an unfamiliar programming language.

Finally, for both MSTM and CELES, wrappers were written to improve usability, functionality and streamline workflow. These in-house wrappers were written in MATLAB and included functionality to quickly save and load simulation data, dynamically visualise sphere position in 3D, and dynamically log the time and memory usage of the simulation. On the output side, the wrapper can process the near-field data to generate plots of electric magnitude and intensity at arbitrary locations.

3.3.5 Initial simulations of light propagation

Following the initial setup, the immediate aim was to model light propagation through a discrete particle domain, thereby enabling validation of the T-matrix implementation.

Zeus and Mnemosyne are both powerful lab-level machines capable of running medium-scale T-matrix simulations. Compilation, testing and modification of the T-matrix codes were significantly easier on both workstations, for which *sudo* access was available. Moreover, there was no need to queue up jobs or manage quotas, unlike UCL's Myriad. Therefore, both machines were primarily used for earlier prototyping simulations of light propagation, for example, testing code modifications or performing parameter space investigation. Large simulations were intractable, both due to the limited potential for parallelisation relative to Myriad, but also because computing time was shared with the other members of the Coherent Optics Group (COG) at UCL.

Early simulations on Zeus and Mnemosyne used MSTM over CELES for two reasons. Firstly, there was high utilisation of the GPUs required by CELES on both machines by other members of COG throughout the PhD. Conversely, CPU and

RAM utilisation were low, favouring a CPU-only MPI code like MSTM. Secondly, CELES was released in 2017 [129] by a research team not yet established in the T-matrix literature. As of the start of the PhD, the code was still being modified on GitHub, and errors were being fixed. Conversely, MSTM was programmed in 2011 by T-matrix veteran Mackowski [160], had been iterated into three (now four) versions, and has over 500 citations. During initial testing of the T-matrix method early in the PhD, MSTM was considered a more reliable option.

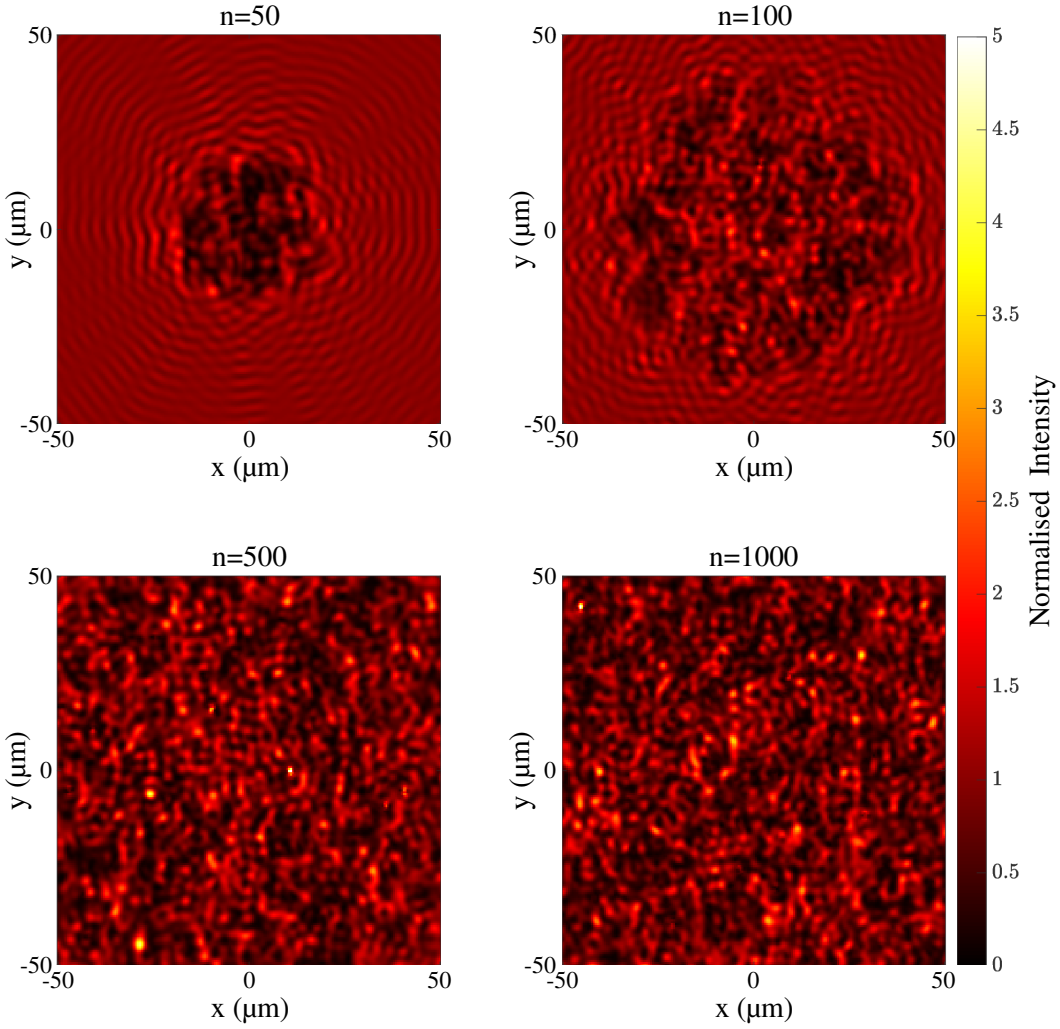

Figure 3.3: MSTM is used to simulate the propagation of a plane wave through 4 discrete particle volumes with 50, 100, 500 and 1000 spheres with a radius of 1 μm and a refractive index of 2. Shown here are the scattered field intensities on the 100 μm^2 plane located 5 μm behind the medium. The refractive index of the background is 1.

The first simulation was designed such that a 633nm plane wave was simulated

directly incident on a pseudorandom discrete particle medium consisting of 0.5 μm radius spheres with a refractive index of 2.5836 and a volume concentration of 0.25%. The background refractive index was set equal to 1. The intensity near-field was evaluated on a 100 μm^2 XY plane located 5 μm behind the medium. MSTM was used to perform the T-matrix calculation, and the results are shown in Figure 3.3 for domains with 50, 100, 500 and 1000 spheres.

As shown in Figure 3.3, the field behind the medium is perturbed. Across the observation plane, the field appeared as a seemingly random arrangement of bright and dark spots, arising from the constructive and destructive interference of multiply scattered waves. Local intensity maxima exceeded the incident field intensity due to constructive interference, while adjacent nulls approached zero intensity. As the number of spheres increases, the apparent field perturbation becomes more pronounced, taking a greater proportion of the visualisation plane.

Figure 3.4 shows a histogram of intensities for the 500 sphere simulation. A Rayleigh distribution was fitted to the normalised data, and showed a strong fit, indicating the speckle pattern had been fully developed [167]. This initial result demonstrates that the T-matrix method is capable of generating fully developed speckle patterns through discrete particle media.

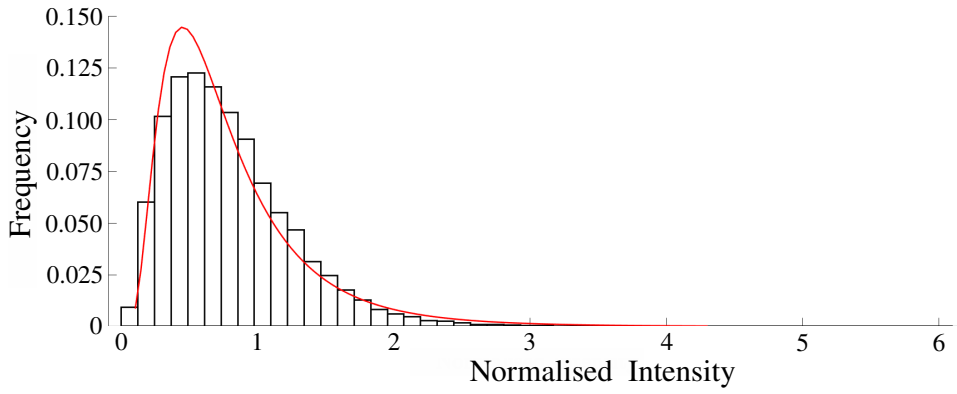

Figure 3.4: Histogram plot of the speckle pattern generated using 500 spheres shown in Figure 3.3. A Rayleigh distribution was fitted to validate that a fully developed speckle pattern has formed.

The simulation was repeated for a sphere count up to 10000 spheres, and clock time was measured with dstat. Simulations were run in parallel over four cores on Zeus with MSTM. This allows Figure 3.5 to be generated, which is a plot of clock time as a function of sphere number. Polynomial regression was used to determine a criterion for estimating the simulation time as a function of sphere count.

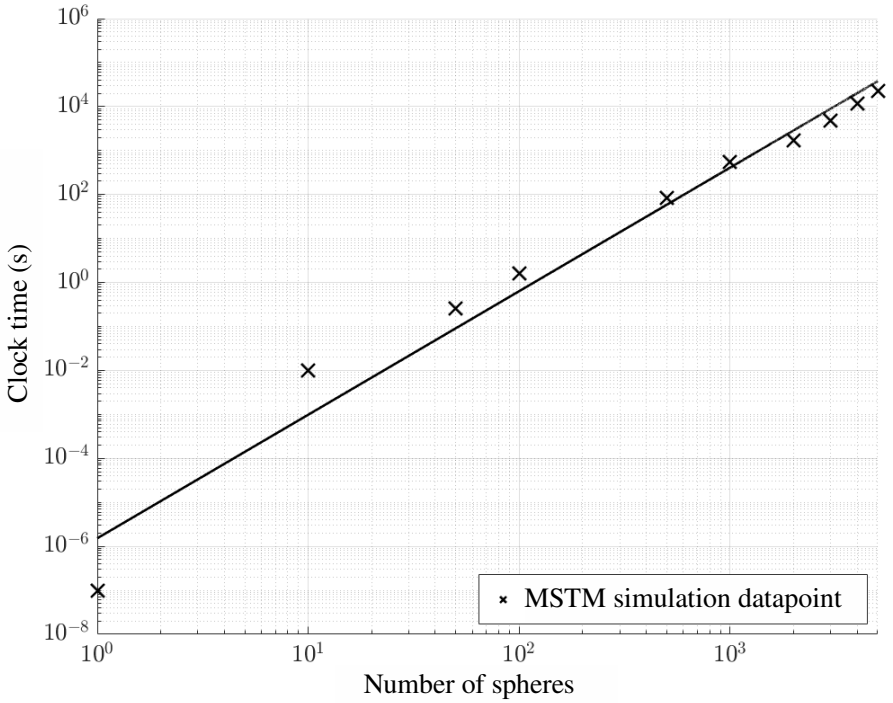

Figure 3.5: The clock time taken to simulate differently sized scattering domains in MSTM (radius = 1 μm). MSTM was run in parallel over four cores on Zeus, whose specs are listed in Section 3.3.2.

Note from Equation 3.19 that simulation time is a function of the number of spheres and the truncation order of the VSWF expansion, which in turn is a function of the radius and wavelength of the constituent spheres and incident light. Therefore, the data in 3.5 is not translatable to other discrete particle domains. Likewise, specific computational times are also a function of the simulation hardware and specific T-matrix settings, such as convergence thresholds or chosen precision.

For example, Myriad became available one year into the PhD and significantly accelerated computation times. Both CELES and MSTM calculations were per-

formed on Myriad, leveraging I and B nodes for MSTM and J, E, F, and L nodes for CELES.

Another computational consideration is that CELES uses OpenMP, which is a shared memory architecture. Initially, it may seem that it would run poorly on Myriad, which has many computational nodes. However, UCL guidelines recommend Myriad to be used for a large batch of serial jobs, instead recommending the Kathleen cluster for multi-node jobs.

As discussed in Section 3.3.1, T-matrix codes in general are not as refined as other computational toolkits. As such, a thorough parameter space exploration was a necessary precursor to validation, and ultimately, using the codes to model WFS and other phenomena. The parameter space refers to the full range of possible inputs for a given T-matrix code. This includes both optically relevant parameters, such as wavelength, refractive indices and sphere properties, and simulation-specific parameters, such as convergence thresholds and expansion orders.

These broad investigative simulations served three purposes. First, to develop familiarity with the T-matrix codebase. Second, to optimise machine-specific parameters such as CPU core count and memory allocation limits. Third, to identify (and correct) implementation-specific bugs.

For brevity, the vast majority of these parameter space exploratory simulations have been omitted from this thesis. Instead, a series of key results are highlighted documenting the discovery of an MSTM-specific artefact produced when the background refractive index is changed from $n = 1$. This artefact is shown in Figure 3.6.

The fields in Figure 3.6 are produced by using MSTM to simulate the propagation of a plane wave (633 nm) through a 100 μm^3 discrete particle domain, containing 1 μm spheres with a refractive index of 2 at a volume fraction of 0.05. The *"recipe"*

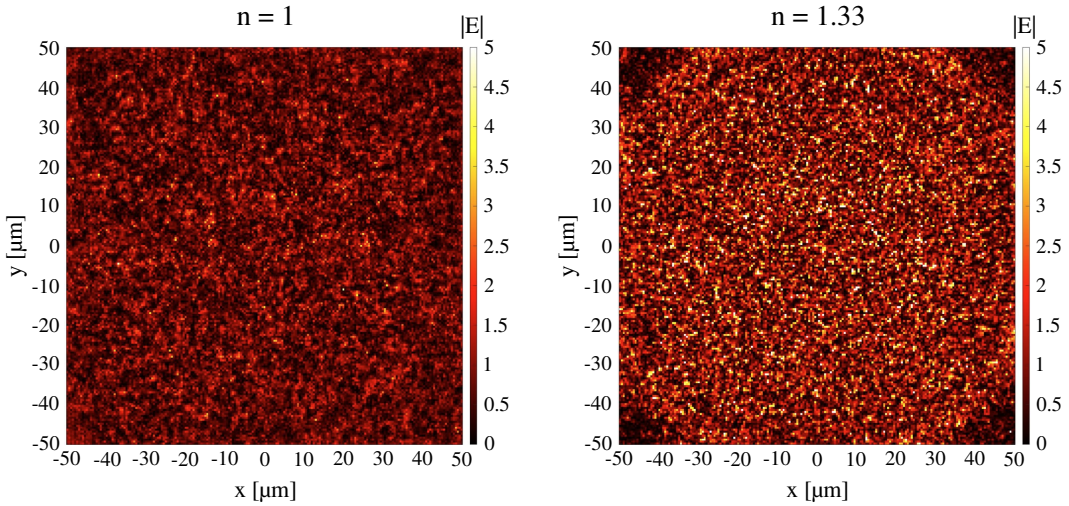

Figure 3.6: MSTM is used to simulate the propagation of light through a 100 μm^3 discrete particle volume. Shown here are the scattered fields on the 100 μm^2 plane located 5 μm behind the medium. The refractive index of the background is 1 for the left image and 1.33 for the right image.

of this domain was arbitrarily chosen as part of the parameter space exploration. The electric field magnitude is calculated and visualised across the 100x100 μm^2 plane located 5 μm behind the medium. This offset ensures that particles near the exit surface do not obscure the field pattern.

As shown in Figure 3.6, when the background refractive index is set to 1.33 (the refractive index of water), the resulting scattered field is clearly erroneous. A Gaussian-like field profile is observed rather than a fully developed uniform speckle pattern. Notably, the electric field magnitude is uniformly brighter than expected, given that the mean field amplitude of the input plane wave is normalised to 1. In contrast, a background refractive index of 1 (the refractive index of air) produces a plausible developed speckle pattern. A histogram of the field magnitudes across the plane follows a Rayleigh distribution (not shown), consistent with light scattering theory [167]. As expected, the magnitude is broadly lower nearer the edges due to light escaping from the sides of the simulation.

To isolate the root cause of the anomalous field seen with a background refractive index of 1.33, additional tests were run in a scattering-free environment. Since

MSTM requires at least one sphere in the domain, a single sphere was placed at the origin with its refractive index matched to the background medium. This setup is equivalent to simulating free-space propagation through a sphere-less medium. Both plane waves and Gaussian beams (633 nm) of varying widths were propagated through the domain for a background refractive index of 1 and 1.33. The magnitude of the electric field on a plane bisecting the domain at $z = 0$ is shown in Figure 3.7.

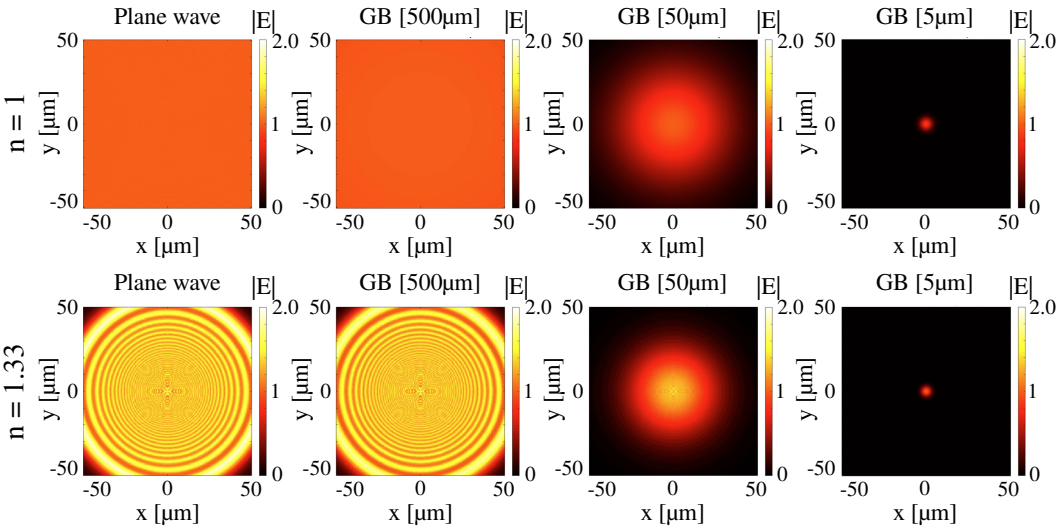

Figure 3.7: Free space plane wave and Gaussian beam (GB) propagation simulated using MSTM. The wavelength of the incident light was 633 nm, and the background refractive index was either 1 or 1.33 for the first or second row, respectively.

Figure 3.7 reveals a persistent error: simulations with a background refractive index of 1.33 produce anomalously bright fields with spatially structured artefacts. At large beam widths, and for the plane wave, concentric interference rings appear. This experiment was repeated for a range of refractive indices above 1, and the artefact was persistently present in the field (data not shown).

This issue was brought to the attention of MSTM author Daniel Mackowski, who confirmed the error and recommended a workaround. T-matrix and Mie theory are functions of the refractive index contrast of a given sphere. The ability to define the refractive index of a given sphere and the background independently is a convenient method of inputting data to T-matrix and Mie solvers. As the simulation is correct when the background refractive index is set to 1, simulating other background re-

fractive indices can be achieved by normalising the scatterer refractive indices and scaling the particle radii. For example, for a background refractive index of 1.33, all particle refractive indices should be divided by 1.33 and all radii multiplied by 1.33. Figure 3.8 shows the result of applying this correction.

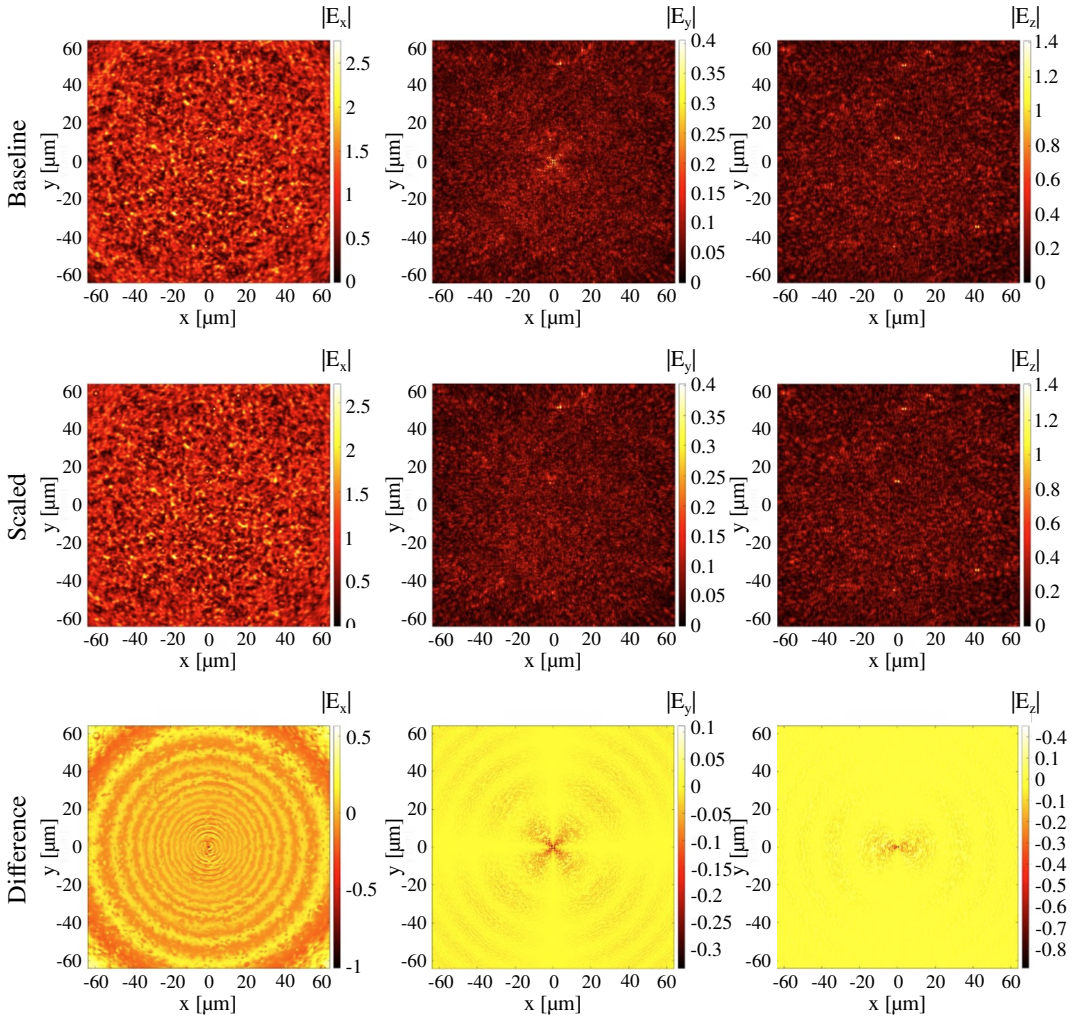

Figure 3.8: Correcting the concentric ring artefact in MSTM by applying a scaling fix. Plane waves (633 nm) are propagated through a discrete particle volume. The top row shows the unscaled field. The middle row shows the scaled, corrected field. The final row shows the difference between the scaled and unscaled simulations.

As shown, applying the scaling method eliminates the concentric ring artefact. The residual difference between corrected and uncorrected fields matches the artefact previously observed, confirming the fix's effectiveness.

3.4 Validation

3.4.1 Field comparison vs Mie

To ensure the accuracy of the T-matrix simulations, the first stage of validation involved comparing the computed near-field results with known solutions. Specifically, the scattered field generated by simulating the interaction of a plane wave with a single sphere was calculated using MSTM and compared with the semi-analytic fields derived from Mie theory.

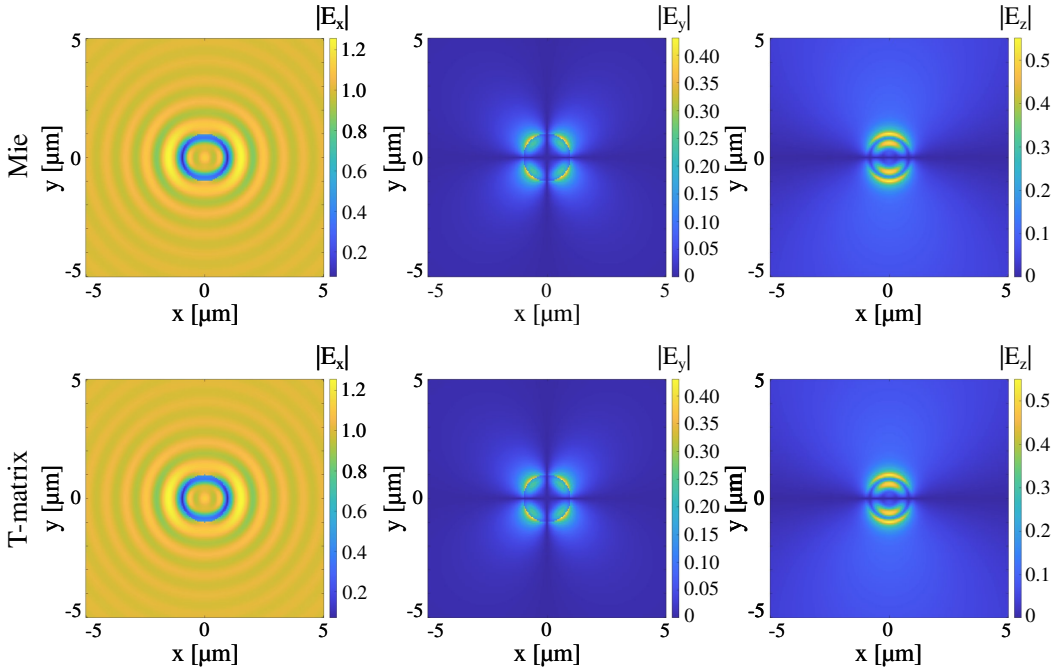

Figure 3.9: Validation of T-matrix simulation (MSTM) against analytic Mie theory (custom code). A single 1 μm sphere with a refractive index of 2 is illuminated by a normally incident plane wave propagating along the z-axis. The background refractive index is 1.33. Each column shows the magnitude of a different electric field component ($|E_x|, |E_y|, |E_z|$) in the xy-plane bisecting the sphere's centre. Top row: Mie theory solutions. Bottom row: MSTM simulation results.

Figure 3.9 shows one such validation example. A single 1 μm sphere with a refractive index of 2 was placed in the simulation domain, and a linearly polarised plane wave ($\lambda = 633$ nm) was incident upon it. The magnitudes of each electric field component ($|E_x|, |E_y|, |E_z|$) were calculated on a transverse xy-plane bisecting the particle using both MSTM and Mie theory. The near fields generated by Mie theory were created using a custom in-house code created by Peter Munro [168]. These

results were, in turn, validated against Kuan Fang Ren's Absphere [169], and the results were found to match (not shown).

As expected, all three field components show excellent agreement between Mie theory and MSTM. Qualitatively speaking, the percentage root mean square error (RMSE) was $< 0.01\%$. The scattered fields were expected to agree. After all, the T-matrix method is an extension of Mie theory to multisphere domains (with the potential to model nonspherical particles, which is not considered in this thesis).

The first objective of validation using Mie theory was to build individual familiarity with a given T-matrix code. E.g. are spheres being placed in the correct locations? Is the near field being evaluated at the right plane? Are the electric field magnitudes being calculated correctly?

The second objective is to validate the specific T-matrix code. As mentioned before, T-matrix implementations are, in general, less mature than other computational methods. The full parameter space of any given solver has not been fully explored, leading to errors and artefacts.

3.4.2 Field comparison vs FDTD

Although established T-matrix software like CELES and MSTM was used, validation of any derived calculations was needed to ensure correct implementation and build confidence in later models of WFS, which are reliant on simulating light propagation accurately. Additionally, these T-matrix codes are more commonly applied to determine far-field scattering distributions in the fields of atmospheric and astrophysics, and as such, near-field calculations have never been validated as extensively.

To validate the near-field calculations, the fields transmitted through a discrete particle medium were directly compared to those calculated using a previously validated FDTD method [170]. A diagram of the simulation is shown in Figure 3.10a.

A plane wave (633 nm) is simulated normally incident onto a 10 μm^3 discrete particle medium containing 35 spheres (see Figure 3.10b). The constituent spheres had a radius 1 μm, a refractive index 1.46, and the background refractive index was 1.33. This medium was turbid enough to ensure multiple scattering of the incident light field.

These specific simulation parameters were chosen to make the FDTD simulation tractable. As shown in Figure 3.10b, the spheres are packed densely into the bounding volume, minimising free space between each sphere. Consequently, less volume needs to be meshed, reducing the overall FDTD simulation size. Moreover, optically soft spheres were chosen that minimise the error caused by staircasing in the specific FDTD implementation used [170].

Having defined the simulation scenario, T-matrix calculations were used to obtain the electric field in an axial plane bisecting the medium. These calculations were performed using MSTM. The resulting field magnitude was plotted in Figure 3.10c. As expected, a seemingly random structure is present due to the scattering by the spheres.

For comparison, the calculation was repeated using FDTD. This involved discretising the entire medium (including the space between the spheres) into a 3D grid of voxels. When designing the grid, a nonuniform spacing previously found to minimise discretisation errors was used [171], along with a perfectly matched layer to minimise boundary reflections [120]. The resulting field magnitude was plotted in Figure 3.10d.

The field obtained by FDTD was visually identical to the one produced by the T-matrix, with the percentage RMSE being $< 2\%$. As the FDTD method is known to be valid, the close similarity between the fields suggested that the T-matrix calculations were accurate. It also validates the implementation and use of the T-matrix

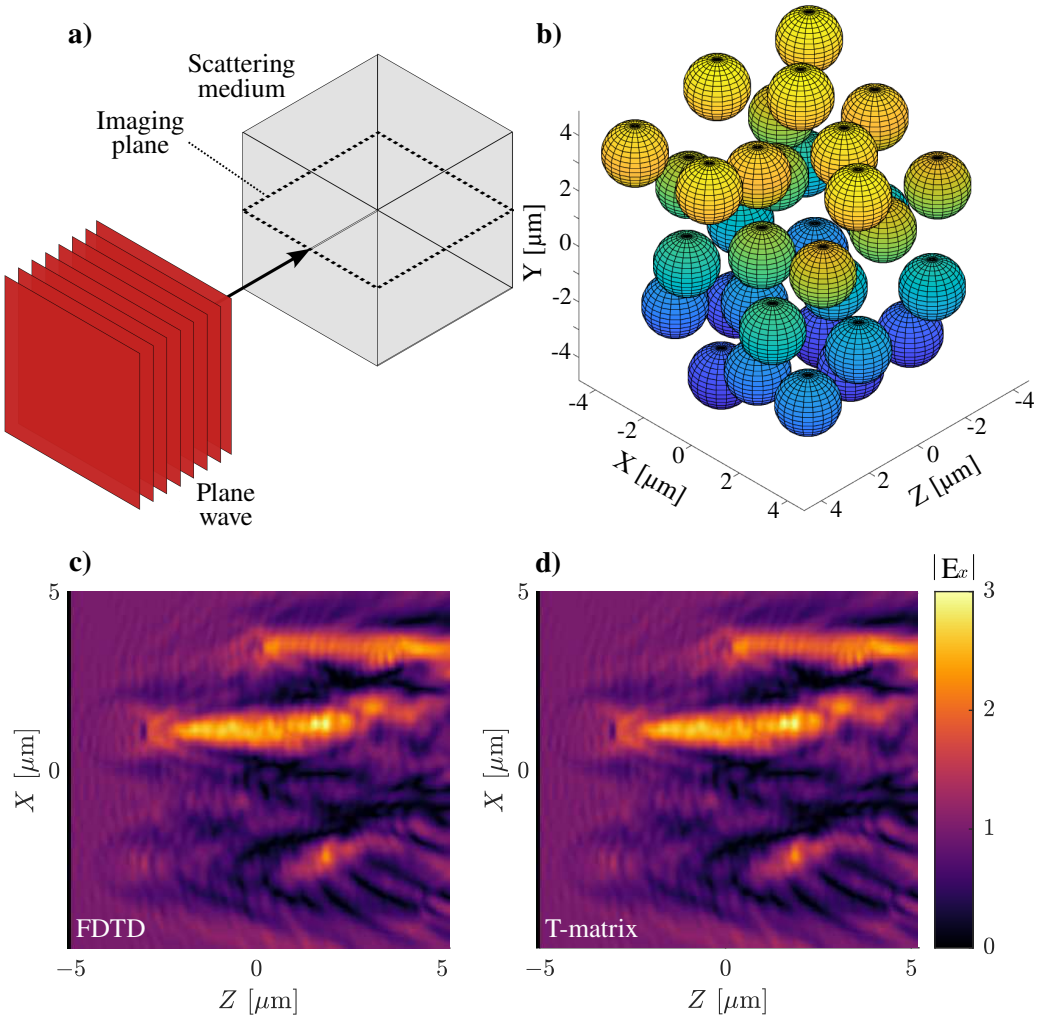

Figure 3.10: Simulated validation experiment comparing fields calculated using the T-matrix (MSTM) and FDTD. a) Setup: a plane wave was incident upon a 10 µm wide cubic medium comprising 35 spheres (radius 1 µm, refractive index 1.46, background index 1.33). b. 3D sphere arrangement. c-d. electric field magnitude in the plane labelled "imaging plane", calculated by (c) the T-matrix and (d) FDTD. The optical wavelength was 633 nm.

codes for this PhD. For example, are the spheres in the correct position and the correct radius? Are the calculations of the electric field amplitude correct?

However, when the simulation was repeated using CELES, artefacts appeared in the field patterns. Low magnitude circular patterns are present at the sphere boundaries, as shown in Figure 3.11.

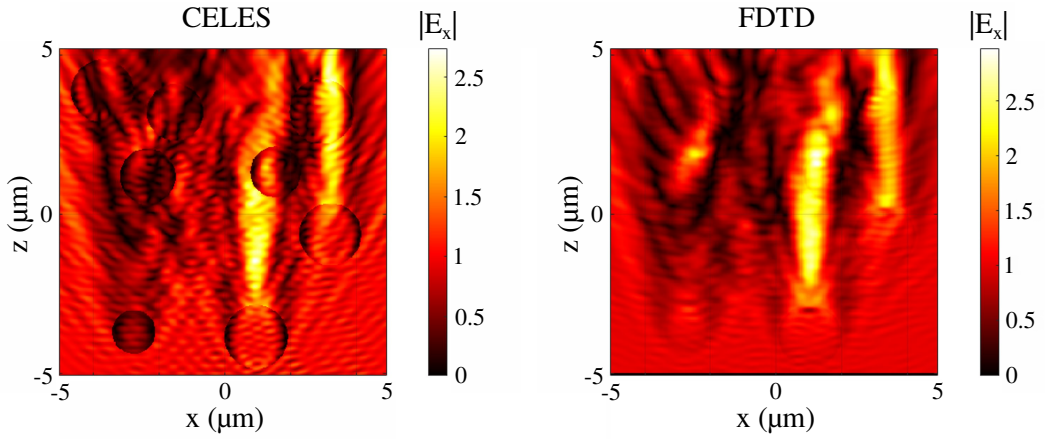

Figure 3.11: Repeated validation experiments (Figure 3.10) using CELES for T-matrix calculations. Low-intensity circular artefacts appear at the sphere boundaries.

This error has been identified implicitly in existing CELES literature. Near-field plots in the original CELES paper have a thick white outline delineating sphere boundaries, or overlay 3D sphere volumes onto the underlying field [129].

It was discovered that the cause of these anomalous field patterns is a CELES-specific block-diagonal preconditioner step, which is designed to improve convergence of the iterative solver. The mechanics and function of this preconditioner are described in detail in the original CELES publication [129]. In brief, the preconditioner works by isolating small blocks containing fewer particles and inverting these blocks analytically. Doing so accelerates the convergence of the GMRES solver, especially in dense or large particle systems. However, because this approximation assumes weak inter-particle coupling during preconditioning, it can introduce small numerical inconsistencies in the computed near field, particularly in highly ordered or tightly packed domains. Disabling the preconditioner or using alternative solver settings mitigated the observed artefacts. However, this significantly increased computational time to impractical levels. As a result, the preconditioner was retained for some simulations, with the understanding that the local fields in the immediate vicinity of the spheres may be inaccurate, although the global field structure remained valid.

3.5 Chapter summary

This chapter established the first component of the computational framework: the ability to model coherent light propagation through scattering media using the T-matrix method. The method was chosen because it provides a rigorous, full-wave solution of Maxwell's equations, while remaining computationally tractable for ensembles of spherical scatterers at length scales relevant to WFS experiments.

The chapter began with a background review of the T-matrix formalism, tracing its origins and summarising the eventual extension of the method to multi-particle systems. The theory was formalised for the case of clusters of spheres. The scaling of the method with respect to particle size and number was explained, as was the truncation order.

A comparative survey of existing solvers (MSTM, CELES, faSTMM) was presented, and their parallelisation strategies (MPI, OpenMP, CUDA) were discussed in the context of the available computational hardware. All three solvers required modification. In particular, MSTM was extended with OpenMP near-field routines to reduce memory usage and a scaling fix was implemented to correct a background-index artefact. CELES was modified to allow 3D near-field evaluation and caching of scattered field coefficients, while faSTMM was extended with the ability to calculate near-fields. These adaptations significantly improved the practicality and functionality of the solvers.

Initial simulations demonstrated that the T-matrix method can generate fully developed speckle patterns in turbid sphere media, with intensity statistics consistent with theory. The computational scaling of MSTM was characterised. Validation against analytic Mie solutions confirmed that single-sphere fields were reproduced to within machine precision, while comparisons with an independent FDTD solver showed agreement for multi-sphere domains. These validations confirmed the correctness of the modified T-matrix framework and built confidence in its use for the

subsequent modelling of WFS.

In conclusion, this chapter delivers a validated, extensible T-matrix framework for simulating coherent light propagation through discrete particle media. The contribution lies in adapting and extending existing solvers to enable accurate near-field calculations, correcting previously undocumented artefacts, and demonstrating that the framework produces statistically correct speckle patterns consistent with theory and independent benchmarks. This framework forms the foundation for the subsequent chapters, where it will ultimately be applied to model WFS.

Chapter 4

Designing T-matrix-optimised sphere-based replica turbid media

This chapter addresses the second component of the computational framework: representing a scattering medium for coupling with the T-matrix method to enable simulations of light propagation through bespoke scattering media. This involves constructing a recipe-based approach to design synthetic simulation media that meets the modelling requirements defined in Section 2.3.4. Specifically, this medium must have desired macroscale optical properties, must model scattering as a result of microscale refractive index inhomogeneities, and must be geometrically unconfined.

The discrete particle model, introduced in Section 2.3.3.5, meets these requirements. The discrete particle model represents scattering media as a pseudorandom aggregation of scattering spheres. The size, density, and refractive index ratio of these spheres define the macroscale optical properties of the medium.

The scope and contributions of this chapter are threefold. Firstly, the mapping from particle-specific design parameters to macroscale optical properties is formalised and investigated in the context of T-matrix simulation, and a method for designing discrete particle media with bespoke optical properties is created. Secondly, a method for optimising the design of the discrete particle media is presented,

both with respect to the medium geometry and the design of the constituent spheres. Finally, the designed media is extensively validated against IAD, Monte Carlo, and memory effects - a framework that can be translated to validating other scattering media.

The chapter proceeds as follows. First, the background theory of the discrete particle method is discussed, including a discussion of modelling generic biological tissue, a formalisation of Mie theory and a review of existing applications of discrete particle phantoms in experimental literature. Second, the methodology used in this thesis to design discrete particle domains is constructed. Next, sample domains are validated using a combination of IAD, Monte Carlo, and memory effects. Two new methods for optimising the design of this discrete particle media are constructed. Finally, the chapter concludes with a summary and a discussion of future work.

4.1 Background

4.1.1 Modelling generic tissue optical properties

As discussed in Section 2.1, light attenuation in biological tissue is governed by both absorption and scattering. Attenuation is described by the attenuation coefficient $\mu_t = \mu_a + \mu_s$, representing the combined probability per unit length that a photon will be either absorbed or scattered.

The scattering and/or absorption behaviour of various biological tissues has been quantified [172, 173, 174, 175], albeit with significant challenges. Measurements are frequently performed *ex vivo*, where the absence of blood flow, structural integrity, and temperature regulation may result in optical properties that differ from *in vivo* conditions. Additionally, reported values are highly dependent on wavelength and experimental methodology, with inconsistencies arising from variations in measurement techniques, sample preparation, and model fitting procedures.

To address this, Jacques [21] proposed a semi-empirical framework that decom-

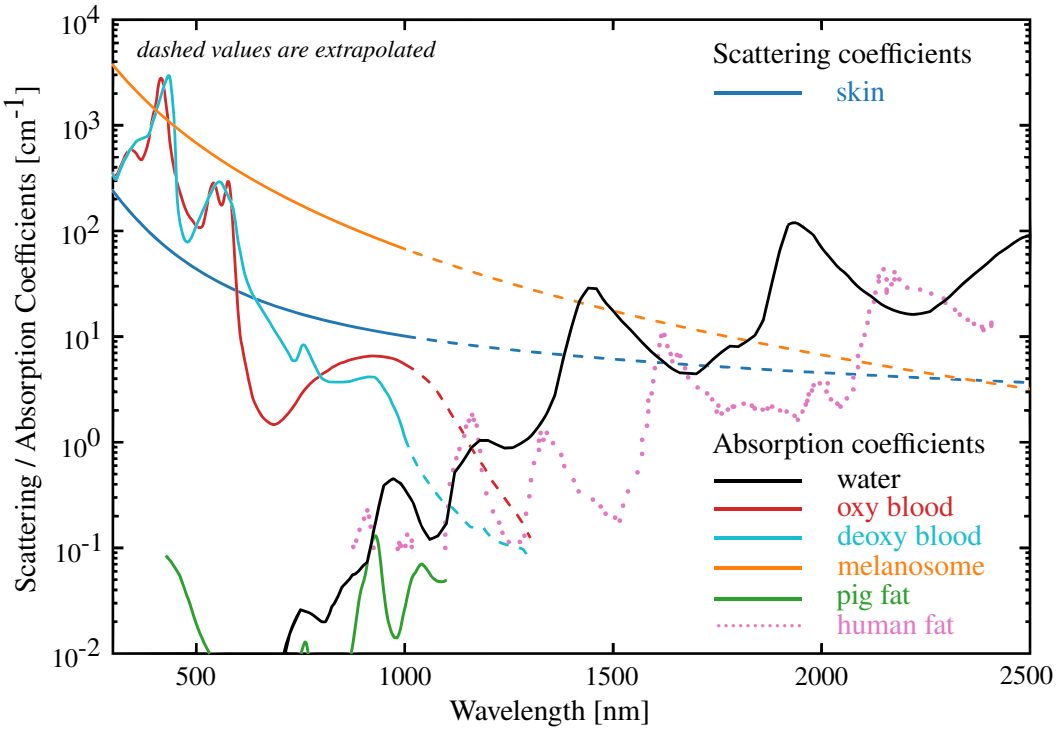

Figure 4.1: Wavelength-dependent optical properties of select constituents of biological tissue. Adapted from Jacques [176]. Data compiled from various sources as described by Jacques [176].

poses both the absorption and scattering behaviour of tissue into the absorption and scattering behaviour of said tissue's key biological constituents. The optical properties of select tissue constituents are shown in Figure 4.1. This approach provides a physically grounded method for estimating bulk tissue optical properties if the composition and structure are known *a priori*, enabling the construction of *"generic"* models for a range of tissue classes (e.g., muscle, fat, skin) across a range of wavelengths.

4.1.1.1 Absorption in a generic tissue

The total absorption coefficient μ_a of a tissue is given as the weighted sum of the absorption spectra of its chromophores:

$$\mu_a = BS\mu_{a.\text{oxyHGb}} + B(1-S)\mu_{a.\text{deoxyHGb}} + W\mu_{a.\text{water}} + M\mu_{a.\text{melanosome}} + F\mu_{a.\text{fat}} + \ldots \tag{4.1}$$

Where [176]:

- B = blood volume fraction
- $\mu_{a.\text{oxyHGb}}$ = oxygenated blood absorption coefficient
- S = oxygen saturation of haemoglobin
- $\mu_{a.\text{deoxyHGb}}$ = deoxygenated blood absorption coefficient
- W = water volume fraction
- $\mu_{a.\text{water}}$ = water absorption coefficient
- M = melanosome volumue fraction
- $\mu_{a.\text{melanosome}}$ = melanosome absorption coefficient
- F = fat volumue fraction
- $\mu_{a.\text{fat}}$ = fat absorption coefficient

4.1.1.2 Scattering in a generic tissue

For scattering, Jacques adopted a two-component model to capture the contributions of subcellular structures to the reduced scattering coefficient μ_s' [21]:

$$\mu_s' = \mu_{s.500nm}' \left(f \left(\frac{\lambda}{500\,\text{nm}} \right)^{-4} + (1-f) \left(\frac{\lambda}{500\,\text{nm}} \right)^{-b_{\text{mie}}} \right) \tag{4.2}$$

Where:

- $\mu_{s.500nm}'$ = reduced scattering coefficient at 500 nm [cm^{-1}]
- f = fraction of scattering at 500 nm due to Rayleigh scattering
- $1-f$ = fraction of scattering at 500 nm due to Mie scattering
- b_{mie} = scattering power for Mie scattering

According to the theory, scattering can be decomposed into two regimes:

- Rayleigh-like scattering from small subcellular structures (organelles, protein aggregates).
- Mie-like scattering from larger structures (nuclei, collagen fibres).

The individual contributions of Rayleigh and Mie scattering towards the bulk reduced scattering coefficient are shown in Figure 4.2.

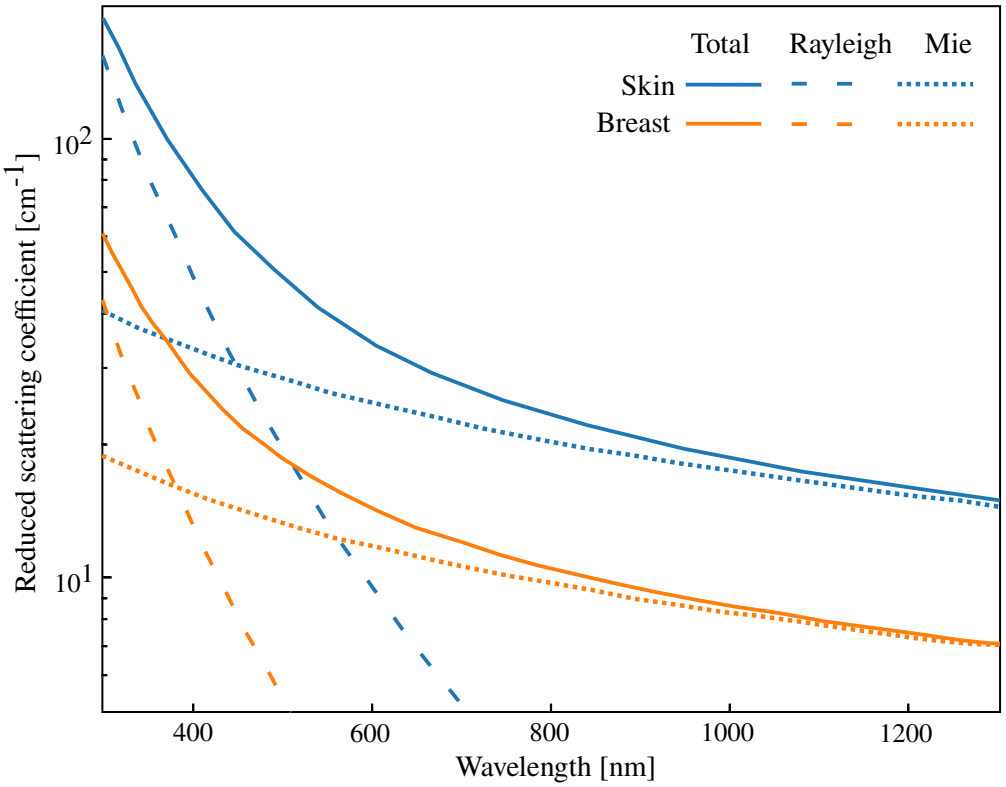

Figure 4.2: Wavelength dependence of the reduced scattering coefficient in biological tissues, decomposed into Rayleigh and Mie contributions. The total scattering (solid line) is shown for representative skin and breast tissue models, with Rayleigh and Mie scattering components overlaid. Rayleigh scattering dominates at shorter wavelengths, while Mie scattering contributes more broadly across the visible and near-infrared range. Adapted from Jacques [21].

As shown in Figure 4.2, the dominant scattering mechanism in tissue for the visible and NIR range is Mie scattering, arising from structures whose sizes are comparable to the wavelength of incident light. Cell nuclei (∼5–10 µm), mitochondria (∼0.5–1 µm), and collagen fibrils (∼30–300 nm) all contribute significantly in this regime.

As such, Mie theory can be directly used to calculate tissue optical properties based on known particle size distributions and refractive indices [20, 115].

In contrast to the reduced scattering coefficient μ_s' and absorption coefficient μ_a, measurement of the scattering coefficient μ_s and anisotropy factor g is more challenging. Jacques discusses several methods for estimating these parameters, but provides no empirical formula for direct quantification [21].

The scattering coefficient is typically measured using collimated transmission experiments, where unscattered light is detected after propagating through a thin tissue sample of known thickness. However, such measurements require samples approximately one mean free path thick ($\sim$100 μm), which are difficult to prepare and prone to dehydration.

The anisotropy factor is most directly measured using angular-resolved goniometry. These measurements involve assessing the scattering phase function, but are complicated by low signal levels in the backwards direction (biological tissue is strongly forward scattering) and by refraction effects at tissue interfaces. An alternate method involves deriving the anisotropy from measurements of μ_s and μ_s'.

For anisotropy, experimental data consistently indicate high values, typically $g > 0.9$. This means tissue can be considered highly forward scattering at these wavelengths. This result is consistent with the observation that Mie scattering dominates in this regime (see Figure 4.2), as Mie scattering has a much greater forward bias compared to Rayleigh scattering [112].

4.1.2 The theory of Mie theory

Designing a synthetic scattering medium to replicate the light scattering behaviour of arbitrary media, including biological tissue, requires understanding how aggregate light scattering through a medium is characterised. As discussed in Section 2.1 and above, key optical properties include the scattering coefficient, absorption

coefficient, and the anisotropy factor, which together determine how light is attenuated and directionally redistributed in the medium. By tuning these parameters, a phantom medium can be designed to mimic the propagation of light in a target tissue.

As shown in Section 4.1.1.2, the aggregate scattering behaviour of biological tissue can be modelled using Jacques' two-component model [21]. This model decomposes the reduced scattering coefficient into two components based on the sizes of the scattering particles: a Rayleigh component and a Mie component (see Equation 4.2). Figure 4.2 shows that for visible and NIR wavelengths, the Mie scattering contribution is dominant. Consequently, the macroscale scattering behaviour of a biological tissue can be modelled using an agglomeration of Mie scatterers.

This theory forms the basis of the discrete particle method - a technique used to model bespoke scattering media as an assembly of spheres embedded in a background medium. The discrete particle model captures the microscale origin of scattering, with macroscale scattering behaviour being the result of multiple microscale refractive inhomogeneities. Microscale geometric and optical properties such as the sphere radius, spatial density and refractive index contrast define the macroscale scattering of light through the medium.

As mentioned in Section 2.3.3.5, one of the primary advantages of the discrete particle model over the continuum model (Section 2.3.3.4) is the ability to model the optical properties of the medium (namely the scattering coefficient and anisotropy) analytically using Mie theory. The process of doing so is described below.

In Mie theory, a fundamental quantity governing light-particle interactions is the scattering cross-section C_{sca}, defined for a single spherical scatterer of radius a, embedded in a non-absorbing background of refractive index n_b, and illuminated

by a plane wave of wavelength λ. The size parameter is given by:

$$x = \frac{2\pi n_b a}{\lambda}. \tag{4.3}$$

Using Mie theory, the total scattering cross-section is expressed as:

$$C_{\text{sca}} = \frac{2\pi}{k^2} \sum_{n=1}^{\infty} (2n+1) \left(|a_n|^2 + |b_n|^2 \right), \tag{4.4}$$

where $k = \frac{2\pi n_b}{\lambda}$ is the wave number in the background medium, and a_n, b_n are the Mie scattering coefficients defined by:

$$\begin{aligned} a_n &= \frac{m\psi_n(mx)\psi_n'(x) - \psi_n(x)\psi_n'(mx)}{m\psi_n(mx)\xi_n'(x) - \xi_n(x)\psi_n'(mx)}, \\ b_n &= \frac{\psi_n(mx)\psi_n'(x) - m\psi_n(x)\psi_n'(mx)}{\psi_n(mx)\xi_n'(x) - m\xi_n(x)\psi_n'(mx)}. \end{aligned} \tag{4.5}$$

with $m = n_p/n_b$ the refractive index ratio, and ψ_n, ξ_n the Riccati–Bessel and Riccati–Hankel functions, respectively (see *Light Scattering by Small Particles* by van de Hulst for a complete derivation [112]).

For a dilute suspension of such particles at number density ρ, the macroscopic scattering coefficient is given by:

$$\mu_s = \rho C_{\text{sca}}. \tag{4.6}$$

In terms of the volume fraction ϕ, the number density is:

$$\rho = \frac{3\phi}{4\pi a^3}, \tag{4.7}$$

so that

$$\mu_s = \left(\frac{3\phi}{4\pi a^3} \right) C_{\text{sca}}. \tag{4.8}$$

Beyond total scattering strength, the directionality of scattering is characterised by the anisotropy factor g, which quantifies the mean cosine of the scattering angle

θ (see Section 2.1.1). It is computed from the differential scattering cross-section $\frac{dC_{\text{sca}}}{d\Omega}$, given in Mie theory as:

$$\frac{dC_{\text{sca}}}{d\Omega} = \frac{1}{k^2}\left(|S_1(\theta)|^2 + |S_2(\theta)|^2\right), \tag{4.9}$$

Where $S_1(\theta)$, $S_2(\theta)$ are the scattering amplitude functions for orthogonal polarisation components. These are computed via:

$$S_1(\theta) = \sum_{n=1}^{\infty} \frac{2n+1}{n(n+1)}\left(a_n \pi_n(\cos\theta) + b_n \tau_n(\cos\theta)\right), \tag{4.10}$$

$$S_2(\theta) = \sum_{n=1}^{\infty} \frac{2n+1}{n(n+1)}\left(a_n \tau_n(\cos\theta) + b_n \pi_n(\cos\theta)\right), \tag{4.11}$$

with angular functions:

$$\pi_n(\cos\theta) = \frac{P_n^1(\cos\theta)}{\sin\theta}, \quad \tau_n(\cos\theta) = \frac{d}{d\theta}P_n^1(\cos\theta), \tag{4.12}$$

where P_n^1 are the associated Legendre polynomials.

The anisotropy factor is then obtained via:

$$g = \frac{1}{C_{\text{sca}}}\int_0^{\pi} \frac{dC_{\text{sca}}}{d\Omega}\cos\theta \sin\theta \, d\theta. \tag{4.13}$$

In practice, the integral in Equation 4.13 is evaluated numerically over a discretised angular mesh.

Online calculators exist to make the calculation of μ_s from Equation 4.8 and g from Equation 4.13 simple, such as the one provided on *omlc.org* by Scott Prahl [177]. Alternatively, a range of dedicated offline codes can be used for T-matrix calculations [178, 169, 168].

4.1.3 Mie theory and discrete particles in phantom design

The concept of using discrete particles has been widely used to design and investigate tissue-mimicking phantoms – artificial materials that replicate the optical scattering properties of biological tissues. Early work by Schmitt and Kumar demonstrated the power of a sphere-based approach to model *"tissue-like"* scattering [115]. They assumed tissue could be modelled as a collection of spherical scatterers with a broad (skewed log-normal) size distribution representative of the microstructure of *in vivo* tissue. Mie theory was then used to calculate the synthetic tissue's bulk optical properties, with their calculated optical properties matching those of real tissue. The initial implication of this research was the idea that critical bulk optical properties, such as scattering coefficient and anisotropy, could be replicated using discrete particle domains with an appropriate distribution of sphere sizes. Their use of a radius distribution for the spheres introduced a wavelength-dependence to the medium - phantom optical properties matched experimentally derived results for a range of wavelengths.

Following this rationale, numerous studies have employed discrete particle methods and Mie theory to guide the fabrication of phantoms that mimic specific tissue types. Pogue and Patterson provide a comprehensive review of these tissue-mimicking phantoms [179]. Briefly, phantoms can be broken down into three components: a matrix, scattering inclusions, and absorbing inclusions. Matrices are a bulk material that is used to support the scattering and absorbing inclusions. It is typically water-based and has a refractive index of around 1.34 [179]. Options include a hydrogel (e.g. made from gelatin or agar), a resin, or a simple aqueous suspension. Scattering inclusions are small particles dispersed throughout the matrix and are responsible for replicating the bulk scattering behaviour of tissue. They typically make up $< 5\%$ of the volume of the phantom and include lipid microparticles, polymer microparticles, and metal oxide powders (such as titanium dioxide or aluminium oxide) [179]. Conversely, absorbing inclusions are chromophores that replicate the optical absorption qualities of the medium, and include ink, dyes, and blood [179].

4.1.4 Optical property measurement with Inverse Adding Doubling

To validate that a designed phantom possesses the target optical properties, the bulk optical properties are measured and compared against Mie theory predictions. A common technique for doing this is the IAD method. The IAD algorithm is an inverse radiative transfer approach that uses measured reflectance and transmittance data (often obtained experimentally with an integrating sphere setup) to infer the sample's μ_s, μ_a, and g.

In practice, three measurements are taken of the scattering sample [180]:

1. *the reflectance, M_R* - which is a measure of the amount of light reflected by a scattering medium normalised by the incident light.

2. *the transmittance, M_T* - which is a measure of the amount of light that passes through a scattering medium normalised by the light that would have passed had the medium not existed.

3. *the unscattered transmittance, M_U* - which is a measure of the amount of light that passes through a scattering medium without being scattered, normalised by the light that would have passed without the medium.

The IAD program then iteratively adjusts guessed values of μ_s, μ_a, and g in a radiative transport model (using adding-doubling) until the calculated values match the measurements [181].

In the context of Mie-based phantoms, IAD serves as a crucial validation step. Because it is possible to predict μ_s and g from Mie theory, those predictions can be compared against the properties retrieved by IAD from experimental data. Cook *et al.* and Grohl *et al.* have used IAD to measure the scattering and absorption properties of tissue-mimicking phantoms for PAI [182, 183]. Troy and Thennadil use IAD to measure the optical properties of human skin in the NIR wavelength range [184].

Overall, the combination of Mie theory for *a priori* design and the IAD method for a *posteriori* optical property validation is a well-established approach in tissue phantom development. This background provides the theoretical basis for designing sphere-based replica media for use with the T-matrix method.

4.1.5 Macroscale validation techniques

The purpose of IAD validation is to ensure that a given synthetic scattering medium has been designed and constructed appropriately - that it can replicate the optical properties predicted by Mie theory.

Ultimately, the critical question is: Is light propagating through the medium as expected? In this sense, the Mie theory and FDTD method from Chapter 3 were used to validate the microscale implementation of the framework. Are spheres being placed appropriately? Are the field calculations accurate? Are there bugs in the T-matrix codes? Meanwhile, IAD will be used to validate the mesoscale elements of light propagation. Does the statistical description of light propagation through a given medium (as defined by the scattering coefficient and anisotropy) match theory?

The final two validation methods extend this approach further, probing the macroscale consequences of light transport. Monte Carlo simulations provide an ensemble-averaged solution to the radiative transport equation, describing how light propagates when interference is averaged out. Comparison between Monte Carlo fluence distributions and ensemble-averaged T-matrix fields therefore tests whether the emergent behaviour of the medium reproduces the expected macroscopic light transport. The agreement between the two validates not only the domain design but also the statistical behaviour of light propagation across many instances.

On the other hand, memory-effect correlations focus on secondary features of scattered light fields that arise from the deterministic nature of light scattering and

interference. The angular memory effect, for example, captures how transmitted speckle patterns decorrelate gradually under small changes in incident angle. Demonstrating that simulated media can reproduce these correlations confirms that the framework can model second-order speckle properties that are known from experiment and theory.

Together, Monte Carlo and memory-effect validation ensure that the framework can model the emergent statistical and correlation behaviours of light in complex media. This builds confidence that the framework can be reliable at modelling light focusing via WFS.

4.2 Methods

4.2.1 Defining generic tissue optical properties

4.2.1.1 Absorption coefficient

"Ex vivo" volume fraction measurements for various tissues are provided by Jacques [21]. For example, skin dermis can be described using the following volume fractions [176], with the volume fractions being defined by Equation 4.1:

- $B = 0.002$
- $S = 0.70$
- $W = 0.65$
- $M = 0$
- $F = 0$

Consider a sample of skin dermis being illuminated by either the ubiquitous He-Ne (λ=633nm) or Nd:YAG (λ=1064nm) lasers. Using the volume fractions defined above and the absorption coefficients specified in Figure 4.1 with Equation 4.1 allows Table 4.1 to be constructed:

Tissue constituent	Absorption coefficient [cm^{-1}]		Volume Fraction	Adjusted absorption coefficient [cm^{-1}]	
	633nm	1064nm		633nm	1064nm
Oxygenated blood	2.744	3.502	0.0014	0.0038416	0.0049028
Deoxygenated blood	25.337	0.373	0.0006	0.0152022	0.0002238
Water	0.003	0.120	0.65	0.00195	0.078
Melanosome	309.575	54.919	0	0	0
Fat (Pig)	0.00121	0.142	0	0	0

Table 4.1: Absorption coefficients and volume fraction adjusted values for various constituents of biological tissue at 633 nm and 1064 nm.

Therefore, the absorption coefficient of a generic biological tissue is defined as the sum of the adjusted absorption coefficients at each wavelength of interest. This is calculated to be 2.099×10^{-3} mm^{-1} at 633nm and 8.313×10^{-3} mm^{-1} at 1064nm.

4.2.1.2 Scattering coefficient

"Ex vivo" measurements of the scattering properties of biological tissue have been calculated as [175, 21]:

- $\mu'_{s.500nm} = 20.2$ cm^{-1}
- $f = 0.18$
- $b_{\text{mie}} = 0.638$

Which, according to Equation 4.2, results in a tissue with a reduced scattering coefficient of 15.6 cm^{-1} at 633 nm. With an anisotropy of 0.9 [21], this results in a tissue with a scattering coefficient of 15.6 mm^{-1}.

4.2.1.3 Generic tissue optical properties

Ultimately, for most soft tissues and in the 600–1000 nm *"optical window"*, $\mu_s \gg \mu_a$. For instance, in human dermis at 633 nm, μ_s is many orders of magnitude greater than the scattering coefficient [172, 21].

This is supported by our calculation of μ_a and μ_s at 2.099×10^{-3} mm^{-1} and 15.6 mm^{-1} respectively at 633 nm. As such, absorption is not modelled when designing the computational framework. This simplification of the physics is made

under the assumption that absorption has a negligible impact on the light propagation (at millimetre depths and visible and NIR wavelengths), and is an assumption used by the existing models of WFS discussed in Section 2.3.2.

4.2.2 Generating discrete particle domains

4.2.2.1 Design methodology

A given *"recipe"* for producing sphere suspensions with desired macroscale properties can be obtained by solving a linear problem defined by Mie theory. In practice, because the coefficients depend nonlinearly on the sphere size and refractive index, the solution is found by searching over candidate sphere parameters and selecting those that minimise the mismatch between predicted and target properties.

To identify as many viable designs as possible, an exhaustive parameter search was performed. Matzler's Mie code [178] was used to calculate the scattering coefficient and anisotropy across all domains, with sphere refractive indices ranging from $1.34 \leq n_s \leq 2.6$, volume densities from $0.0001 \leq v_f \leq 0.05$, and radii from $0.05 \leq r \leq 2$ μm. The background refractive index was set equal to water at $n_b = 1.33$, and the wavelength was defined as $\lambda = 633$ nm and $\lambda = 1064$ nm. This simulation took one week on UCL's 'Myriad' cluster. Upon completion, a 12 GB database of ∼25 million discrete particle domains was generated.

Matzler's code was validated (not shown) against the three other codes, Scott Prahl's online OMLC solver [177], Kuan Fang Ren's ABsphere [169], and an in-house Mie code by Peter Munro [168].

The process of selecting an appropriate recipe to produce a medium with a given target scattering coefficient and anisotropy was as follows:

1. Define target bulk properties (μ_s and g, at a wavelength λ. For example, consider the generic biological tissue defined in Section 4.2.1.3, for which $\mu_s = 15.6$ mm^{-1} and $g = 0.9$ at 633 nm.

2. Search through the database of ∼25 million discrete particle domains and identify domains with values of μ_s and g that match the target medium within a given tolerance.

3. Construct a discrete particle domain by pseudorandomly placing N non-overlapping spheres in a bounding volume (using the pseudorandom placement method described in Section 3.3.3).

4. Export sphere centres, radii, and refractive indices to the input format required by the T-matrix solver.

4.2.2.2 Design considerations

There is a hidden step between the second and third processes defined above. In practice, multiple domains can exist with the desired optical properties with different permutations of scattering spheres. These optically identical discrete particle domains are called *"candidate"* domains - domains with the correct target optical properties but a distinct *"recipe"*, e.g. sphere sizes, refractive index contrast or concentration. To select the optimal candidate domain, appropriate evaluation criteria must be selected.

Experimental constraints are useful for removing unviable candidate domains. Common scatterers, such as rutile titanium dioxide particles or silica microbeads, have defined refractive indices and can only be manufactured at specific particle sizes. This simplifies the design of a discrete particle domain, but makes it more difficult to create a given domain with specific target optical properties. This is because not all constituent scatterers are able to generate discrete particle domains with a particular set of target optical properties. For example, rutile titanium dioxide has a refractive index of 2.5836 at $\lambda = 633$ nm and is commonly manufactured with a radius of approximately 1 μm [185]. Therefore, it is only possible to vary the volume concentration of the domain, the background refractive index, or the wavelength of the incident light. To visualise the optical properties of the domains that can be generated with rutile titanium dioxide, Mie theory was used to calculate

the scattering coefficient and anisotropy for a series of titanium dioxide discrete particle instances. The instances had a fixed refractive index of 2.5836, a background refractive index of 1.33 and a radius of 1 μm [185]. The volume fraction was varied from 0.005 to 0.4, and the wavelength from 200 to 1200 nm. Results are plotted in Figure 4.3.

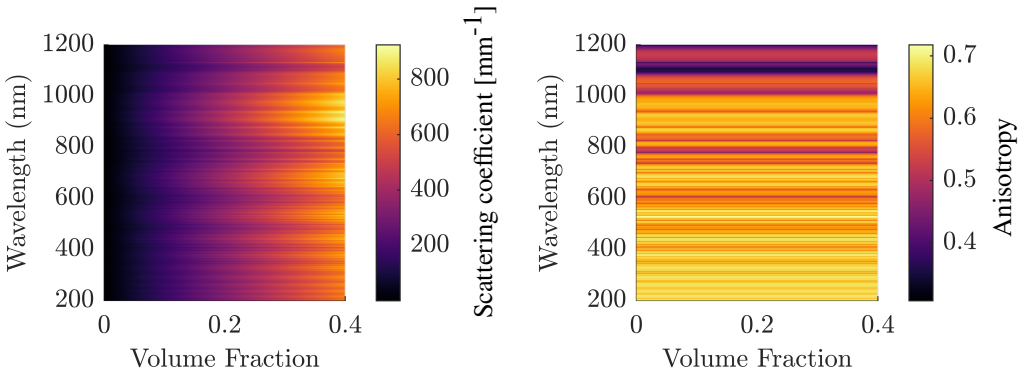

Figure 4.3: Using Mie theory to determine the scattering coefficient (left) and anisotropy (right) of a discrete particle domain comprised of rutile titanium dioxide scatterers with sphere radius of 1 μm and a refractive index = 2.5836 in a background with a refractive index = 1.33. The volume fraction was varied from 0.005 to 0.4 and the wavelength from 200 to 1200 nm.

As shown in Figure 4.3, generating a domain with an anisotropy over 0.7 is difficult using titanium dioxide particles. As such, while titanium dioxide domains can be constructed to replicate the scattering coefficient of biological tissue (by changing the concentration), replicating tissue's highly forward scattering nature is challenging. This is made more challenging as anisotropy is defined on a per-sphere basis, as shown in Figure 4.3. Anisotropy does not change as the volume concentration of the discrete particle domain is increased.

Scattering coefficients are generally easier to match than anisotropies. This is because the scattering coefficient scales linearly with the volume concentration of scatterers, as shown in Figure 4.3. There are some limitations to this, however. Mie theory becomes invalid when the scatterer concentration is too high due to near-field interactions between particles. Moreover, random placement algorithms fail when

packing spheres into domains with a very high concentration, necessitating the use of a packing algorithm such as Lubachevsky–Stillinger or Jodrey–Tory algorithm [186].

In this thesis, a computational framework is constructed for modelling WFS, and as such, the experimental design constraints discussed above do not have to apply. Researchers have significantly more freedom in designing the parameters of a discrete particle domain. Consequently, more viable *"candidate"* exist, and another selection method is required. The process of deciding on the ideal *"candidate"* domain will be discussed in Section 4.4.1.

4.2.3 Measuring, reflectance, transmittance and ballistic light

Values of the reflectance, M_R, and the transmittance, M_T, required by IAD to calculate the optical properties of a medium are experimentally measured using integrating spheres placed before and after the medium [180]. Measuring the unscattered transmittance, M_U, is accomplished by placing a detector at some distance away from the scattering medium, directly in the path of the Gaussian beam. An aperture is used to spatially filter the scattered light, such that only the unscattered light is detected. In this section, a process to replicate the experimental measurement of these IAD inputs *in silico* is formulated.

Measuring M_R and M_T of a scattering medium is relatively simple. The total light intensity on a plane directly in front of and behind the medium can be directly measured using the T-matrix method as a Gaussian beam is simulated propagating through the medium. M_R and M_T can then be normalised by measuring the intensity across the same planes with the scattering medium removed. In practice, this was achieved by using the T-matrix codes (CELES or MSTM) to simulate a medium with a single sphere of the same refractive index as the background. A diagram depicting the measurement of these IAD values is shown in Figure 4.4.

Measuring M_U is more challenging. Three approaches can be used:

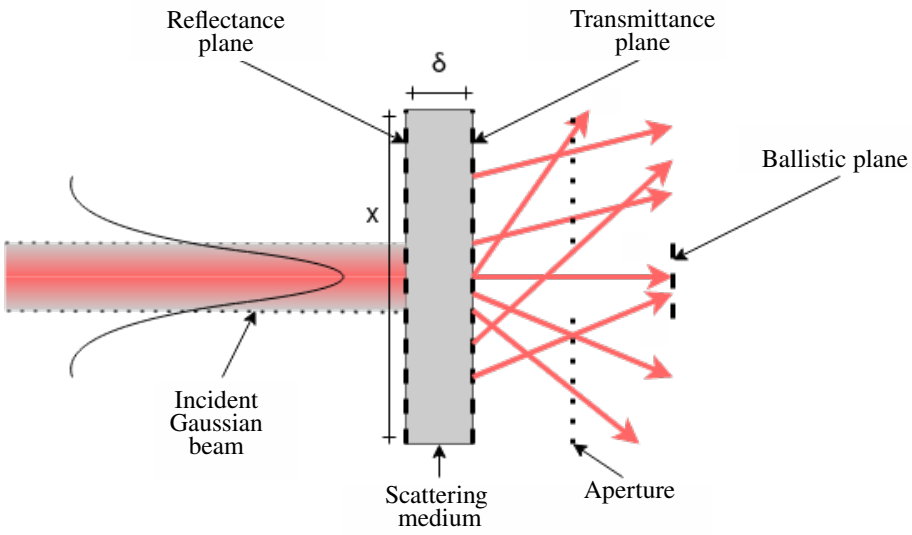

Figure 4.4: In IAD, measurements of the reflectance, transmittance and ballistic light component can be used to calculate the optical properties of a scattering medium. Using the T-Matrix method, the scattering of an incident Gaussian beam is simulated, and the reflectance and transmittance are measured by evaluating the near-field intensity across the two planes shown. To measure ballistic light, the measured intensity is obtained at multiple distances behind the scatterer, simulating the effect of spatial filtering using an aperture.

- Do not measure M_U. Instead, use the expected value of g derived from the Mie theory. The IAD software can use this anisotropy, combined with the measured values of M_R and M_T, to model the scattering coefficient of the scattering medium.

- Do not measure M_U. Instead, use a value of g directly derived from the average cosine of the scattered light around the scattering medium. The T-matrix method can be used to directly calculate the scattering phase function, from which the anisotropy can be derived.

- Measure the ballistic light along a profile behind the medium that runs parallel to the direction of propagation. Average the intensity along this profile to measure the ballistic light.

The effects of each method on the IAD calculation of the optical properties of the medium will be discussed in Section 4.3.2.

Note from Figure 4.4 that any light that escapes from the sides of the medium would not be detected by either the reflectance or transmittance planes. This is an experimental and computational limitation of IAD that can be minimised through the appropriate design of the scattering medium. By minimising the size of the incident Gaussian beam and maximising the diameter of the scattering medium, it is possible to reduce the amount of light escaping from the sides of the medium [180]

For the purposes of validation, two simulation mediums were created for use with IAD. First, a special IAD-specific titanium dioxide medium with geometrical constraints designed to carefully minimise light escaping from the sides of the medium. Specifically, size constraints were imposed on this domain such that the radius must be $\times 2$ the thickness, δ, and the width of the incident Gaussian beam must be less than $1/2$th the domain radius to further minimise light escaping from the sides. Second, a titanium dioxide phantom designed to replicate the seminal Vellekoop and Mosk WFS demonstration [7]. This phantom was designed to be useful for later simulations of WFS, and as such, its validation with IAD would be foundational for demonstrating the computational framework's ability to model WFS. The construction of these two domains will be discussed in Section 4.3.1.

4.3 Validation

4.3.1 Creating titanium dioxide validation phantoms

To validate the method of creating discrete particle domains with target scattering coefficients and anisotropies, appropriate domains must be constructed for validation purposes. As mentioned, two domains have been designed for this role. Firstly, an IAD-specific highly-constrained geometry designed to work well with the limitations of the IAD model. Secondly, a more experimentally viable simulation medium that would be reused for later simulations involving the modelling of WFS.

4.3.1.1 Geometrically constrained phantom

The first discrete particle domain was constructed with spheres that have a diameter of $1\mu m$, a refractive index of 2.6 and a packing density of 0.25%. The background refractive index was 1.33, and the wavelength of the incident light was 633 nm. Mie theory predicts that this recipe would create a scattering medium with a scattering coefficient and anisotropy of $\mu_s = 93.98cm^{-1}$ and $g = 0.4841$, respectively.

The overall medium geometry was constrained to minimise the proportion of light escaping from the sides of the simulation - a common cause of error in IAD [181]. A sphere count of 10000 spheres was first defined to ensure multiple scattering and minimise the scattering impact of any given sphere. Then a geometrical constraint was applied to a bounding cylinder containing these 10000 spheres: the radius of the cylinder must be $\times 2$ the thickness. This constraint was plotted on Figure 4.5, and the intersecting lines were used to determine the optimal domain size. This size was determined to be "hockey puck" shaped geometry with a radius of 69.3361 µm and a depth of 34.6681 µm. This domain can be seen in Figure 4.5.

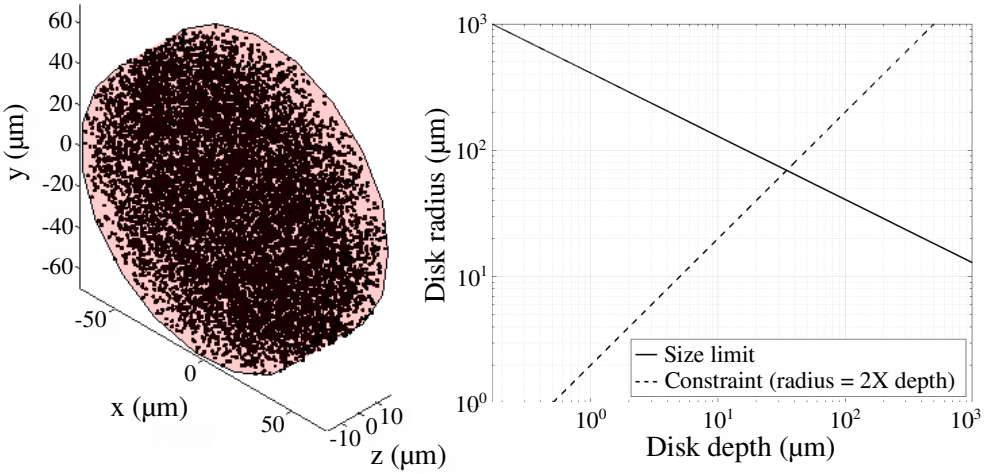

Figure 4.5: Left) The titanium dioxide discrete particle medium optimised for IAD simulation. 10000 spheres are constrained by a disk of radius 69.3361 µm and depth 34.6681 µm. Sphere density is 0.25%. This geometry was designed to minimise the proportion of light that escapes from the sides of the simulation. Right) Determining the optimum radius and depth for the IAD validation medium. A constraint is applied such that the radius must be double the depth of the bounding cylinder, leading to a "hockey puck" geometry.

4.3.1.2 Vellekoop and Mosk phantom

As the purpose of this thesis is to construct a computational framework for modelling light propagation and simulating WFS, a discrete particle validation domain was designed that emulates the titanium dioxide phantoms used in seminal WFS experiments. Specifically, the domain was designed to replicate the 10 μm thick white paint layer used by Vellekoop and Mosk in their original demonstration of optical focusing through turbid media [7]. Moreover, titanium dioxide scattering inclusions are a common component of experimental tissue-mimicking phantoms, as discussed in Section 4.1.3.

The target optical properties were selected based on the TMFP provided in their paper [7], which is approximately 5 μm. Specific scattering coefficient and anisotropy values were not provided. Instead, Mie theory was used to determine these values using a modified version of the method described in Section 4.2.2. Rather than designing a domain to fit a specific scattering coefficient and anisotropy, a target TMFP was defined (which is a function of scattering coefficient and anisotropy as defined in Section 2.1.1). It was discovered that a domain with a TMPF of $\sim$5 μm could be generated when μ_s=445 mm^{-1} and g=0.55. It was determined from the data in Figure 4.3 that a volume fraction of 0.26 at a wavelength of 633 nm was capable of generating a domain that matched the target scattering coefficient and anisotropy with $< 1\%$ error. The final *"recipe"* for this titanium dioxide domain was:

- Sphere refractive index = 2.5836
- Background refractive index = 1.33
- Sphere radius = 1 μm
- Volume fraction = 0.26
- Wavelength = 0.633 nm

Using the pseudorandom placement method described in Section 3.3.3, a 100x100x10 μm^3 volume was populated with the spheres described above. The central 30x30x10 μm^3 subsection of the resulting discrete particle volume is shown in Figure 4.6 (a magnified view of the domain makes it easier to visualise the individual spheres).

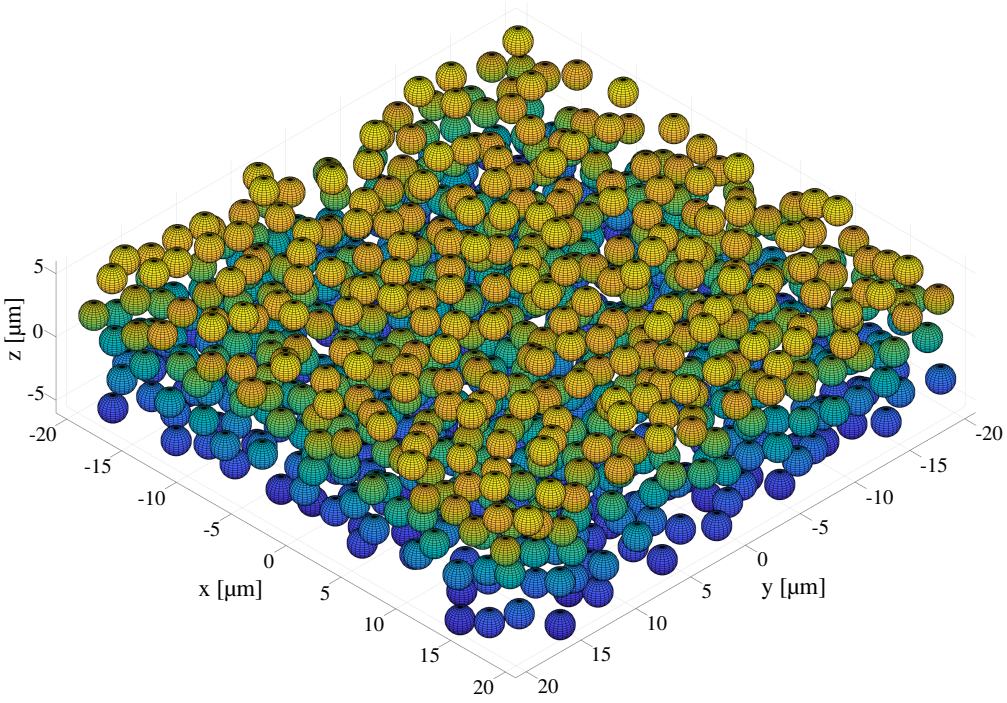

Figure 4.6: Titanium dioxide discrete particle domain designed to replicate the scattering layer used in Vellekoop and Mosk's original demonstration of WFS. A 100x100x10 μm^3 volume is populated with 1 μm at a volume density of 0.26 using the pseudorandom placement method described in Section 4.2.2. Shown here is the inner 30x30x10 μm^3 volume so the spheres can be visualised more clearly.

4.3.2 Inverse adding doubling

A Gaussian beam of $\lambda = 633$ nm was simulated propagating through the geometrically constrained "hockey-puck" domain using MSTM, running on Zeus. As shown in Figure 4.4, the field was evaluated at the transmittance and reflectance planes, as illustrated in Figure 4.7. By normalising these fields against free-space propagation, the diffuse reflectance M_R and diffuse transmittance M_T were determined. In addition, a profile along the optical axis was extracted, from which the ballistic

component M_U was estimated by averaging the on-axis intensity beyond the scattering layer (see Figure 4.7).

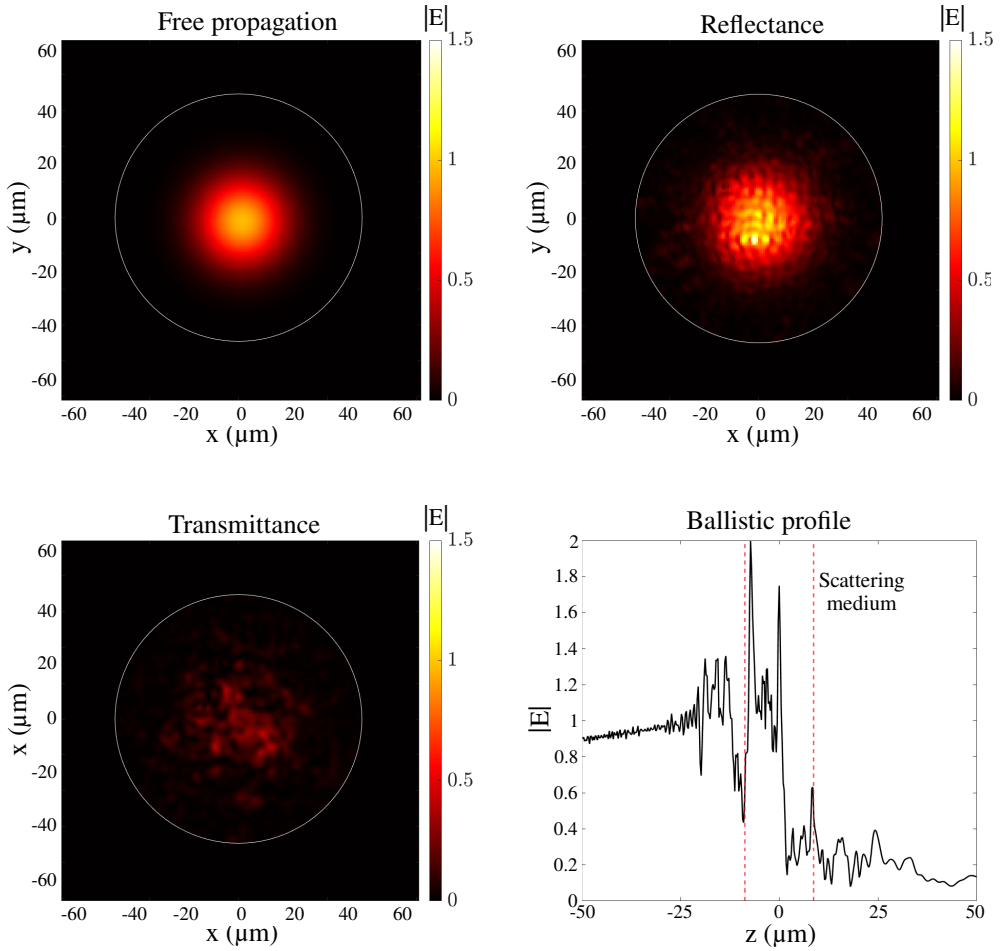

Figure 4.7: The transmittance, reflectance and ballistic profile for a Gaussian beam incident on a scattering medium calculated using the T-matrix method. The simulated discrete particle model is shown in Figure 4.6. By normalising the intensity in the transmittance and reflectance planes by the free propagation measurement, M_T and M_R can be determined. M_U is measured by averaging the intensity along the axis of beam propagation after the scattering medium (represented by the two dashed red lines). The white circles show the boundary of the scattering disk.

As mentioned in Section 4.2.3, three methods have been created for providing a measurement of anisotropy or the ballistic component required by IAD. First, anisotropy can be taken directly from Mie theory, thereby avoiding explicit measurement of M_U. Second, anisotropy can be directly derived from the scattering

phase function. Third, M_U can be measured directly from the transmitted field along the optical axis.

The IAD-derived values of scattering coefficient and anisotropy, for each method, are shown in Table 4.2.

Optical property	Mie Theory	g direct Mie	g phase function	M_U measured
μ_s (cm^{-1})	93.98	90.90 ± 12.12	89.56 ± 4.94	87.11 ± 3.31
g	0.48	0.48	0.44 ± 0.06	0.39 ± 0.04

Table 4.2: IAD derived optical properties for the geometrically optimised validation. g direct Mie refers to using the Mie theory-estimated value of anisotropy as an input. g phase function refers to calculating the anisotropy from the average cosine of the scattering phase function (MSTM has a built-in function to automate this). M_U measured refers to measuring the unscattered ballistic component by averaging along a ballistic profile behind the medium, as shown in 4.4.

Each technique demonstrates close agreement between the optical properties derived from IAD and those predicted by Mie theory. Across all three strategies for estimating the ballistic component or anisotropy, the scattering coefficients fell within a narrow range around the theoretical value of 93.98 cm^{-1}. The smallest deviation was observed when the anisotropy was fixed directly from Mie theory, yielding $\mu_s = 90.9 \pm 12.1$ cm^{-1}. Comparable results were obtained when the anisotropy was computed from the scattering phase function (89.6 ± 4.9 cm^{-1}) and when the ballistic transmission was measured directly from the axial profile (87.1 ± 3.3 cm^{-1}).

The retrieved anisotropy values show a similar pattern. Both the Mie-based input and phase-function calculation reproduced values close to the theoretical estimate of $g = 0.48$. The phase-function method produced a slightly lower mean anisotropy (0.44 ± 0.06), while the ballistic measurement approach gave the lowest value (0.39 ± 0.04). This systematic reduction is consistent with the increased sensitivity of the direct ballistic measurement to multiple scattering, which can cause a modest underestimation of forward scattering strength.

To investigate the Vellekoop and Mosk experimentally relevant titanium dioxide domain, the final approach of measuring M_u directly was used. This is because it most closely matches experimental practice while still being a sufficiently accurate method of validating the optical properties of a given domain.

To this end, the above approach was applied to the titanium dioxide phantom designed to replicate the seminal Vellekoop and Mosk demonstration of WFS. The target properties were $\mu_s = 445$ mm^{-1} and $g = 0.55$ (transport mean free path ~ 5 μm). A $30 \times 30 \times 10$ μm domain was populated with 1 μm spheres at a concentration of 0.26, embedded in water ($n = 1.33$). The simulation geometry is shown in Figure 4.8a.

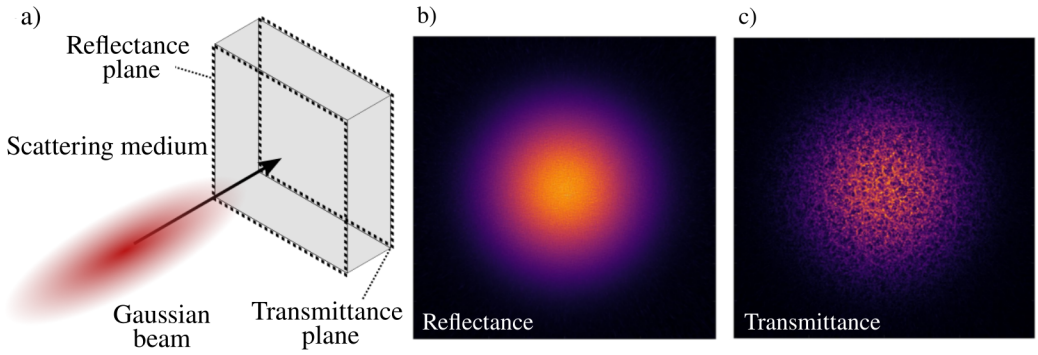

Figure 4.8: Validating the medium design process by simulating material characterisation experiments. a) Setup: a Gaussian beam ($\lambda = 633$ nm) was incident upon a diffusive layer of titanium dioxide spheres (radius 1 μm, refractive index 2.6, concentration 0.26 by volume) embedded in a homogeneous background ($n = 1.33$). b–c) Intensity distributions in the "reflectance" and "transmittance" planes labelled in subfigure a).

Normalised field distributions in the reflectance and transmittance planes are presented in Figure 4.8b and c. As expected, in the reflectance plane, the intensity distribution was smooth and Gaussian-shaped, with only slight perturbations due to backscattering. Across the transmittance plane, the profile is still roughly Gaussian; however, the intensity distribution is more irregular and speckled due to multiple scattering across the thin layer. To calculate the unscattered transmittance, the intensity was integrated along a 10 µm long line along the optical axis behind the layer (not plotted).

IAD was used to estimate the scattering coefficient and anisotropy based on the derived values of M_R, M_U, and M_T. The scattering coefficient was calculated to be 445 mm^{-1} and the anisotropy 0.56. This results in a transport mean free path of 5.1 μm. As these agreed closely with the design parameters, this verified the design process. This demonstrates that IAD provides a robust independent validation of the medium design process.

4.3.3 Monte Carlo

Monte Carlo modelling provides a statistical solution to the radiative transport equation by simulating the trajectories of individual photons as they undergo successive scattering and absorption events. Unlike full-wave methods, it does not resolve interference effects; instead, it yields the ensemble-averaged fluence distribution corresponding to a medium with given optical properties. As mentioned in Section 4.1.5, Monte Carlo can be used as a technique to validate the macroscale nature of light propagation through the medium, independent of any given discrete particle instance.

To this end, a Gaussian beam was first simulated propagating through the experimentally inspired titanium dioxide phantom from Figure 5.3. The Gaussian beam had a full-width at half-maximum width of 10 μm at a wavelength of 633 nm. The magnitude of the electric field was calculated in an axial plane bisecting the layer and plotted in Figure 4.9a.

As expected, when entering the titanium dioxide layer, the Gaussian-shaped beam loses coherence and breaks up. This occurs most prominently halfway through the medium, corresponding to a depth of $\sim$1 TMFP. Beyond the medium, the light forms complex interference patterns with fine spatial structure inside the layer, expanding outward as the light begins to propagate in free space beyond the medium.

Each T-matrix simulation yields the exact field for a single, plausible instance of

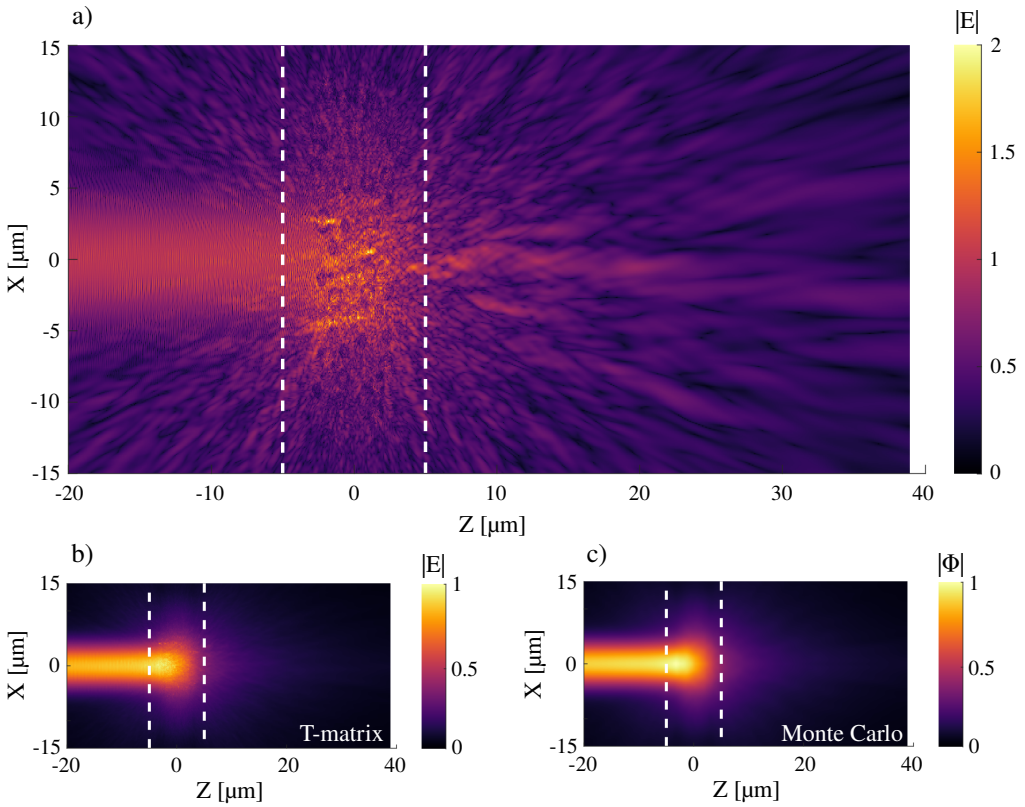

Figure 4.9: Simulation of Gaussian beam propagation through a diffusive titanium dioxide medium. The plots show the spatially-resolved electric field magnitudes ($|E|$) and normalised fluences ($|\Phi|$) in a plane bisecting the layer: (a) calculated using a T-matrix simulation; (b) averaged over 1000 repeats with different sphere arrangements; (c) obtained with Monte Carlo. The incident light was a Gaussian beam (10 µm FWHM, lambda = 633 nm, travelling left-to-right). The boundaries of the layer are shown by the white lines.

the titanium dioxide discrete particle domain. Different pseudorandom placements of spheres using the same recipe generate unique speckle patterns, but each is (in theory) representative of the same mesoscale scattering medium. By repeating the simulation across many such instances, it is possible to average out the diversity of any individual field and construct an ensemble model of light propagation through the medium.

Averaging over 1000 instances produced the distribution shown in Figure 4.9b, where the speckle structure vanishes, leaving a smooth intensity profile. This ensemble-averaged field can be compared with the fluence profile generated by the

Monte Carlo method of simulating light propagation.

To generate a Monte Carlo fluence profile, a titanium dioxide layer of thickness 10 μm was modelled using Monte Carlo (ValoMC [187]). The bulk optical properties used as inputs were those derived from Mie theory for the discrete particle recipe described in Section 4.3.1, namely a scattering coefficient $\mu_s = 445\ \mathrm{mm}^{-1}$, an anisotropy factor $g = 0.55$, and a refractive index-matched background ($n = 1.33$). The absorption coefficient was set to zero, consistent with the medium's weakly absorbing nature.

The Monte Carlo fluence distribution was normalised to the incident fluence and visualised in Figure 4.9c. The profile shows the expected smooth decay of intensity with depth into the medium, broadened laterally by multiple scattering. No speckle structure is present, as the method yields an ensemble-averaged solution to the radiative transport equation. This distribution is visually indistinguishable from the ensemble-averaged T-matrix field shown in Figure 4.9b. Quantitative comparison confirms this agreement, with a normalised RMSE between the two profiles of less than 4%, demonstrating that the T-matrix framework reproduces the same macroscopic light transport behaviour as Monte Carlo modelling.

4.3.4 Memory effects

Using the validation approaches demonstrated so far, it has been possible to demonstrate that the designed discrete particle mediums are able to reproduce bespoke optical properties (IAD) and, when averaged over many instances, model bulk light transport correctly (Monte Carlo). However, a given replica medium should also be capable of modelling the higher-order correlation phenomena observed in experimentally-derived speckle fields. The angular memory effect (AME) - which is the small tilt invariance of the transmitted speckle pattern - provides a method of validation. Demonstrating AME *in silico* confirms that the discrete particle framework preserves subtle speckle correlations arising from deterministic multiple scattering. This is an important feature for the motivation of wanting to model

light focusing via WFS in subsequent chapters.

A tissue-like discrete particle domain was designed using Mie theory to match the properties of biological tissue at $\lambda = 633$ nm. As discussed in Section 4.2.1, a generic tissue has $\mu_s = 15.6$ mm^{-1} and $g = 0.9$. A bounding volume was created that measured $200 \times 200 \times 100$ μm^3 and comprised spheres of radius 1.72 μm and refractive index $n = 1.6$ embedded in a background of $n = 1.33$ at a volume fraction of 0.0077. This recipe was randomly chosen from the available candidate domains able to generate a medium with tissue-like optical properties.

Light propagation through this domain was simulated using CELES [129] on Myriad. Forty-one plane waves with polar angles from 0° to 4° were incident. For each angle, the complex transmitted field was recorded on a 50×50 μm^2 plane behind the medium. This field is shown in Figure 4.10.

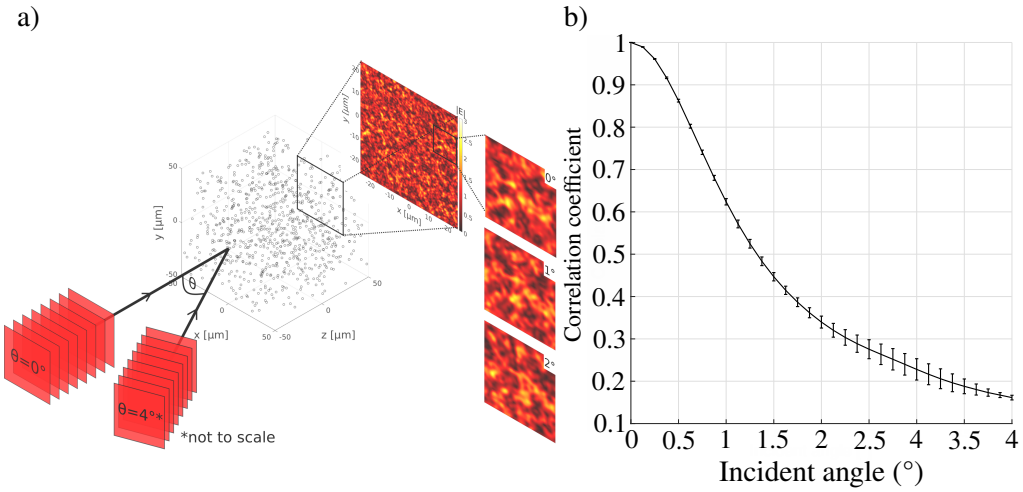

Figure 4.10: a) Diagram of angular memory effect simulations through a tissue-like domain. Light incident on a tissue-like discrete particle domain is scattered, and a speckle pattern is generated on a plane behind the medium. As the incident angle is shifted, the speckle pattern begins to decorrelate. b) The correlation coefficient of each speckle pattern (as determined by the cross-correlation coefficient) is plotted as a function of the angle of the incident light.

As shown in Figure 4.10, a plane wave propagating through the tissue-like domain is scattered and a speckle pattern is generated on a plane behind the medium. When

the angle of the incident light is varied, the speckle pattern begins to gradually decorrelate, which can be visualised in Figure 4.10a by highlighting the decorrelation of a small feature within the large speckle.

To quantify this decorrelation, the cross-correlation coefficient between speckle resulting from a normally incident plane wave, and speckle patterns produced by plane waves incident at varying angles is plotted in Figure 4.10b. Simulations were repeated 5 times with different instances of the tissue-like domain.

The measured correlation curves (Fig. 4.10b) display the characteristic bell-shaped profile of the AME: correlations remain high for small input tilts and decay smoothly with increasing angle. The curves were consistent across the five independent realisations, indicating that the effect is a property of the recipe-defined medium rather than a specific particle arrangement.

These results confirm that the designed tissue-like media reproduce expected angular speckle correlations, thereby validating the framework at the macroscale level. The AME behaviour observed here is qualitatively consistent with theory and prior experiments in highly anisotropic media [97]. Note that existing attempts to simulate angular correlations in scattering media using less rigorous techniques like random phase screens failed to model the correlations accurately [97].

4.4 Optimisation of discrete particle domains

The generation of discrete particle domains described in Section 4.2.2 yields not a single solution but a set of viable candidate domains. Each candidate domain satisfies the target bulk optical properties but differs in the microscopic “recipe” of sphere radius, refractive index, and concentration. Optimisation is therefore required to identify the most suitable candidate domain for subsequent T-matrix simulations.

This optimisation process has two components. The first concerns the selection of the optimal recipe from the list of viable candidates. As discussed previously, domains with equivalent macroscopic scattering behaviour can differ substantially in their computational cost when simulated. This is because the scaling behaviour of the T-matrix method scales with the number of spheres, and the truncation order (see Section 3.2.4). By evaluating candidate recipes using criteria such as the total number of linear equations to be solved, it is possible to identify computationally efficient domains with the desired optical properties.

The second component concerns specific geometrical constraints used to generate a given discrete particle instance. Once the optimal recipe is selected, a domain must be populated with individual spheres. The width of this simulation domain must be wide enough to minimise light escaping the sides of the simulation, but a narrower domain is more computationally efficient.

Together, these optimisation steps (sphere design and domain width) can be used to enable efficient T-matrix simulations of light propagation through discrete particle media.

4.4.1 Optimising the sphere design

One approach to optimising the computational efficiency of the discrete particle domain is to optimise the design of the constituent spheres. As mentioned in Section 4.2.2, an exhaustive search was undertaken to explore the discrete particle parameter space, which generated a 12 GB database of $\sim$25 million discrete particle domains.

As shown in Figure 4.3, a given domain with desired optical properties can be created in many ways using different permutations of scattering spheres. These optically identical discrete particle domains are called *"candidate"* domains - domains with the correct target optical properties but a distinct *"recipe"*, e.g. sphere sizes, refractive index contrast or concentration. To select the optimal candidate

domain, appropriate evaluation criteria must be selected.

Light propagation is simulated using the T-matrix method, and the computational efficiency of this method scales quadratically with the total number of linear equations (see Section 3.2.4). As such, candidate domains are evaluated based on the total number of linear equations created using a T-matrix formulation of the scattering problem - effectively a measure of computational efficiency. This is important as the computational complexity of simulating these candidate domains can vary by over an order of magnitude. The total number of linear equations T is given by Equation 3.19, which is repeated below:

$$T = 2N_s L_s(L_s + 2) \tag{4.14}$$

Where N_s is the total number of spheres in a given discrete particle domain of volume V, which is a function of the volume density v_f and radius r:

$$N_s = \frac{V v_f}{\frac{4}{3}\pi r^3} \tag{4.15}$$

L_s is the truncation order of the vector spherical wave function expansion and can be estimated using Wiscombe's criterion [161]:

$$L_s = \begin{cases} x + 4x^{1/3} + 1, & 0.02 \leq x \leq 8 \\ x + 4.05x^{1/3} + 2, & 8 \leq x \leq 4200 \\ x + 4x^{1/3} + 2, & 4200 \leq x \leq 20000 \end{cases} \tag{4.16}$$

Where x is the size parameter of the constituent spheres, $x = \frac{2\pi r}{\lambda}$.

The design goal is to find the correct combination of radius, refractive index and volume density that produces the lowest total number of linear equations while producing a domain with the target scattering coefficient and anisotropy. There are therefore two conflicting parameters to maximise and minimise, respectively.

Larger spheres at a lower concentration have a greater volume efficiency and consequently fewer are needed for a given domain, but larger spheres necessitate a much larger truncation order.

The process of optimising a discrete particle domain is as follows. The discrete particle database is searched to isolate the entries that generate domains with a scattering coefficient and anisotropy sufficiently close to target values. The list of viable domains is known as the *candidate domains*. To select the optimally efficient candidate, a 100 μm^3 sample volume is constructed, such that the total number of spheres can be determined from 4.15. Likewise, the truncation order is determined using Wiscombe's criterion (Equation 4.16). These values are applied to Equation 4.14 to determine the number of equations that need to be solved using the T-matrix method. The optimal candidate domain is therefore the domain that has the lowest number of linear equations. This optimal discrete particle *"recipe"* is used to populate a volume using the pseudorandom placement method described in Section 4.2.2.

To demonstrate the optimisation process, consider the process of designing a tissue-like discrete particle domain using the method described in 4.2.2. Section 4.2.1 defined generic tissue optical properties as a scattering coefficient of 15.6 mm^{-1} and an anisotropy of 0.9 at 633 nm. The discrete particle database created in Section 4.4.1 was searched to find *"recipes"* that produce a discrete particle *"candidate"* domain with matching optical properties, specifically a scattering coefficient of 15.6 ± 0.05 mm^{-1} and an anisotropy of 0.9 ± 0.005. Multiple candidate domains are found. A 100 μm^3 sample volume is constructed, such that the total number of spheres can be determined from Equation 4.15. The truncation order is determined using Wiscombe's criterion (Equation 4.16). These values are applied to Equation 3.19 to determine the number of equations that need to be solved using the T-matrix method. The candidate domains, and their associated number of linear equations, are plotted in Figure 4.11.

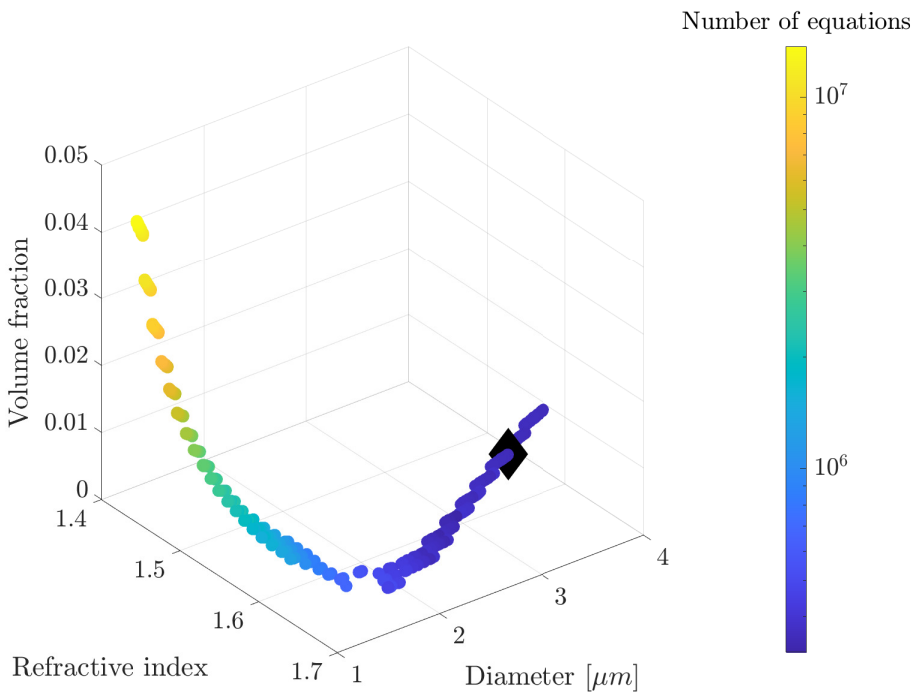

Figure 4.11: Fully dimensional visualisation of candidate discrete particle domains that achieve a scattering coefficient of $15.6 \pm 0.05 mm^{-1}$ and an anisotropy of 0.9 ± 0.005 (at a wavelength of λ = 633 nm). The black diamond indicates the discrete particle domain with the fewest number of linear equations, and therefore the most computationally efficient. This optimum domain is constructed from spheres with a radius of 1.72 µm a refractive index of 1.60 and a density of 0.77% by volume.

The most efficient domain has been determined as the one with the lowest number of linear equations, and is shown in Figure 4.11 by the black diamond. This domain is constructed from spheres with a radius of 1.72 µm a refractive index of 1.60 and a density of 0.77% by volume for a wavelength of 633 nm.

4.4.2 Optimising the medium width

Equation 3.19 shows that the computational complexity of the T-matrix method scales with the number of spheres. The number of spheres can be minimised by optimisation of the discrete particle *"recipe"*, as shown above. The number of spheres can also be minimised by simply decreasing the overall simulation volume.

For example, consider simulating light propagation through a X μm deep *"tissue-like"* discrete particle domain: how wide does the domain need to be? An insufficiently sized domain would allow a disproportionate amount of light to escape from the sides of the simulation. In theory, there is a relative *"sweet spot"* of domain width that is narrow enough to appropriately model the coherent phenomena of interest but not wide too be computationally inefficient.

In most computational methods, this optimisation is performed via convergence testing. Parameters such as simulation width or mesh density are increased until key measured quantities converge. However convergence takes a long time and the quantities used to assess convergence may not be representative of the convergence of the entire simulation. For example, a given speckle pattern may converge, but derived phenomena such as memory correlations or focus generation via WFS may still remain unconverged.

To optimise the width of a simulation medium faster and more accurately, a new metric was created that could quantify how much light reached a target window for a given domain. This technique is called *photons retained*. Photons retained is a measure of the proportion of light entering a simulation that stays confined within the simulation boundaries - rather than escaping from the sides of the simulation volume.

The Monte Carlo method (see Section 2.3.5.3) was used to simulate the fraction of propagating light that reaches a target region. As the goal of this thesis is to model WFS through a *"tissue-like"* medium, the optical properties of the simulation medium are chosen to match biological tissue. This means having a scattering coefficient of $10 \pm mm^{-1}$ an anisotropy of 0.9 and a refractive index of 1.38 [188].

To determine the optimal simulation width without repeatedly running computationally expensive forward models, a reverse simulation approach was used.

Instead of simulating the propagation of light into a medium and measuring how much reaches a target region, photons were launched from the target region, exploiting the principle of light reversal. The fluence distribution could then be measured as a function of depth, and thresholded for various simulation widths. This allows for the proportion of light that would be lost for a given simulation width to be quantified.

A 1000x1000x200 μm^3 simulation volume was created. The 1000 µm width relative to the 200 µm depth makes the simulation volume effectively infinitely large. A 50 µm wide pencil beam of photons was simulated propagating into the *"tissue-like"* medium (representing a 50 µm target region). Light propagation is simulated using the Monte Carlo method. The resulting fluence distribution across the 3D volume is shown in Figure 4.12.

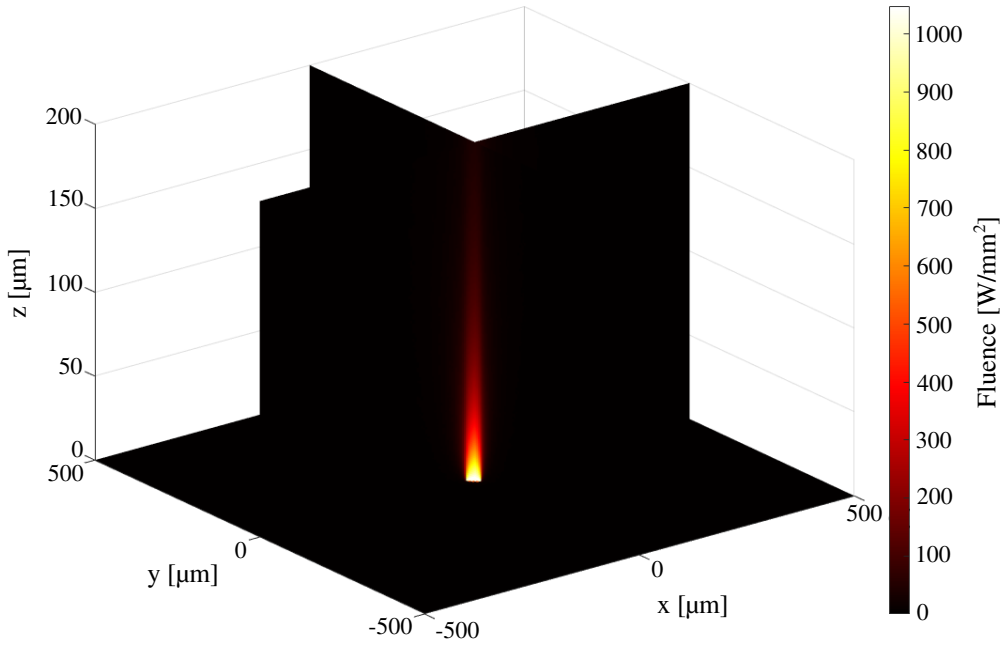

Figure 4.12: Fluence visualisation resulting from a Monte Carlo simulation of a 50 µm pencil beam propagating through a 1000x1000x200 μm^3 *"tissue-like"* volume. The fluence profiles derived from this simulation are used to derive the photons retained metric, which can be used to determine the simulation width for a given simulation depth. ValoMC was used for the simulation. [187].

To perform the Monte Carlo simulations, the mesh-based ValoMC was used [187]. Mesh width was defined as 1 µm, and all other settings were not changed from the default. Simulations were performed on Peter Munro's *"Zeus"* computer at UCL, which has two Intel Xeon Gold 6148 CPUs, a NVIDIA Quadro P6000 and 128 GB of RAM.

The fluence profiles are recorded at a depth of 50, 100, 150 and 200 µm across the 1000 µm x-axis. The fluence profile for the 100 µm depth is shown in Figure 4.13a.

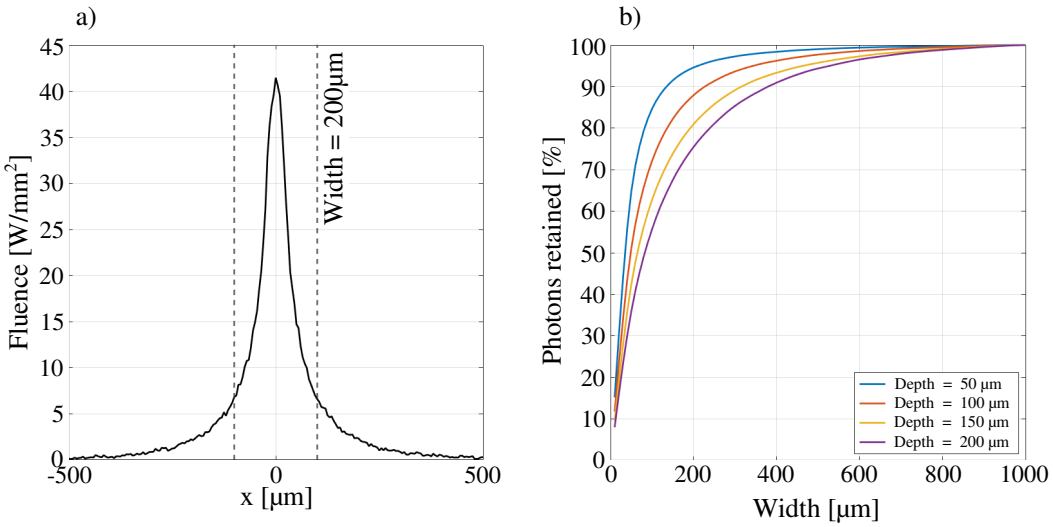

Figure 4.13: Graphs from which the photons retained metric can be derived. a) is a plot of fluence profile across a 1000 µm x line at y=0 and z=100 µm. A 200 µm threshold is set. The photons retained metric is defined as the area under the curve bounded by this threshold relative to the total area under the curve. This is an effective measure of the proportion of scattered light that would be lost from a simulation of width X. These derived photons retained values are plotted in b) for depths of 50, 100, 150 and 200 µm.

For a given depth, it is now possible to define a width threshold (e.g. 200 µm was used in Figure 4.13a). The area under the fluence curve was integrated, and the proportion of integrated light inside the width threshold is calculated relative to the total integrated light across all 1000 µm profiles. This effectively gives a measure of how much light would be lost out of the sides of the simulation if the simulation volume was constrained to a given width.

Expressed as a percentage, this proportion of thresholded light is defined as the *photons retained* metric and is plotted in Figure 4.13b. Using this graph, it is possible to determine the optimal width of a *"tissue-like"* simulation of light propagation of a given depth, based on a value judgement of what percentage of photons retained is satisfactory.

The photons retained metric is ultimately still a provisional method for determining the optimal width of a simulation domain. While it provides a convenient estimate of light lost, it rests on several assumptions and simplifications. First, there is no criterion for what fraction of photons must be retained to ensure accurate modelling of coherent phenomena. For example, whether 80%, 90%, or 95% retention is sufficient depends on what is being modelled.

Second, the assumption that the light incident on the target region can be modelled using a 50 μm pencil beam is not physically realistic. In reality, scattered light reaching the target region would have an angular distribution that is a function of the optical properties of the medium, the total scattering path length, and the incident light field. As the transport mean free path of this medium is 1 mm, it was assumed that over a 200 μm propagation depth, the scattering would be relatively weak. In this weakly scattering regime, a non-diffuse, collimated pencil beam was considered to provide a reasonable approximation to the angular distribution of the scattered light field.

Additionally, not all photons equally contribute to the development of a speckle pattern or the properties of coherent phenomena such as WFS or memory effects. Photons that travel along highly scattered, meandering paths may have highly unique phase profiles and thus influence interference-based phenomena in unknown ways. These meandering *"snake photons"* are more likely to be thresholded out if a photons retained metric is used.

Furthermore, the metric does not account for absorption. While absorption is weak for visible and NIR propagation through biological tissue (see Section 2.1.1), it may affect some photons disproportionately. For example, the meandering *"snake photons"*.

Lastly, the metric assumes a uniform incident field, e.g. a plane wave. If WFS is modelled using the random medium method of modelling input modes (see Section 6.4.2), then Gaussian beams are used. In such cases, the required simulation width may be smaller than that predicted using photons retained.

Ultimately, the photons retained metric was a preliminary investigative technique used to assess the viability of reducing the width of a given simulation domain. The results presented in Figure 4.13b were still useful in highlighting the practical challenges of domain width optimisation. Specifically, they showed that narrowing the simulation domain too aggressively can lead to a greater loss of photons than expected, particularly as depth increases. Critically, the contributions of these laterally escaping photons to coherent phenomena are unknown.

4.5 Chapter summary

This chapter developed and validated a framework for designing discrete particle media compatible with T-matrix simulations. The key contributions are as follows.

First, the mapping from particle-level parameters (sphere radius, refractive index, and concentration) to bulk optical properties was formalised through Mie theory, enabling the creation of "recipes" for replica turbid media with bespoke scattering coefficients and anisotropies. A large-scale exhaustive search generated a database of over 25 million candidate domains, providing a reusable resource for designing tissue-like scattering media.

Second, novel optimisation strategies were introduced to improve computational

efficiency. Candidate domains with equivalent macroscopic properties were compared based on the total number of T-matrix equations, allowing identification of the most efficient sphere configurations. In addition, the photons retained metric was proposed as a practical tool for determining optimal medium width, balancing computational efficiency with accurate modelling of light transport.

Third, a robust validation framework was established. IAD confirmed that designed domains reproduced target scattering coefficients and anisotropies; Monte Carlo comparisons verified that ensemble-averaged T-matrix simulations reproduced correct macroscopic transport behaviour; and angular memory effect studies demonstrated preservation of higher-order speckle correlations. Together, these validations confirmed that the framework produces synthetic turbid media with the correct optical properties across microscopic, mesoscopic, and macroscopic scales.

Overall, this chapter provides a complete and optimised method for designing T-matrix-compatible scattering media, with reusable tools for recipe selection, validation, and optimisation. These advances establish the foundation for the WFS simulations that follow.

Chapter 5

Modelling light focusing via wavefront shaping

In the previous two chapters, a computational framework was constructed and validated to simulate light propagation through bespoke scattering media. In this chapter, the framework is used to model the focusing of light through and inside scattering media via WFS.

The scope and contributions of this chapter are threefold. Firstly, the angular spectrum method is combined with the T-matrix propagation framework to create a new method of modelling input modes that is a close computational analogue of experimental WFS setups. Secondly, the seminal experimental demonstration of WFS by Vellekoop and Mosk [7] is replicated *in silico* as an optical focus is generated through a highly scattering titanium dioxide layer. The enhancement of this focus is validated against theory and found to be consistent with it. Finally, the framework is extended to provide a preliminary exploration of multi-focal generation and the role of spatial correlations in determining enhancement.

The chapter proceeds as follows. First, the background of WFS is reviewed using a transmission matrix formalisation. This includes a discussion on the methods of modelling input modes (experimental design, angular spectrum theory), and output modes (enhancement theory, N/M). Then, the methods of constructing a

simulation of light focusing via WFS are constructed. Next, the computational framework is demonstrated, focusing light through a titanium dioxide layer. The model is then extended to generate an internal focus and investigate multiple foci. Finally, the chapter concludes with a discussion of potential directions for further development and a summary.

5.1 Background

As discussed in Chapter 2, light incident on turbid media scatters, reducing intensity as a function of depth and eroding spatial coherence. This scattering is an aggregation of numerous small-scale scattering events resulting from microscale refractive index inhomogeneities within the medium. WFS exploits the deterministic nature of this light propagation to compensate for scattering's deleterious effects by optimising light propagation through turbid media. In effect, WFS facilitates the creation of beneficial light patterns, such as optical foci, which result in higher fluence and improved imaging capabilities [7].

In the previous two chapters, a computational framework has been designed that couples the full-wave T-matrix method with a discrete particle model of scattering media. This framework has been extensively validated at the micro-, meso-, and macroscales. In the following chapter, optical foci are generated through a titanium dioxide phantom, replicating the first experimental demonstrations of WFS by Vellekoop and Mosk [7].

Recall from Section 2.2.2 that WFS can be formalised through a transmission matrix framework, which describes the coupling between arbitrary input modes and output modes across a given medium. Thus, constructing a WFS model involves three key components: modelling the input modes, the transmission matrix, and the output modes.

5.1.1 Modelling input modes

Selecting input modes involves choosing a basis with orthogonal elements that can be phase or amplitude modulated. As discussed in Section 2.2.1, WFS experiments use devices like spatial light modulators (SLMs) or digital micromirror devices (DMDs) to modulate the incident wavefront. By dividing the input beam into many segments (pixels) and imparting a controllable phase (or amplitude) shift to each, the SLM effectively prepares a set of input modes that interfere to form a desired intensity pattern after a scattering sample.

A thin lens then Fourier-transforms this modulated field into an angular distribution of light on the sample [134]. By adjusting the phase of each SLM segment, experimenters selectively control the angular spectrum of the incident field (albeit with an unknown mapping between SLM element modulation and the resultant angular spectrum phase shifts). This direct connection motivates the use of the angular spectrum method as a mathematical framework for representing input modes when constructing a model of WFS.

The angular spectrum method represents an arbitrary optical field as a superposition of plane waves, each propagating at a different angle. These plane waves are characterised by their angle of incidence, defined by a polar angle θ and an azimuthal angle ϕ, and take the general form:

$$E(x,y,z) = e^{i(k_x x + k_y y + k_z z)} \tag{5.1}$$

where $k_x = k\sin\theta\cos\phi$, $k_y = k\sin\theta\sin\phi$, and $k_z = k\cos\theta$. In practice, the angular spectrum is discretised into a finite set of plane waves. In the proposed model of WFS, these plane waves are then simulated individually using the T-matrix method. The T-matrix method calculates the scattered field for each incident angle, thereby creating a mapping between the input modes (plane waves incident at a particular angle) and the output modes (light fields at the target region).

5.1.2 Modelling the transmission matrix

As constructed and validated in Chapter 4, bespoke scattering media can be modelled using the discrete particle approach. In practice, this entails selecting desired scattering coefficient and anisotropy values and using Mie theory to construct a discrete particle medium with said optical properties. The specific *"recipe"* for this domain is defined by sphere radii, refractive indices, and densities. Consequently, custom scattering media can be constructed and utilised as inputs for a T-matrix solver.

5.1.3 Modelling output modes

Choice of output modes is similarly arbitrary (e.g., the light field behind a medium projected onto an imaging device). One advantage of the full-wave T-matrix method is its ability to evaluate the complex scattered field at arbitrary points, including within a medium.

In practice, WFS is typically used to focus light into a single output mode, generating an optical focus through or inside a scattering medium. The spatial modulation required to generate this focus can either be amplitude-based (e.g. using a DMD) or phase-based (e.g. using an SLM). The specific method of modulation determines the maximum possible enhancement, η, with full phase and amplitude control, achieving an enhancement of [189]:

$$\eta_{\text{pred}} = \alpha(N-1)+1 \tag{5.2}$$

where N is the number of elements used to control modulation and α represents an enhancement factor that can be used to characterise the efficiency of other modulation methods (see Table 5.1).

Another important consideration is the N/M theory, which relates the achievable enhancement to the ratio of controlled input modes N over the number of output modes M in the target region. If the focal spot or detection area (region of in-

Table 5.1: Maximum possible enhancement for different spatial modulation methods. Data taken from Vellekoop *et al.* [34]

Modulation Method	α
Full phase	$\pi/4$
Binary phase	$1/\pi$
Binary amplitude	$1/2\pi$

terest) encompasses M independent speckle grains (output modes), the maximum enhancement is effectively diluted over those modes. In general, the enhancement ratio scales approximately as $\frac{N}{M}$ (with the same α factor as above) [190]. In other words, to maximise the focus intensity relative to the background, one should maximise N (the number of controllable segments) and minimise M (focus on a single speckle-sized target if possible). For instance, focusing light onto a single optical mode (speckle grain) with a high-N SLM can produce enhancements of order N (thousands-fold intensity increases have been reported [7]), whereas focusing onto a larger spot that covers multiple speckle grains will yield a lower enhancement since the same optimised input is shared among M modes.

5.2 Methods

5.2.1 Applying the computational framework

The overall structure of the modelling framework constructed and validated in Chapters 3 and 4 is shown in Figure 5.1. The process to apply the framework to model WFS is therefore as follows.

The first step is to construct a simulation domain with prescribed optical properties using Mie theory, as described in Section 4.2.2. Incident light is then defined in terms of a set of input modes. These can be individual plane waves or Gaussian beams, or an angular spectrum that can be independently spatially modulated to model WFS. The T-matrix method is used to simulate the propagation of each input mode through the medium (see Section 3.3), yielding complex field distributions that can be used to model WFS and other coherent phenomena.

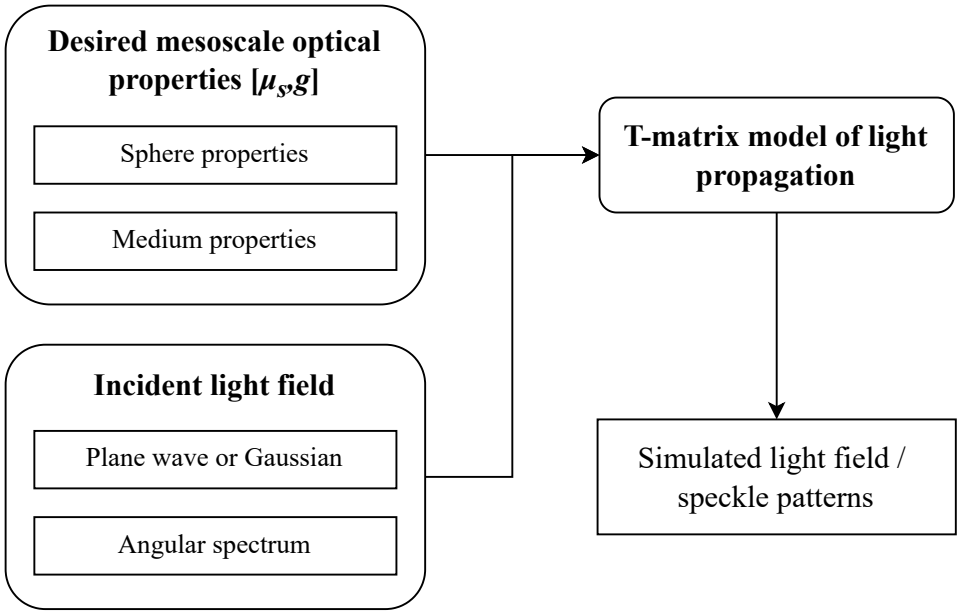

Figure 5.1: Overview of the proposed method for simulating light propagation and modelling WFS. Mesoscale optical properties, such as the scattering coefficient and anisotropy, are specified as targets. Mie theory is used to select appropriate sphere and medium properties that yield the desired scattering behaviour. The incident light field (defined as a plane wave, Gaussian beam, or angular spectrum) is propagated through the domain using the T-matrix method. This produces a simulated light field or speckle pattern that can be used to model WFS or other coherent optical effects.

The process of defining the method for modelling the input modes is now defined.

5.2.2 Angular spectrum modelling of input modes

The complex spatially modulated incident light fields found in WFS are modelled using an angular spectrum decomposition. As discussed in Section 5.1.1, this approach is directly analogous to the experimental situation of an SLM and lens. In the proposed method, the complex input field is broken down into a discrete set of plane wave modes, each characterised by a unique incident angle (spanning a chosen range of angles in θ and ϕ). Practically, each plane wave mode is realised as a separate T-matrix simulation of a collimated beam entering the scattering sample at that angle.

Specifically, input modes were sampled uniformly from -10° to $+10^\circ$ in both angular dimensions, resulting in a total of 441 distinct plane waves. The propagations of these plane waves are simulated independently using the T-matrix method, which solves for the complex electric and magnetic fields across a target region.

Modelling input modes using this method has several advantages. First, the *in silico* modelling of these input modes can be replicated in experimentation. Each incident plane wave can be represented on an SLM by applying a linear phase ramp across its surface.

Second, the method is efficient to simulate. The T-matrix calculations for each input mode are independent and can be calculated in parallel. Multiple machines or clusters can be put to work to independently simulate different incident angles.

Third, the mappings between the plane wave input mode and the scattered field can be reused. Arbitrary complex fields can be represented using an angular spectrum decomposition. For example, consider simulating the propagation of an arbitrary incident field through a medium. Rather than run a new T-matrix simulation, the scattered field can be calculated via superposition of the appropriate spatially modulated plane wave input modes. This assumes enough plane waves have been defined at an appropriate angular discretisation to represent the incident field.

Fourth, modelling input modes using an angular spectrum enables direct investigation of other coherent phenomena such as the angular memory effect (AME). Since each input mode corresponds to a distinct angle of incidence, the degree of correlation between output speckle patterns provides a way to quantify the AME.

5.2.3 Optimising incident light

To illustrate the proposed method, the generation of an optical focus through a highly scattering titanium dioxide layer is simulated, as shown in Figure 5.2.

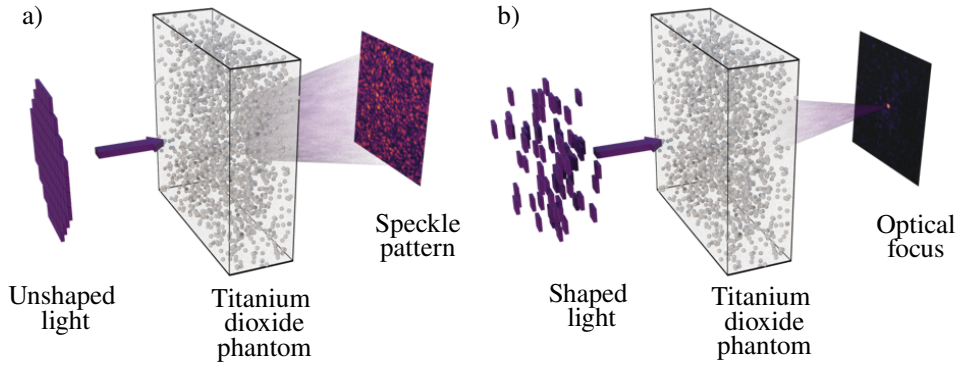

Figure 5.2: a) Light incident upon a highly scattering medium is multiply-scattered, resulting in the production of a fully developed optical speckle pattern forming on a plane behind the medium. b) Appropriately structured light propagates through the same medium such that the transmitted field interferes to produce an optical focus at the same plane in a defined target.

The titanium dioxide discrete particle *"recipe"* was designed in Section 4.3.1 to match the optical properties used in the seminal Vellekoop and Mosk paper [7]. This domain has a TMPF of ∼5 μm and a scattering coefficient and anisotropy of $\mu_s = 445\ \text{mm}^{-1}$ and $g = 0.55$. The wavelength of the incident light was $\lambda = 633$ nm. The domain was constructed from 1 μm radius spheres with a refractive index of 2.5836 (in a 1.33 background) at a volume fraction of 0.26. A 30x30x10 μm^3 was populated with these spheres using a pseudorandom positioning method outlined in Section 4.2.2. Recall that this exact domain has been validated using IAD and Monte Carlo, as demonstrated in Sections 4.3.2 and 4.3.3 respectively.

5.2.4 Spatially modulating input modes

Once a set of input modes has been defined, the propagation of these plane waves through the medium is simulated using the T-matrix method. This creates a linear mapping from input modes to output modes. The output modes are typically defined as a near-field plane of interest inside or past the medium.

The link between each input mode and the output modes is linear - a shift of 2π across the input mode produces a 2π shift across the near-field of the associated output mode. As the T-matrix method is capable of calculating the complex field, these phase shifts can be applied to either the input mode (before simulation) or

after (with post-processing).

The stepwise sequential algorithm was used [49] to determine what phase shift is needed to model WFS and simulate the generation of an optical focus. This is because the stepwise sequential algorithm is guaranteed to find the optimal spatial modulation that results in the highest enhancement focus 2.2.3. Briefly, a single input mode and resulting field were chosen as a reference. The fields resulting from every input mode were added to this reference, after applying a sequence of phase shifts ($2\pi/64$). From each set of resulting fields, the phase shift yielding the highest intensity at the target location was selected and the corresponding field stored. Finally, the stored fields were summed together to synthesise the total field produced by a beam comprising the entire phase-modulated angular spectrum.

A simplified process can be applied for binary phase modulation (see Table 5.1), with only phase modulations of 0 or 2π being used. The process for binary amplitude modulation is even simpler still. No phase modulation is applied to each input mode; either the linear combination of the output field and the reference increases the intensity at the target location or reduces it. Those that resulted in an increase were stored and summed together to synthesise the optimised field.

5.3 Modelling light focussing

5.3.1 Light propagation through a titanium dioxide domain

Light propagation of a single input mode directly incident on the domain was simulated using CELES on Zeus, and took approximately 4 hours to complete. Specifically, a plane wave with a wavelength of 633 nm was simulated propagating through this domain along the z-axis, and the resulting electric field distributions are shown in Figure 5.3. Visualising the internal and transmitted fields is important as it confirms that the Vellekoop and Mosk-inspired phantom is sufficiently scattering to be useful for modelling WFS. This would be the case if a fully formed speckle pattern is generated through the medium, as expected after two TMFPs.

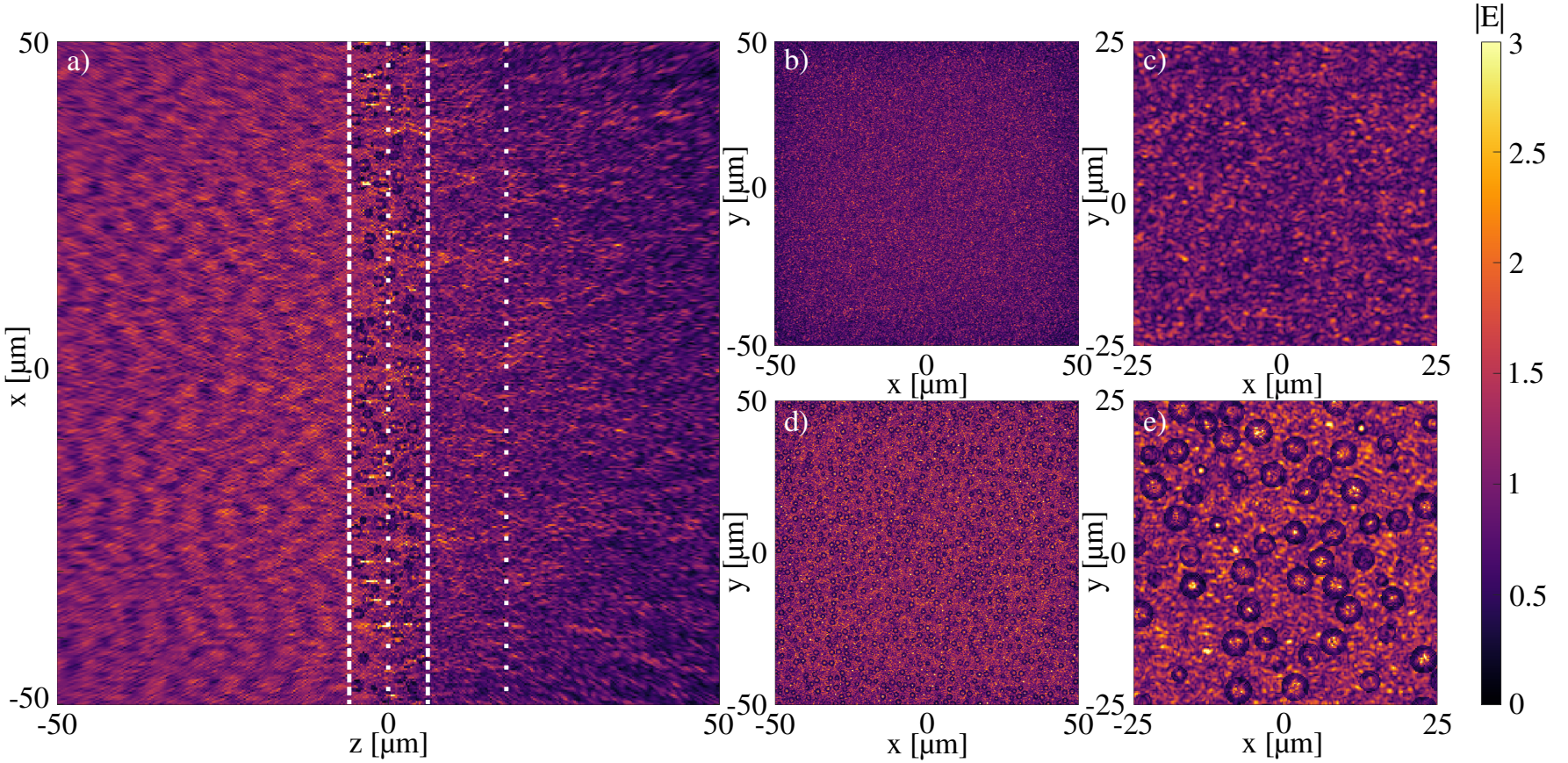

Figure 5.3: Electric field magnitudes resulting from plane wave propagation through a 100x100x10 µm^3 titanium dioxide domain with a TMFP of ∼5 mm. a) Field magnitude in the transverse *xz* plane bisecting the medium. White dashed lines delineate the boundaries of the discrete particle medium. Dotted lines delineate the location of the transverse planes b-e. b) and c) Field magnitude in the 100x100 µm^2 and 50x50 µm^2 *xy* pltitaniumanes at $z = 15$ µm. d) and e) Field magnitude in the 100x100 µm^2 and 50x50 µm^2 *xy* planes at $z = 0$ µm.

The electric field distributions shown in Figure 5.3 are, firstly, further clear demonstrations of how the T-matrix method can be used to simulate coherent light propagation through bespoke scattering media. The Figure reveals the emergence of a fully developed speckle pattern consistent with propagation through approximately two TMFPs.

In Figure 5.3a, the magnitude of the electric field is shown across the xz plane bisecting the medium. The 10 μm thick discrete particle medium is delineated by the dashed white lines. The field before the medium is uniformly more intense than the field after the medium, consistent with significant light scattering caused by the titanium dioxide particles. Regular backscattering fringes can be seen in the field before the medium, arising from the constructive and destructive interference of backscattered light with the incident plane wave.

Subfigures b) and c) depict the transverse field magnitude distributions at $z = 15$ μm across a 100x100 μm^2 and 50x50 μm^2 plane, respectively. As expected for two TMFPs, a seemingly random speckle pattern has developed at both scales. The field statistics were examined and found to be Rayleigh distributed, suggesting that the speckle was well-developed [167]. The magnitude across the boundaries of b) is slightly less intense, the result of light escaping from the sides of the simulation. The inner 50x50 μm^2 plane shown in c) shows the speckle pattern more clearly. The fully developed speckle field appears as an irregular landscape of light field peaks and nulls. The brightest spots locally exceed the incident field magnitude due to constructive interference, while nearby dark spots approach zero amplitude due to destructive interference. These features confirm that the medium induces sufficient scattering to decorrelate the input and output fields, a necessary condition for modelling WFS.

Subfigures d) and e) instead both show the field magnitude directly inside the medium, at $z = 0$ μm. The magnitude across the plane is, on average, much brighter

than the fields after the medium. This is due to light undergoing less scattering at this distance of 5 μm. Like subfigures b) and c), the field has developed into a speckle pattern with irregular peaks and nulls caused by constructive and destructive interference. However, the scattering spherical titanium dioxide inclusions can be seen throughout the field. The particles are surrounded by a dark ring profile corresponding to the radius of the particle. The field should be smoothly varying without discontinuities. This behaviour, specific to CELES, was identified during Mie theory validation and discussed in Section 3.4.2.

The fields depicted in Figure 5.3 are evidence that the T-matrix method is capable of simulating the propagation of light through highly scattering media and generating fully developed speckle patterns. These results support the use of this domain in subsequent simulations for the purposes of validating the discrete particle framework used to design and construct the domain.

5.3.2 Focusing through and inside a titanium dioxide domain

A target plane was first defined 20 μm behind the turbid titanium dioxide layer. To show the field produced by a single, unshaped, plane wave, a simulation was performed in which the layer was illuminated at normal incidence. The magnitude of the electric field was evaluated in an axial plane bisecting the layer, and plotted in Figure 5.4a. As expected, before the layer, the field distribution is relatively uniform, albeit containing weak interference effects due to the backscattered light. Inside the layer, the light distribution quickly develops a fine, seemingly random structure. The sphere boundaries are also clearly visible. The distribution qualitatively appears to become more randomised the further into the medium the light propagates. Behind the medium, the magnitude of the electric field is, on average, lower, and the random distribution of light elongates as the transmitted field expands.

To visualise the resulting transmitted light pattern, the magnitude of the electric field in a 30x30 μm^2 transverse plane behind the layer (dashed line in Figure 5.4a)

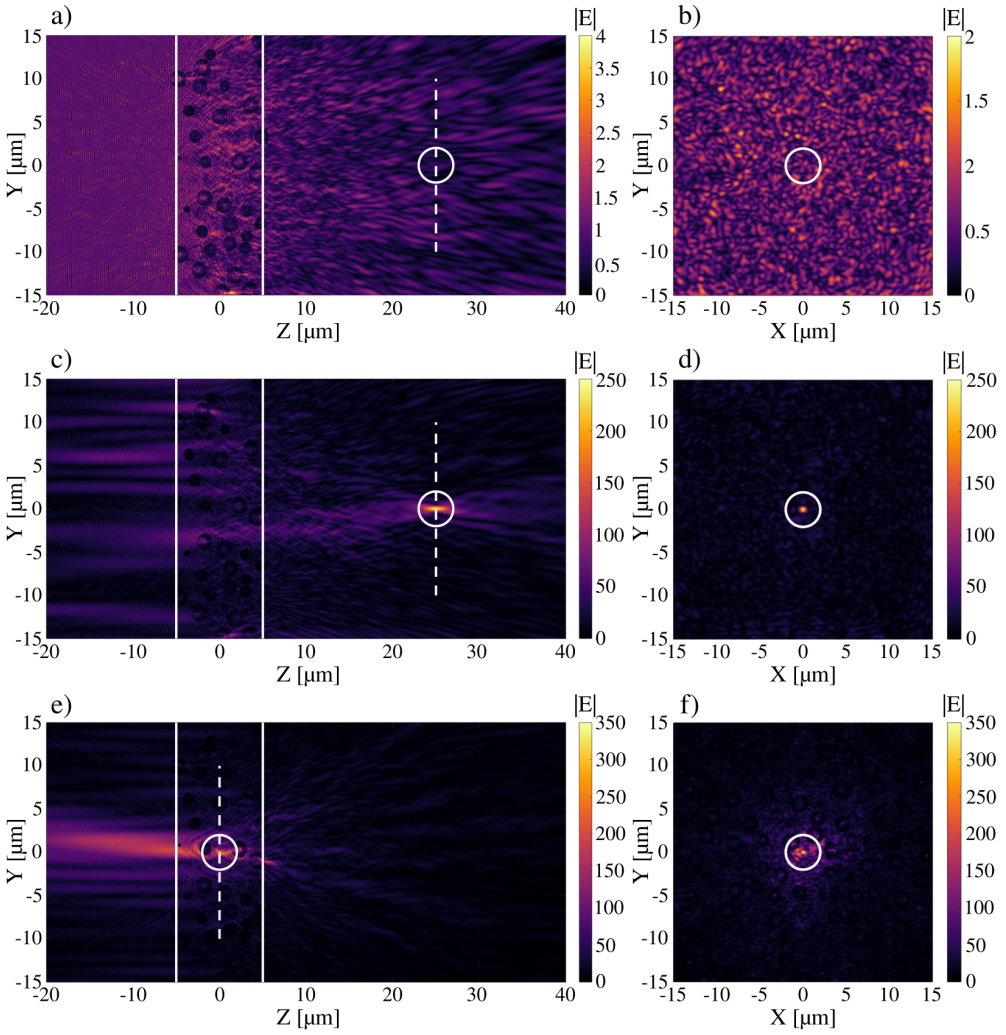

Figure 5.4: Simulation of light transmission and focusing through and inside a turbid layer. The images are 2D slices through the 3D light field calculated for three different incident wavefronts, namely: (a-b) a normally incident plane wave, (c-d) a structured beam optimised using an iterative WFS algorithm to focus light into a point located behind the medium at the location of the white circle; (e-f) a structured beam optimised using the same process, with the target positioned inside the medium. The planes on the left-hand side (a, c, e) bisect the medium, parallel to the optical axis. The planes on the right-hand side (b, d, f) are perpendicular to the optical axis and are positioned along the dashed line.

was evaluated and plotted in Figure 5.4b. As expected, there exists a seemingly random speckle pattern. The speckle statistics were examined and found to be Rayleigh distributed, suggesting that the speckle was well-developed [167]. This plane would be analogous to the field pattern that may be captured on a CCD placed behind the medium. At the centre of this plane, a white circle marks the location of

the target region into which light will be focused.

Next, to generate a focus through the medium, the field produced by a beam comprising an angular spectrum of 441 plane waves, optimally phase-shifted to focus at a target location, was calculated. These 441 plane waves represent a 1° angular spacing from -10° to 10°, both polar and azimuthal (as described in Section 5.2.2). To select the phase shifts, a procedure similar to a stepwise sequential algorithm [7] was used. This method was described in Section 5.2.4. Briefly, each plane wave comprising the angular spectrum was simulated sequentially on Myriad. The directly incident plane wave was isolated and treated as a reference. The field of every other plane wave was summed with the reference field, after applying a sequence of phase shifts $(2\pi/64)$. From each set of resulting fields, the phase shift yielding the highest magnitude at the target location was selected, and the corresponding field was stored. Finally, the stored fields were summed together to synthesise the total optimised field. This is analogous to directly simulating the propagation of the optimised field through the medium and calculating the scattered field.

The white circle in Figure 5.4a, b, c and d define the location of the first target - along the origin 20 μm behind the scattering layer. After applying the WFS procedure described above, the resulting field distribution in the axial plane was plotted in Figure 5.4c. Unlike the previous field distribution (Figure 5.4a), the field before and inside the medium has a much coarser structure, with a greater confinement of light in certain spatial regions. This is consistent with a spatially modulated field. Beyond the layer, parts of the field appear to converge towards the target location, with the resulting interference creating a bright axially-elongated focus.

To show the resulting electric field magnitude in the *xy* plane, this was plotted in Figure 5.4d. As expected, there exists a bright focus in the centre of the plane. The focal enhancement (change in the peak to background ratio due to the WFS [189]) was found to be 346. The simulation was repeated five more times with

different target locations within the same plane, and similar results were observed (the translation of this optical focus will be discussed later). Across the repeats, the mean enhancement was 348 and the standard deviation was 7, in agreement with the maximum theoretical enhancement of 347 as derived from Equation 5.2.

To expand on the demonstration provided by Vellekoop and Mosk [7], the input modes were then optimised to focus light inside the scattering medium. Recall from Section 2.2.1.1 that it is not possible to directly focus light inside a medium experimentally, as there is no way to directly resolve the internal light distribution. Instead, an indirect guidestar must be used [35]. The proposed computational framework has no such limitation, as the field can be calculated at arbitrary locations.

To simulate focusing inside the layer, the WFS simulation was repeated with the target location moved to inside the medium, at a depth of 5 μm. This new target is shown by the white circle in Figures 5.4e and 5.4f. The transverse plane (shown by the dashed line) was also moved such that the new target is located at the origin. After applying the same WFS procedure, the resulting light field distribution in the axial plane was plotted in Figure 5.4e. As expected, the incident light field is structured differently from Figure 5.4c, owing to the different spatial modulation. The light field is far more localised and has a greater magnitude. Same as before, the resulting interference causes a focus to be generated at the target location.

To help visualise the focus, the magnitude of the electric field was once again evaluated in the focal plane and plotted in Figure 5.4f. While the magnitude is greater (than in Figure 5.4d), the optical confinement is visually poorer.

To further demonstrate the flexibility of the computational framework, additional simulations were performed to explore the effect of varying the input field modulation and target geometry. These results are shown in Figure 5.5.

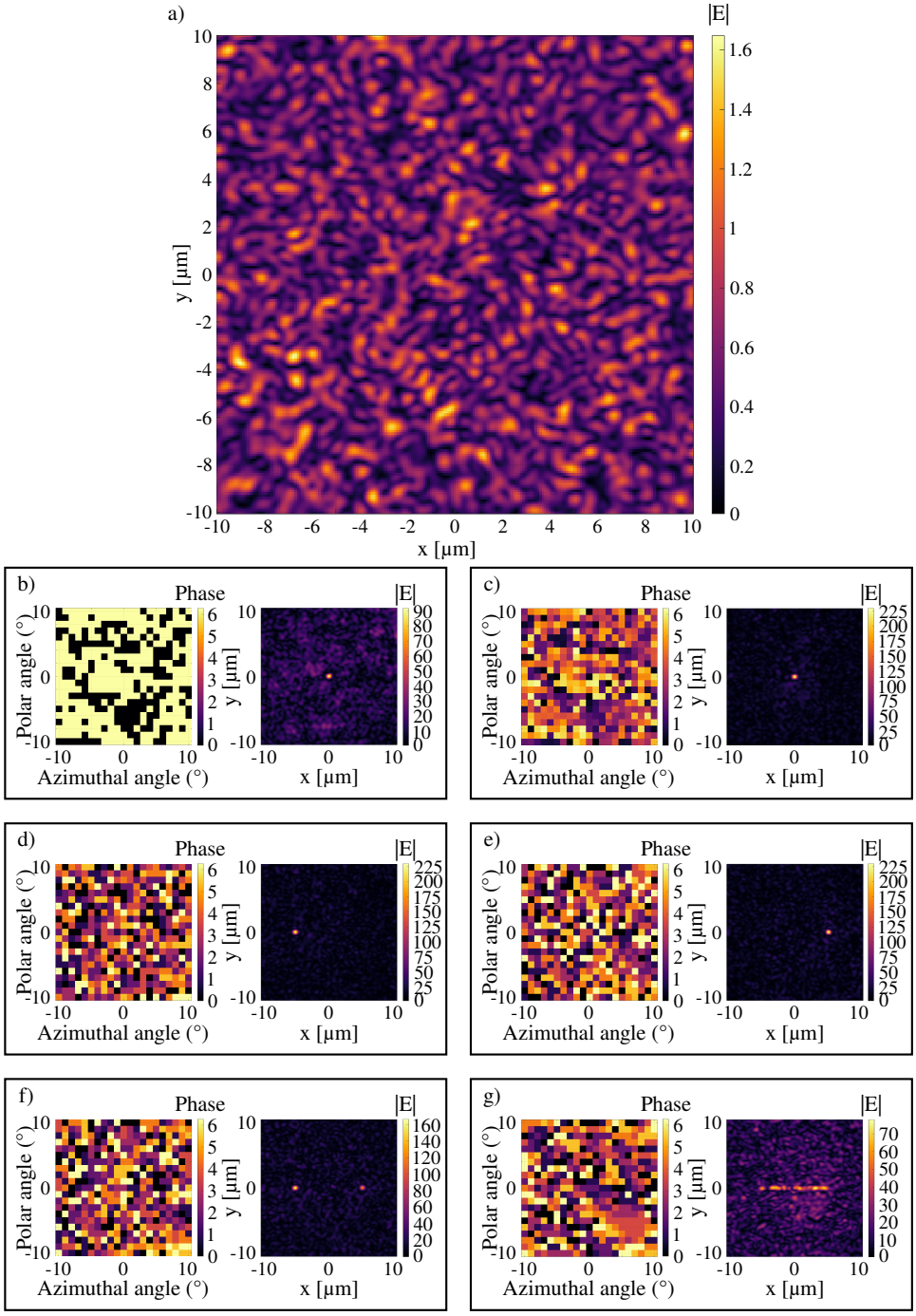

Figure 5.5: Modelling the generation of an optical focus through a scattering layer with various methods of spatial modulations of the incident field. a) the speckle pattern generated by propagating a plane wave through a highly scattering titanium dioxide layer. b-g) are paired sets of the optimised phase modulation across the 411 input modes (left), and the resultant shaped light field (right). b) shows binary phase modulation, while c-g) are full phase-modulated light fields. For c,d,e) light is optimised to generate a focus inside a singular target region that is translated along the x axis. f) shows light being focused into two foci simultaneously. g) is an attempt to optimise the light field to create a continuous line from $-5 < x < 5$ μm. All foci have been generated using the stepwise sequential algorithm.

In Figure 5.5a, the baseline speckle pattern generated by illuminating the scattering layer with a normally incident plane wave is shown again. As previously observed, the pattern is spatially random. In subsequent simulations (Figure 5.5b–g), the phase modulations of each input mode have been shifted in different ways to generate unique light fields. As before, this modulation was performed with the stepwise sequential algorithm. Figures 5.5b–g show both the optimised phase modulation (left) and the resultant shaped light field (right).

In Figure 5.5b, light was focused into the same target region behind the scattering medium at $x = 0$, $y = 0$, and $z = 25$ as in Figure 5.4. A binary phase modulation was used to optimise the scattered light field, in which each input mode plane wave was restricted to either 0 or 2π phase shifts.

The enhancement of the binary phase modulated focus was calculated to be significantly lower than that of the full phase modulation shown in Figure 5.4 and replicated in Figure 5.5b (140 vs 346). This result matches the theoretical enhancement for binary phase modulation of 141, calculated by inputting the correct value of η from Table 5.1 in Equation 5.2. This diminished enhancement is indicative of a poorer confinement of light and lower intensity within the target region. This can be seen by comparing the optimised field patterns in Figures 5.5b and c. The electric field magnitude of the binary phase modulated focus is lower than the full phase focus.

Figures 5.5c–e illustrate the spatial flexibility of the focusing algorithm. In these simulations, the same full phase modulation procedure was used, but the target region was systematically translated laterally along the x axis. As expected, the position of the optical focus follows the location of the target region, and the enhancement remains roughly consistent across translations.

In Figure 5.5f, the procedure was adapted to simultaneously focus light into two

separate target regions. The phase mask was optimised to maximise the sum of the electric field magnitudes at both points. The resulting field exhibits two well-defined peaks, confirming the capability of the system to generate multiple simultaneous foci.

Finally, in Figure 5.5g, the simulation target was changed from a point to an extended region: specifically, a linear segment spanning $-5 < x < 5$ µm. The input phases were optimised to maximise the summed field magnitude across this continuous line. The resulting field shows a broadly linear structure, albeit with speckle-sized fluctuations across the target region. A greater number of simulated input modes would result in an even smoother variation. This simulation demonstrates that the method can focus light into arbitrary target regions.

To further illustrate this, simulations were conducted in which the optimisation target was defined not as a single point, but as a circular region of increasing radius. The results are shown in Figure 5.6. As expected, increasing the size of the target region resulted in a broader, weaker focus. This behaviour arises because the same incident power is distributed over a larger area, as described by N/M theory introduced in Section 5.1.3. Despite this, clear energy localisation was observed within each region, confirming the method's ability to target extended volumes.

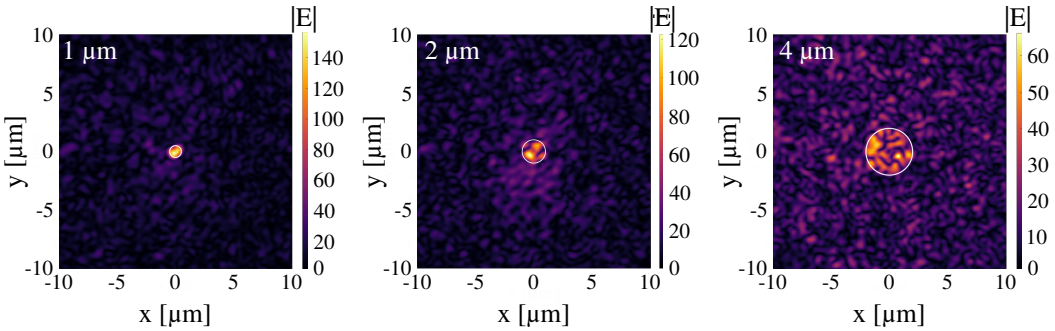

Figure 5.6: Simulating the focusing of light through a highly scattering titanium dioxide layer into target regions of different radii.

This capability is particularly relevant for modelling guidestar-assisted WFS, in which direct measurement of the light field at the target location is not possible.

Instead, an indirect, potentially lower-resolution measurement is used as feedback for the optimisation algorithm (see Section 2.2.1.1 for a discussion of guidestar-assisted WFS).

Finally, one of the unique benefits of using a full-wave computational model is the ability to access and visualise the entire 3D light field within and around the scattering medium. Figure 5.7 shows a volumetric rendering of the electric field magnitude in the 5 μm^3 region surrounding focus generated in Figure 5.4. Transparency is scaled with magnitude to enable visualisation of the focus within the volume. This type of volumetric visualisation is not directly measurable in most experiments of WFS. It could provide valuable insight into how interference structures form within turbid media and can guide future design of WFS strategies.

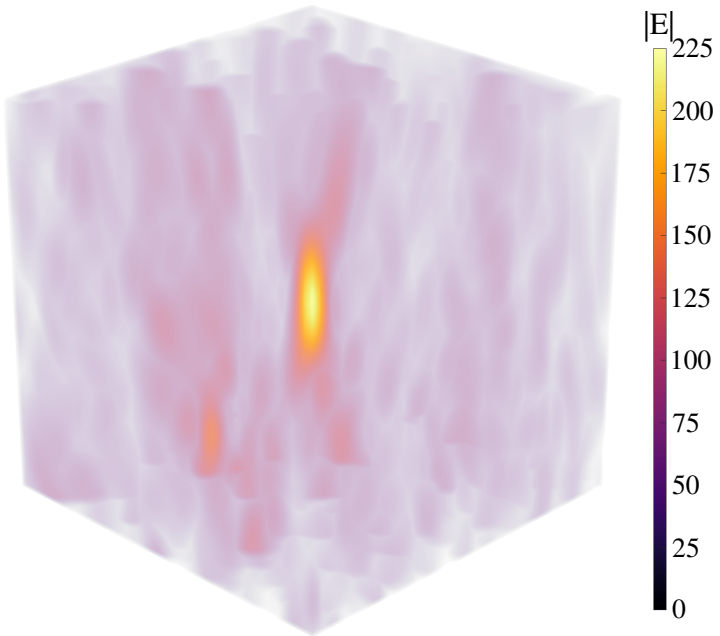

Figure 5.7: 3D visualisation of the focus generated through a titanium dioxide slab using full phase modulation. The electric field magnitude is calculated in a 5 μm^3 volume surrounding the target region. Transparency is scaled with magnitude to visualise the focus formed inside the volume.

5.3.3 Evaluating enhancement

A key metric in WFS is the enhancement, η, defined as the ratio between the peak intensity of the optimised focus and the average background intensity prior to any shaping. This quantity captures the effectiveness of optical control through a scattering medium and scales linearly with the number of independent input modes (see Section 5.1.3).

To investigate how enhancement scales with the number of input modes in the proposed computational framework, a series of simulations was performed in which an optical focus was generated through the same titanium dioxide domain designed to replicate Vellekoop and Mosk [7]. An optical focus was generated for different subsets of the total 441 input modes, and the enhancement was calculated. The results are shown in Figure 5.8.

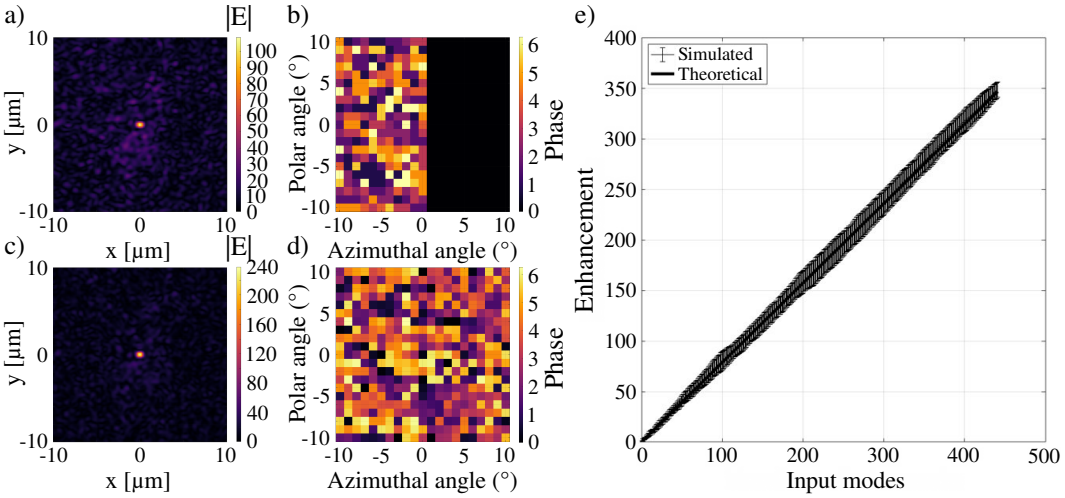

Figure 5.8: Optical foci generated through the titanium dioxide layer from Chapter 5 using full-phase wavefront control. a,c) shows the optimised phase masks, while b,d) show the associated foci generated across a 20 µm^2 plane 20 µm behind the medium. a,b) optimise just over half the available input modes, while all modes are optimised for c,d). e) shows a plot of enhancement (η) vs the number of elements (N) used to generate a focus. Each element is a plane wave propagating through the medium at a different incident angle. The theoretical relationship between enactment and number of input modes is also plotted, and is defined in Equation 5.2.

When all 441 input modes were used, a bright and well-confined optical focus was formed at the target location. As expected, using fewer input modes resulted in a lower enhancement, although a focal spot remained visible. The WFS simulation was repeated five more times with different (off-centre) target locations within the same plane, to generate a standard deviation for the enhancement. The mean enhancement as a function of input modes was plotted in Figure 5.8e. As expected, enhancement scales linearly with the number of independent optimised input modes, and aligns with theoretical predictions from Equation 5.2.

To assess whether theoretical predictions for enhancement scaling extend to more complex light control tasks, the case of generating multiple foci simultaneously was investigated. Using the same sequential algorithm, phase masks were computed to maximise the combined intensity at two, three, four, or five target locations, all positioned within the same transmission plane behind the scattering layer. The resultant pentagonal five-point focus is shown in Figure 5.9, as is the enhancement as a function of the number of input modes for multiple foci.

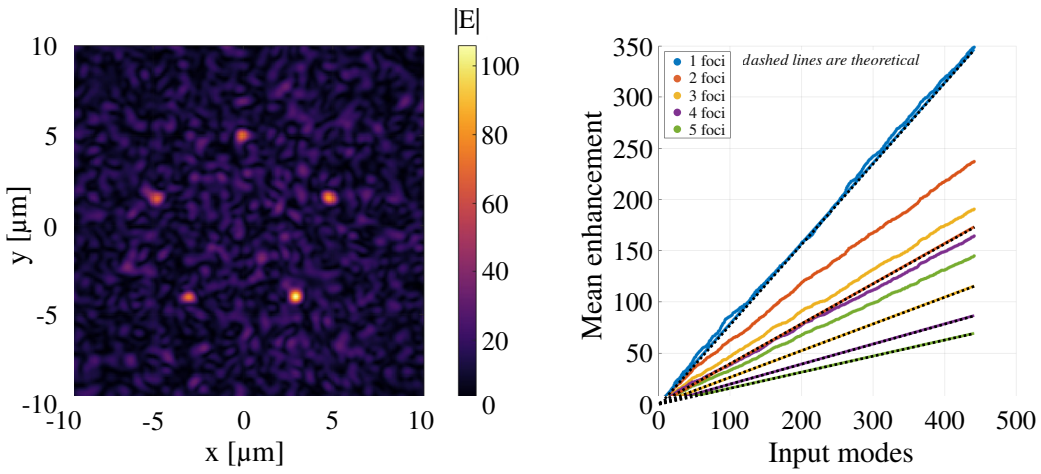

Figure 5.9: Left: Full-phase modulation is used to generate five foci simultaneously in a plane 20 µm behind the titanium dioxide scattering layer. Right: The mean enhancement of 1-5 simultaneous foci against the number of input modes. Theoretical values are calculated using Equation 5.2 and dividing by the number of simultaneous foci.

As shown in Figure 5.9, the model is capable of simulating the generation of multiple foci. Moreover, the enhancement remains linear as a function of the number of input modes. Additionally, the enhancement of a given focus decreases as light is shaped into an increasing number of foci simultaneously. However, the measured mean enhancement values were consistently higher than those predicted by the standard N/M theory.

To understand this, it is helpful to discuss the physical mechanisms of using full-phase modulation to shape light as it passes through a scattering layer. Each input mode has its phase adjusted independently, while its amplitude remains fixed. For any target region, the maximum possible contribution to the enhancement of a given input mode is deterministically defined by linear scattering of that input mode through the medium. However, because the phase can be arbitrarily modulated, the contributions of each mode to a particular target can be brought into perfect constructive interference, maximising the total field magnitude at the focus.

To explore how this mechanism functions in the case of multiple simultaneous foci, Figure 5.10 was generated, which analyses the individual contribution of each input mode to two foci located at x = -5 μm (focus A) and x = 5 μm (focus B) in the same transverse plane as Figure 5.9.

As shown in Figure 5.10, light has been simultaneously focused into the two foci. Panel a) shows the optimised phase mask, while panel b) shows the resulting electric field magnitude. Panels c) and e) display the mode-specific contributions (in terms of electric field magnitude) to the left and right focus, respectively, and panels d) and f) show the associated histograms.

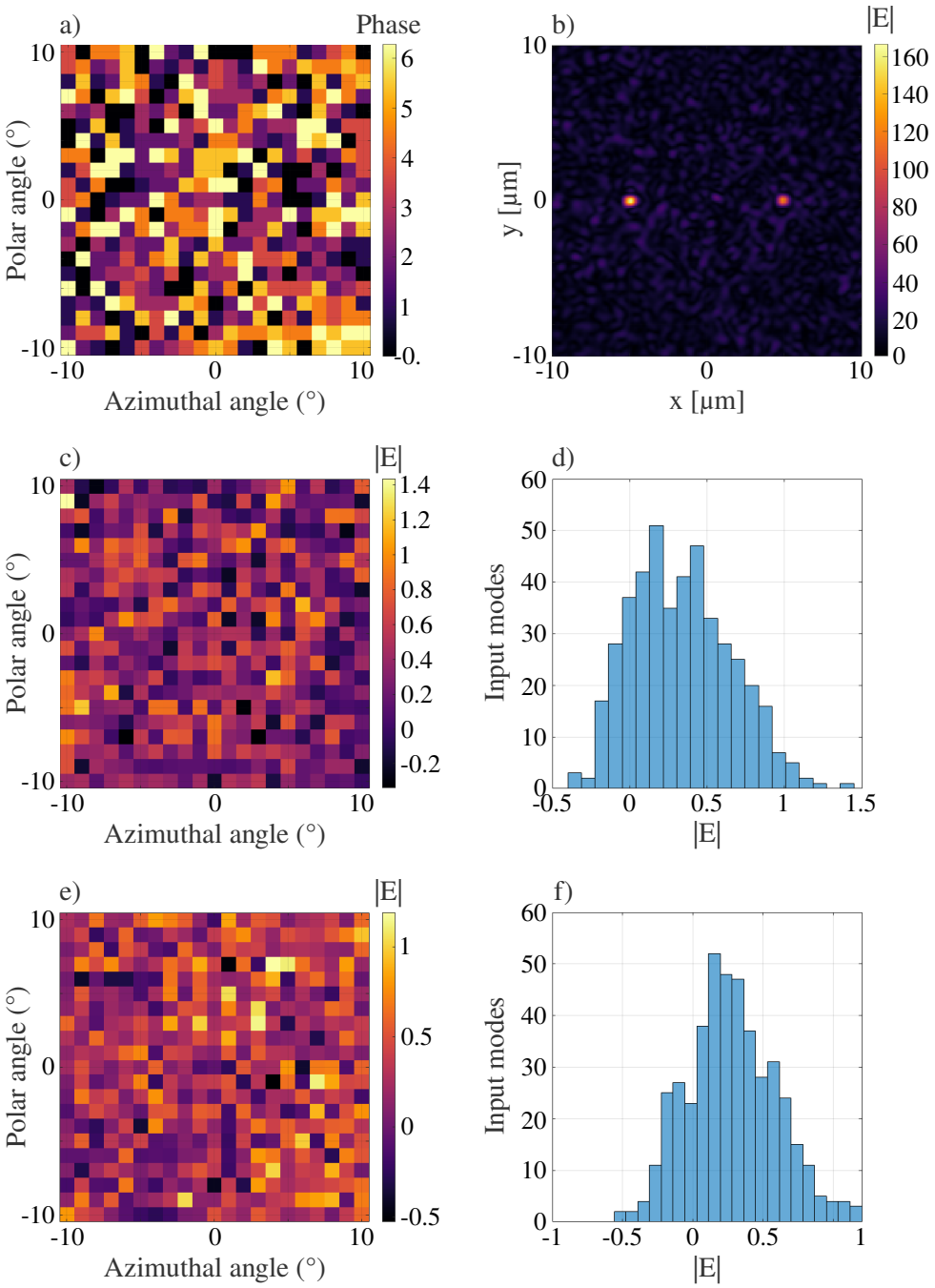

Figure 5.10: Measuring the contributions of individual input modes to each focus in a simulation of WFS generating two foci. a) the phase map and resulting field b) produced by optimising the scattered light to generate two foci at y = 0, and x = -5 and 5 µm. c) and e) show the relative contribution in terms of the magnitude of the electric field for each 441 modes to the left and right foci, respectively. d) and f) are the associated histograms of contributions to the field for each focus.

From this analysis, it was found that each input mode falls into one of three contribution scenarios:

1. the mode constructively contributes to focus A and destructively to focus B

2. the mode constructively contributes to focus B and destructively to focus A

3. the mode constructively contributes to both foci

Crucially, it was never observed that a given mode degraded both foci simultaneously. This is expected: since phase is modulated between $0-2\pi$, any mode that is initially out of phase with both targets can always be adjusted to enhance at least one of them, and potentially, to contribute positively to both. In cases where there is a trade-off (e.g. mode X improves A but degrades B), the positive contribution to one focus always outweighs the negative contribution to the other. These results may suggest why the enhancement across all foci remained higher than the N/M theory suggests.

Understanding the theoretical distribution of input mode contributions across the three categories remains an open problem. In the absence of correlations, one would expect a uniform distribution of modes, leading to strict trade-offs and a $1/M$ scaling of enhancement. The observation that many modes contribute positively to both targets indicates a breakdown of this assumption and highlights the need for a revised statistical model that considers the physically rigorous propagation of the input modes through the medium.

This simulation framework is uniquely well-suited to explore such questions. By directly measuring the field contributions of each input mode to arbitrary target geometries, future work could quantify the overlap between different foci, measure the correlation inside the medium, and determine the limits of simultaneous focusing in realistic scattering media.

5.3.4 Future work

The simulations above showcased the key ability of the computational framework to calculate and visualise internal and external fields in highly scattering titanium dioxide layers. This framework was successfully applied to model WFS and was able to investigate relevant phenomena such as enhancement and correlations across multiple foci.

Having demonstrated the method, it could be adopted to support a range of research studies. For instance, how the characteristics of an internal foci might change with depth. Or the impact optical properties, such as anisotropy, have on focus formation. It could also involve dedicated studies constructed to guide the development of WFS schemes [35, 34, 90], correlation-based imaging methods [191, 14, 41], and other techniques involving coherent light in turbid media [90].

The method could also be extended to model a wider range of turbid media, beyond titanium dioxide phantoms. For instance, absorption could be included by using complex refractive indices. Heterogeneous materials could be represented by assembling composite models comprising different sphere suspensions. This could allow modelling layers of the skin and more complex heterogeneous tissues [192, 20], using different sphere recipes for each layer. Mixtures of sphere types could further broaden the scope. For example, certain sphere distributions have been shown to replicate wavelength-dependent scattering behaviour, such as Schmitt and Kumar's model of biological tissue that uses a lognormal distribution of sphere radii [115]. Finally, to model dynamic media, simulations could be repeated after purposeful or random translations of the spheres. This could allow studying effects such as speckle decorrelation or the deterioration of foci [102, 193].

The WFS simulations took $\sim$2 hours per plane wave on Myriad running CELES, around twice as fast as the simulation running on Zeus or Mneomosyne. This simulation time scales quadratically with the number of spheres and quartically

with the truncation order, as described in Section 3.2.4. Literature suggests this can be improved to a logarithmic dependence on the number of spheres using fast multipole methods [130], such as the latest implementation of MSTM [194] or a modified version of faSTMM that allows for near-field calculation [163].

5.4 Chapter summary

This chapter applied the validated discrete-particle/T-matrix framework to model light focusing through and inside turbid media via WFS. The main contributions are as follows.

First, the angular spectrum method was coupled with the discrete-particle/T-matrix framework to generate a method of modelling input modes that most closely correlated with the experimental setup used for modelling WFS. This technique was validated through comparison with WFS enhancement theory and was found to replicate both the linear growth in focus enhancement and the ultimate theoretical enhancement. This was true for binary and full-phase modulation.

Second, the seminal WFS experiment of Vellekoop and Mosk was replicated *in silico*. A titanium dioxide phantom was constructed that replicated the experimental phantom's optical properties. Using full-phase control, the predicted enhancement agreed with theory. The model also generated and visualised foci inside the medium, demonstrating capabilities that are challenging experimentally.

Third, the framework was extended from single-focus control to multiple foci and extended targets. Enhancement scaled linearly with the number of controlled input modes and decreased with the number/area of targets, while remaining higher than simple N/M predictions, implicating measurable field correlations.

Overall, this chapter establishes a practical and reusable pipeline for WFS studies: (i) generate angular-spectrum input libraries once; (ii) solve the forward fields

via T-matrix; (iii) assemble optimised foci for single or multiple targets, including internal planes; and (iv) quantify enhancement, correlations, and depth dependence. These results provide a validated foundation for subsequent work.

Chapter 6

Modelling light propagation and focusing in tissue

The previous chapter demonstrated how WFS could be modelled through highly scattering titanium dioxide phantoms and validated against theory. These demonstrations established that the computational framework reliably reproduces expected enhancement scaling, generates optical foci both through and inside turbid layers, and extends naturally to multiple simultaneous targets. Having verified the method in highly-scattering layers, attention now turns to its primary application: modelling light propagation and focusing in biological tissue.

Biological tissue presents a fundamentally more complex scattering environment than replica phantoms. Its optical properties vary across scales, combining high scattering coefficients, extremely strong forward anisotropy, and structural heterogeneity. These characteristics limit the depth of penetration of coherent light and degrade the contrast of conventional imaging and therapeutic modalities. Yet, the deterministic nature of scattering ensures that WFS can (in principle) restore coherence and improve energy delivery at depth. A rigorous computational model offers the ability to study these effects *in silico*, providing insights that are difficult to obtain experimentally, particularly inside living tissue where direct access to the scattered light field is not possible.

This chapter, therefore, extends the discrete-particle/T-matrix framework to tissue-like domains. First, discrete particle "recipes" are selected to reproduce reported optical properties of soft tissue, allowing the construction of large-scale domains with realistic scattering behaviour. Next, light propagation is simulated through these domains to analyse speckle formation. Building on this foundation, WFS is modelled to generate foci through thin and deep layers of tissue, both using direct angular spectrum control and a new random-domain approach designed to remove medium-specific correlations. Finally, the framework is applied to explore photoacoustic wavefront shaping (PAWS), where photoacoustic signals act as an internal guidestar for focus generation.

Together, these studies provide preliminary but essential demonstrations of how the framework can be applied to model light focusing in realistic biological tissue. In doing so, they highlight both the potential benefits of computational WFS for biomedical optics and the challenges that must be addressed to translate such methods into practical applications.

6.1 Designing a tissue-like medium

To simulate light propagation through biological tissue, a discrete particle domain was constructed with generic *"tissue-like"* optical properties. Recall from Section 4.1.1 that Jacques' model [176] was used to determine the scattering coefficient and anisotropy of a generic tissue at a wavelength of 633 nm. These optical properties are defined as a scattering coefficient of $15.6mm^{-1}$ and an anisotropy of 0.9. The discrete particle database created in Section 4.4.1 was searched to find consistent sphere *"recipes"* that produce discrete particle *"candidate"* domains with these target properties. Multiple viable candidate domains are identified and have been plotted in Figure 4.11. The method described in Section 4.4.1 was used to select the optimal domain, defined as being the most efficient when coupled with the T-matrix method.

Briefly, a 100 μm^3 sample volume is constructed, such that the total number of spheres can be determined from Equation 4.15. The truncation order is determined using Wiscombe's criterion (Equation 4.16). These values are applied to Equation 3.19 to determine the number of equations that need to be solved using the T-matrix method. The most efficient domain has been determined as the one with the lowest number of linear equations, and is shown in Figure 4.11 by the black diamond. This domain is constructed from spheres with a radius of 1.72 μm, a refractive index of 1.60, and a density of 0.77% by volume for a wavelength of 633 nm.

6.2 Propagating light through a tissue-like medium

To demonstrate how the computational framework can simulate light propagation through large-scale *"tissue-like"* media, a focused beam is simulated propagating through an 800 μm deep discrete particle instance of the optimised recipe. This large-scale medium was created by pseudorandomly positioning spheres throughout a 100x100x800 μm volume. A Gaussian beam with a full width at half maximum (FWHM) of 20 μm was simulated propagating through this medium using CELES. To visualise the resulting scattered light distribution, the field magnitude was calculated in an axial plane bisecting the medium and plotted in Figure 6.1a.

As expected, the electric field magnitude has an initially Gaussian profile, which quickly breaks up upon entering the tissue, and is replaced by a streaky, seemingly random-looking interference pattern. This pattern evolves as the depth increases, becoming more diffuse and less intense - consistent with light propagation through a scattering medium. Beyond a depth of about 600 μm, the field magnitude is so low that it is difficult to visualise on a non-logarithmic scale plot.

To further visualise the transverse attenuation of the field, the electric field magnitude was calculated across a series of 100xμm^2 transverse slices. These slices were taken every 200 μm, at the locations depicted by the white dashed line on Figure 6.1a, and are plotted in Figures 6.1b-f.

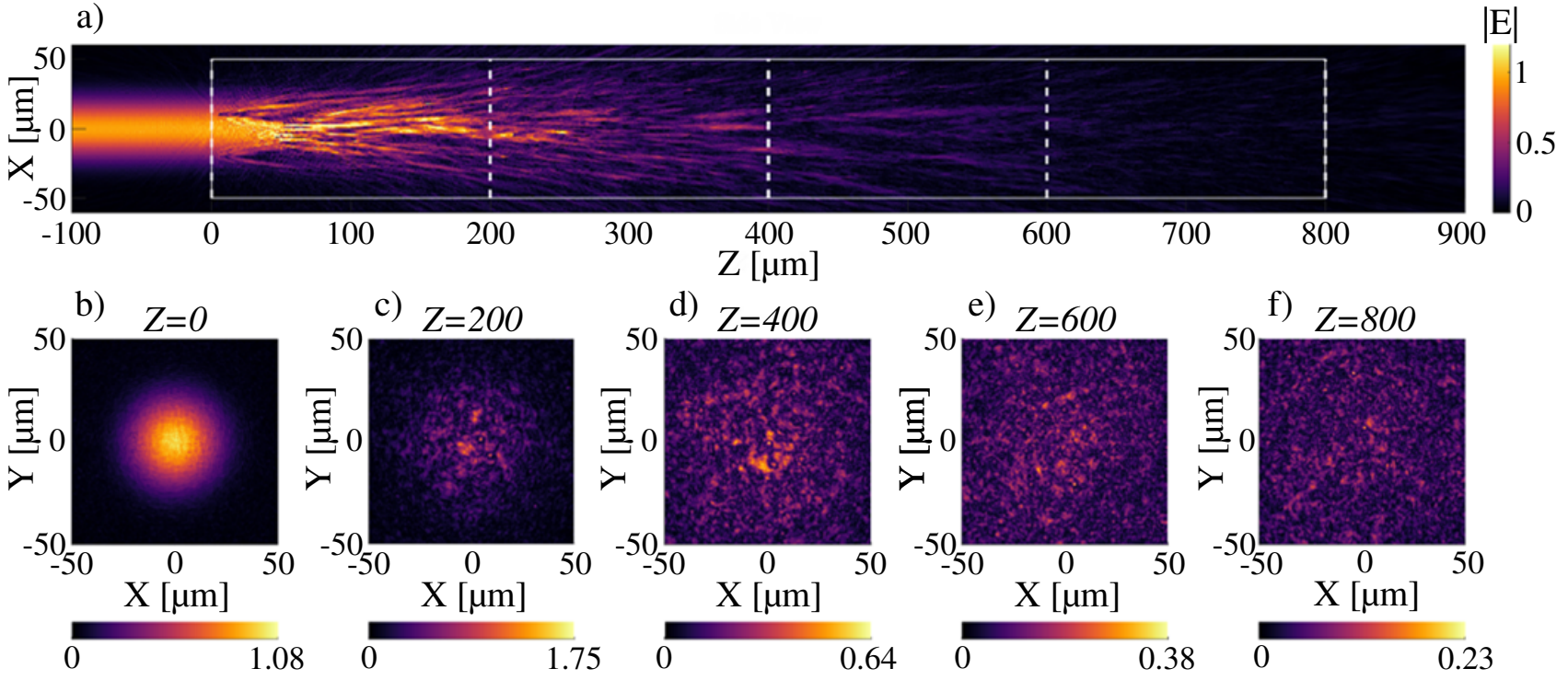

Figure 6.1: Simulation of light transmission through a 800 µm deep tissue-like medium. The plots show 2D axial (a) transverse (b-f) field profiles through the 3D light field formed in an 800 µm thick virtual tissue section. The incident light was a Gaussian beam (20 µm FWHM, λ = 633 nm, travelling left-to-right). The boundaries of the tissue section are shown by the solid white lines. The locations of the transverse planes are shown by the dashed white lines.

As expected, at $z = 0$ μm at the front face of the tissue-like medium (Figure 6.1b), there is a clear Gaussian profile to the light field, with only minor perturbations caused by backscattering. As the depth evolves through to $z = 800$μm, the Gaussian profile is degraded, and a speckle pattern begins to develop.

By demonstrating the simulation of light propagation through $\sim$1 mm of tissue-like material, this simulation demonstrates that the discrete-particle/T-matrix framework would be useful to the field of biomedical optics. For example, it would be useful to investigate how a propagating light field evolves as it propagates through tissue (or, at least, a tissue-like analogue).

6.2.1 Speckle analysis

The transverse field profiles shown in Figures 6.1b–f make clear that the incident Gaussian beam rapidly degrades into a random interference pattern as it propagates through the tissue-like medium. To demonstrate how the proposed computational framework can be used to investigate the nature of light propagation through biological tissue, the statistics of the emerging speckle are analysed as a function of depth. Three complementary measures were used to quantify speckle formation: contrast, size, and amplitude distribution.

6.2.1.1 Speckle contrast

The first measure is the speckle contrast K, defined as the ratio of the standard deviation of the intensity to its mean [167]:

$$K = \frac{\sigma_I}{\langle I \rangle}. \tag{6.1}$$

For a fully developed speckle pattern, theory predicts $K \approx 1$ [167]. Different values arise when residual deterministic structure remains, for example, from the incident beam envelope. Tracking K as a function of depth, therefore, provides a simple indicator of how rapidly the light field evolves toward random statistics.

6.2.1.2 Speckle size

A second measure is the characteristic speckle size, which reflects the transverse spatial scale of the interference. This was obtained from the spatial autocorrelation of the field magnitude $|E(x,y)|$,

$$C(\Delta x, \Delta y) = \frac{\mathscr{F}^{-1}\{|\mathscr{F}\{|E(x,y)|\}|^2\}}{C(0,0)}, \tag{6.2}$$

where $\mathscr{F}$ denotes the Fourier transform. Radial averaging of $C(\Delta x, \Delta y)$ yields a one-dimensional profile $C(r)$ from which the full width at half maximum (FWHM) is extracted. Physically, this FWHM corresponds to the average grain size of the speckle pattern, which sets the spatial resolution limit for imaging through the medium. Calculation of the spatial autocorrelation and curve fitting was performed using Marco Leonetti's *Speckle Autocorrelation* MATLAB toolbox [195].

6.2.1.3 Amplitude distribution

Finally, the distribution of field magnitudes was examined. In the limit of fully developed speckle, the envelope $|E|$ is Rayleigh-distributed:

$$p(|E|) = \frac{|E|}{\sigma^2} \exp\left(-\frac{|E|^2}{2\sigma^2}\right), \tag{6.3}$$

With σ determined by the mean squared field. To assess convergence toward this limit, histograms of $|E|$ at different depths were compared to Rayleigh fits, and the goodness of fit was quantified using the coefficient of determination R^2. Increasing R^2 indicates that the statistics of the simulated speckle are approaching those predicted by theory.

6.2.1.4 Results

Results are shown in Figure 6.2. The top row shows the raw speckle patterns at selected depths, the middle row their autocorrelation functions, and the bottom row the amplitude histograms with Rayleigh fits. Field magnitudes have been normalised for each depth, as the absolute values are less important in this visualisation than the developing speckle (compared to Figures 6.1b–f with individual colourbars).

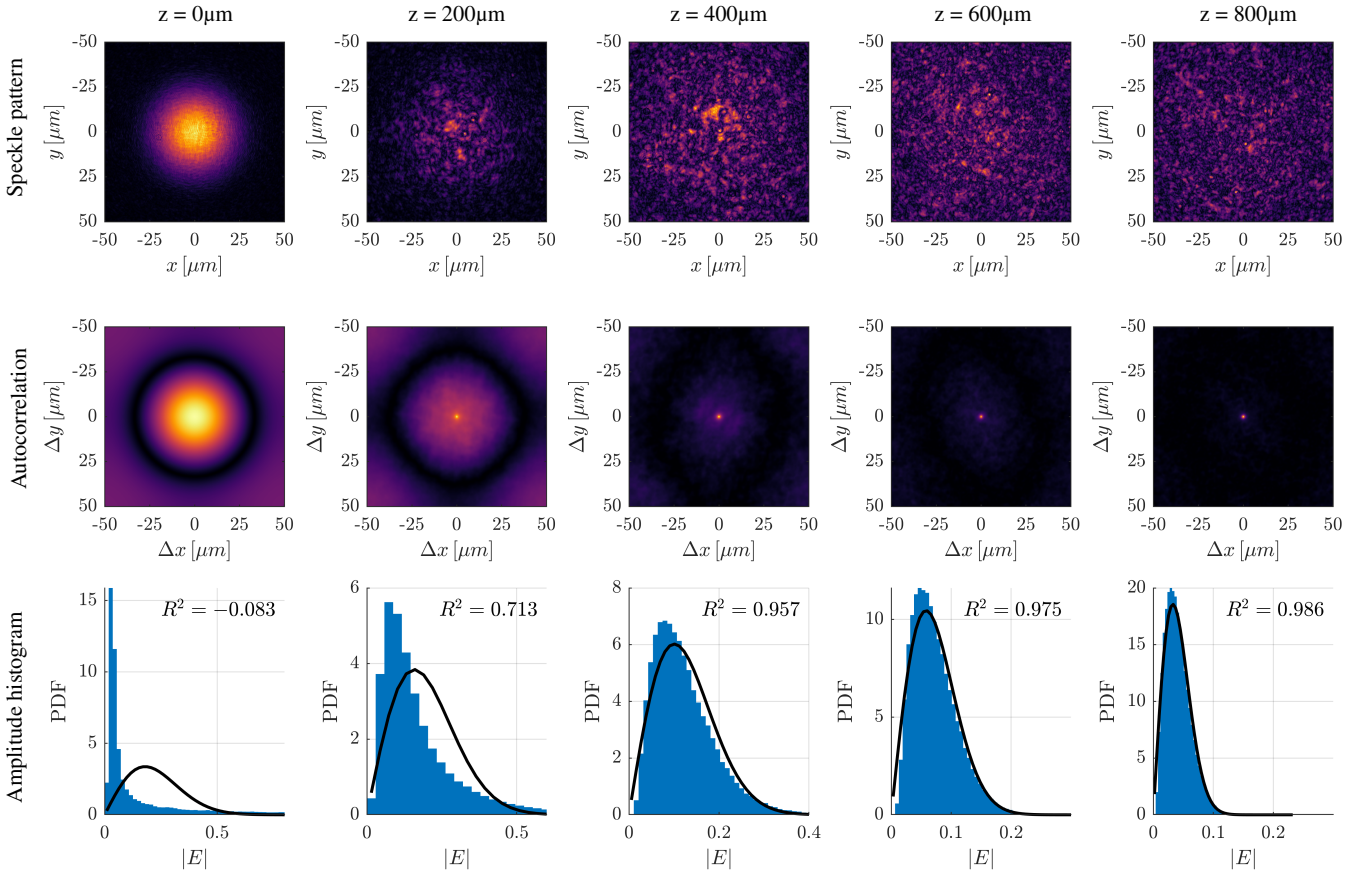

Figure 6.2: Speckle analysis at selected depths inside the simulated tissue-like domain ($z = 0, 200, 400, 600, 800$ µm). Each column corresponds to one depth plane. Top row: amplitude speckle patterns in the near-field, displayed over a 100×100 µm^2 region. Middle row: corresponding spatial autocorrelation functions, showing the characteristic speckle size and structure. Bottom row: histograms of the speckle amplitude distributions with Rayleigh distribution fits; the coefficient of determination (R^2) indicates goodness-of-fit and provides a measure of convergence toward a fully developed speckle pattern.

Looking at the field profiles in the top row of Figure 6.2, it is clear that the residual Gaussian envelope is degraded as a function of depth. The field itself appears to become more random and "speckly". This is supported by looking at the second row - at shallower depths, there is a Gaussian profile clearly present in the autocorrelation plane. As light propagates deeper into the tissue-like medium, this Gaussian component is suppressed, leaving behind a single bright central spot. The width of this spot defines the average speckle grain size. In other words, the disappearance of the extended Gaussian envelope and the persistence of only the central peak are indicators that the field statistics have converged toward those of fully developed speckle. Further evidence is shown in the final row, which shows a histogram of the amplitudes across each plane fitted with a Rayleigh curve. The R^2 error decreases as a function of depth, indicating an improved fit with the data and suggesting, once again, the speckle is becoming fully developed.

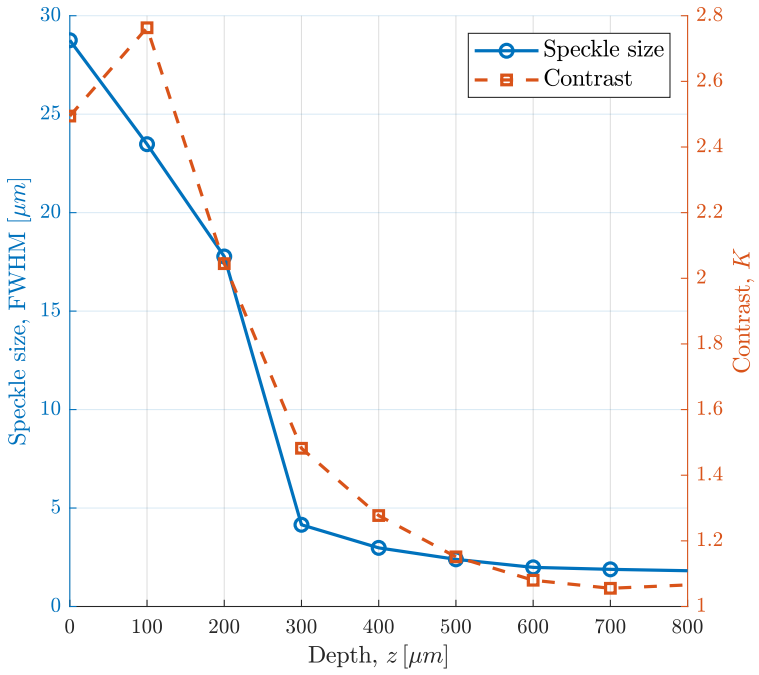

Figure 6.3: Evolution of speckle size and speckle contrast with propagation depth inside the simulated tissue. The speckle size is quantified using the FWHM of the autocorrelation function, while the speckle contrast K is defined as the ratio of the standard deviation to the mean of the intensity distribution. Both metrics are plotted as functions of depth, illustrating the convergence of speckle statistics as multiple scattering develops.

Further quantitative trends are shown in Figure 6.3, where both speckle contrast and speckle size are plotted as a function of depth. The results demonstrate convergence toward stationary speckle statistics inside the tissue-like medium, consistent with theoretical expectations. In particular, the speckle contrast approaches unity, as predicted for fully developed speckle, while the speckle size converges toward an approximately constant value. The speckle size in the near-field is determined by the underlying structure of the medium, the wavelength of the incident light, and the numerical aperture (NA) of the scattered light field. In the current simulations, the relatively narrow computational domain restricts the effective NA, which may artificially broaden the speckle grains and lead to slightly overestimated speckle sizes.

This demonstration is significant because quantifying speckle statistics within bulk tissue is effectively impossible *in vivo*, where only indirect measures of the light field are available. By contrast, the presented simulation framework provides direct access to the internal speckle field, allowing its convergence and statistical properties to be examined in detail. Further work will be required to assess the generalisability of these results. In particular, it remains to be seen whether discrete-particle representations fully capture the statistical behaviour of real tissue, and how factors such as domain width and NA affect the measured speckle size. Nevertheless, these results show that the model reproduces the expected evolution from structured beam profiles at the tissue boundary to fully developed speckle deep inside the medium, thereby providing a useful platform for investigating light transport in tissue-like media.

6.3 Focusing inside a thin tissue-like layer

Initially, a small-scale simulation of WFS being used to focus light into a tissue-like medium was simulated. To this end, the recipe defined above was used to populate a $200\mu m^3$ volume with scattering spheres. A target is defined at the origin of this medium.

As in Chapter 5, a stepwise sequential algorithm is used to optimise the incident input modes to shape light into the medium. However, this time, binary amplitude modulation is used to optimise the input mode plane wave angular spectrum. This was done for demonstration purposes, as previous shaping procedures all relied on some form of phase modulation. Binary amplitude modulation differs in that the phase of each input mode is not modulated. Rather, the scattered field associated with the reference input mode (the normally incident plane wave) is summed with the scattered fields associated with each of the other input modes sequentially. If the sum of the two complex fields increases the electric field magnitude at the target, then the input mode responsible for the increased enhancement is recorded. The superposition of the scattered fields of each of the reinforcing input modes then creates an optical focus, as shown in Figure 6.4

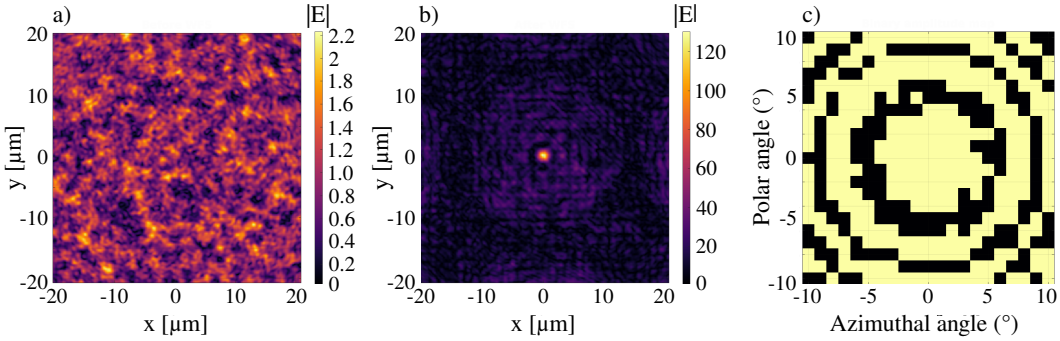

Figure 6.4: Simulation of focusing 100 μm inside a tissue-like layer via WFS. The incident input modes are optimised to shape light into a 200x200x200 μm^3 volume with a scattering coefficient 15.6mm^{-1} and an anisotropy of 0.9. a) and b) depict the magnitude of the electric field across a 40x40 μm^2 transverse plane located at the origin. a) shows the field magnitude resulting from an incident plane wave, and b) shows the optimised scattered field, with an optical focus present. c) shows the binary amplitude map applied to the 441 input modes used to generate the focus.

Figure 6.4a shows the electric field magnitude across a transverse plane located at the origin, after light has propagated 100 μm through the tissue-like medium. The profile of the electric field magnitude across this plane appears uneven and craggy, almost fractal. There are bright spots and dark spots present uniformly throughout the field, in a seemingly random arrangement. Compared to the fully developed speckle patterns seen in Figure 5.5 for a titanium dioxide domain, the tissue-like

scattered field does not vary smoothly, and the field magnitude never fully drops to zero, characteristic of a not fully developed speckle pattern [167]. This observation is consistent with the TMFP of each domain. Recall that the depth of the titanium dioxide domain is 10 μwith a TMFP of ~ 5 μm. Meanwhile, the light field in Figure 6.4a has been generated at a depth of 100 μm, where the TMFP of the tissue-like medium can be calculated to be $\frac{1}{\mu_s(1-g)} = 640$ μm.

Nevertheless, light was focused into a target region at the origin of this tissue-like medium using binary amplitude modulation. The resultant optical focus and associated binary amplitude map are shown in Figures 6.4b and c, respectively. The confinement of the optical focus is much poorer relative to the highly scattering titanium dioxide focus seen in Figure 5.4. The reason for this becomes apparent when looking at the binary amplitude map. There are clear correlations in the amplitude modulation, which has a concentric ring profile, albeit with slight aberrations. This is, once again, a consequence of the weak scattering. At a depth of 100 μm, it is more appropriate to consider this tissue-like simulation a demonstration of adaptive optics and aberration correction rather than true WFS. From this, we can conclude that simulations of at least a TMFP are needed to simulate proper WFS in tissue.

6.4 Focusing inside deep tissue

6.4.1 Constructing a deep tissue medium

To meet the requirement of modelling WFS, light must be simulated propagating through at least a TMFP of tissue, determined to be 640 μm for the generic tissue formulated in 4.2.1. As such, an 800x100x100 μm^3 volume was populated with spheres using the optimised recipe from Section 6.1. This domain is extremely narrow, resulting in two consequences. Firstly, light from a propagating plane wave would be likely to escape from the sides of the simulation. This was apparent even without employing the Monte Carlo method for optimising domain width discussed in Section 4.4.2. Secondly, plane wave input modes at a more oblique incident angle in the angular spectrum decomposition would be incident on the side of the

medium. As such, a new method of modelling input modes had to be formulated.

6.4.2 Modelling input modes

The second approach for modelling input modes was termed the random medium method. In this method, the incident field is fixed, and the scattering medium is randomly regenerated - such that each input mode corresponds to the same incident light propagating through a unique pseudorandom instance of the medium. Each medium instance is designed using Mie theory to have the same macroscale scattering behaviour (scattering coefficient and anisotropy). However, the microscale placement of refractive index inhomogeneities (constituent spheres) is randomised. A diagram depicting the method and its differences with angular spectrum modelling is shown in Figure 6.5.

This method represents an alternative way of modelling input modes. In general, it is a less physically accurate representation of an experimental WFS setup, as *in vivo* WFS would use a fixed medium and a planar SLM or DMD for spatial modulation. The closed physical analogue would be a hypothetical tomographic WFS array, where each input mode propagates along an independent path to the target.

However, the model does have some key advantages. First, like the angular spectrum approach, each input mode is independent and can be simulated in parallel, even across different machines.

Furthermore, random medium modelling enables simulating geometries incompatible with an angular spectrum decomposition. For example, narrow discrete particle domains would not be compatible with a wide angular spectrum - at the larger incident angles, light would be directly incident on the sides of the medium. Conversely, the random medium method can model input modes using a narrow Gaussian beam propagating along the long axis of the medium, minimising light escaping from the sides of the simulation.

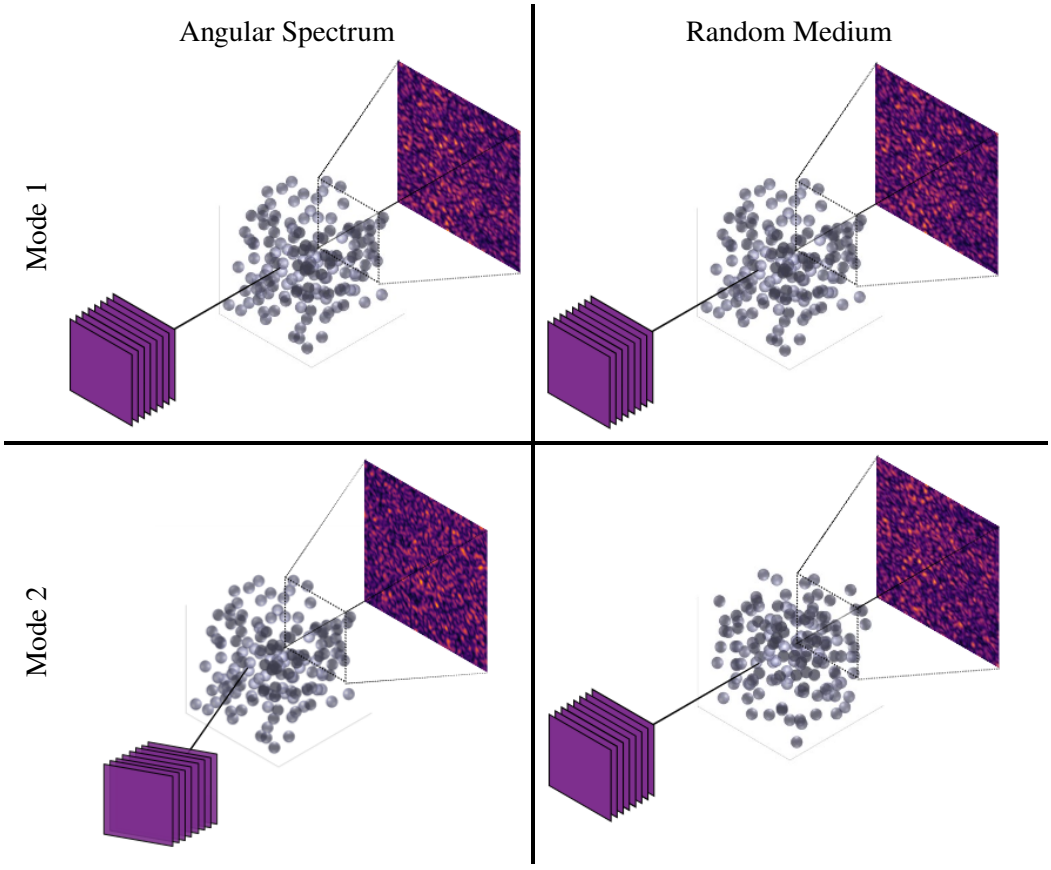

Figure 6.5: Schematic illustration of the two methods used to model input modes in WFS simulations. Left column: In the angular spectrum approach, each input mode corresponds to a plane wave incident at a different angle, all propagating through the same discrete particle medium. Right column: In the random medium approach, each input mode corresponds to light propagating through a different stochastic instance of the medium.

Another key property is that the random medium method removes medium-specific correlations. Angular spectrum input modes modelling uses a fixed medium, and as such, WFS behaviour might be disproportionately affected by the placement of specific spheres. For example, a dense cluster of spheres close to the target region may affect focus generation. Note that this behaviour is not necessarily undesirable. Biological tissue is inhomogeneous, and although it has not been thoroughly investigated, it is possible that a unique microstructure in a given medium may affect WFS and other coherent phenomena. However, the random matrix input mode approach guarantees microscale independent scattering behaviour across the input modes, isolating the impact of medium-specific effects.

6.4.3 Focusing inside deep tissue

The scenario for the simulations of focusing inside deep tissue via WFS is shown in Figure 6.6.

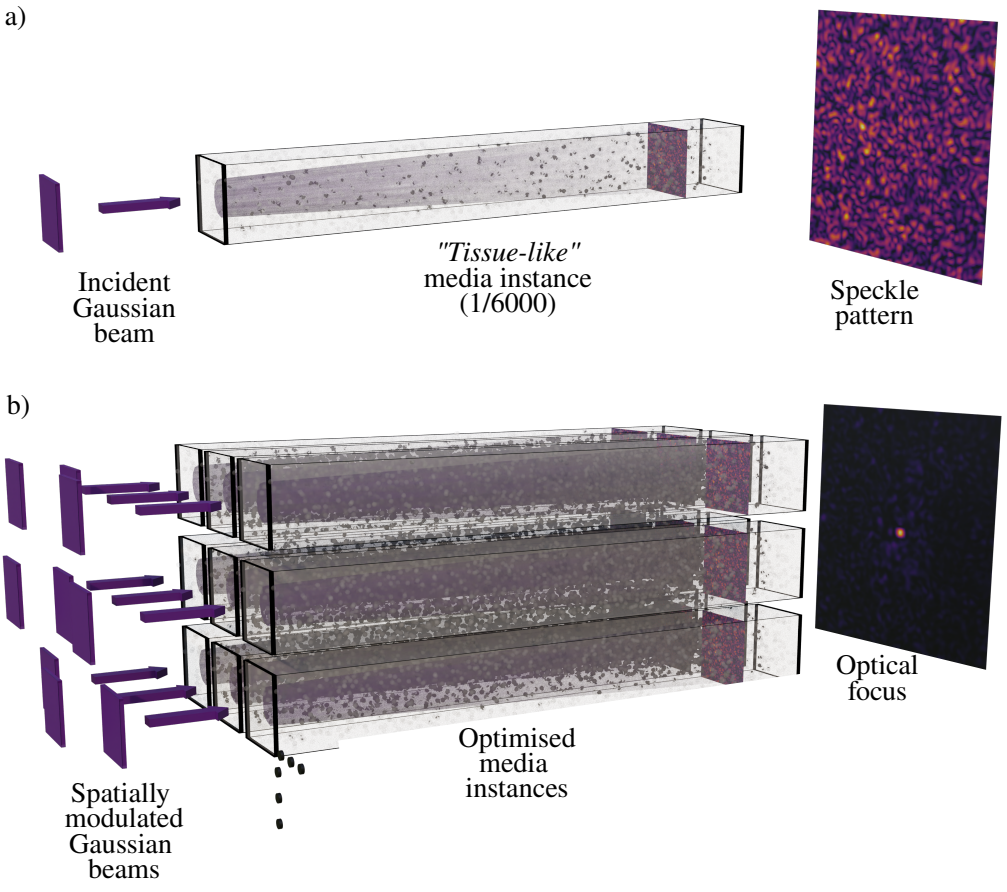

Figure 6.6: Diagram of the simulation scenario to focus light inside a tissue-like medium. a) An incident Gaussian beam is multiply-scattered, resulting in a speckle pattern forming inside the medium. b) The T-matrix method is used to simulate light through 6000 tissue-like discrete particle instances. The phase of these instances is spatially modulated such that the summation of the scattered fields interferes to produce an optical focus inside the tissue-like medium.

To summarise, a Gaussian beam incident on a tissue-like medium rapidly loses its initial profile and evolves into a speckle field at depth, as shown in Figure 6.6a. By regenerating thousands of statistically equivalent medium instances, each with identical macroscopic scattering properties but different microscale structure, these speckle fields can be treated as independent input modes. WFS is then modelled by applying phase modulation across these input modes, and constructive interference

at the target plane produces a bright, speckle-sized focus deep inside the medium, as shown in Figure 6.6b.

In total, 6000 unique discrete particle instances are simulated, corresponding to 6000 input modes used to generate an optical focus. Therefore, the first stage is to simulate the propagation of the first input mode. A Gaussian beam with a full width at half maximum (FWHM) of 20 μm was simulated propagating through the 800x100x100 μm using CELES running on Myriad. A 2D transverse cross-section of the scattered electric field magnitude is calculated and plotted in Figure 6.7a.

As expected, due to the scattering, the initially Gaussian beam is spread out and aberrated, and the magnitude of the field decreases as the beam propagates deeper into the medium. After 800 μm of scattering, the magnitude is too weak to visualise easily without a logarithmic scale.

The magnitude of the electric field across the 30 μm^2 transverse plane located 725 μm inside the medium (delineated by the dashed white line) is shown in Figure 6.7b. As expected, there exists a seemingly random speckle pattern across the field. There are bright spots and dark spots across the field, and the magnitude is uniformly lower than the light field towards the start of the medium.

The simulation was repeated 6000 times using different tissue-like instances of the medium. Fields for a select few other instances are also shown in Figure 6.7c, d and e.

A target region was defined at a location 725 μm deep in the medium (as shown by the white circle in Figure 6.7a). To shape the field, the 6000 input modes were generated as described above, and their individual input phase levels optimised using a stepwise sequential algorithm [7]. The magnitude of the resulting total field was plotted in Figure 6.7f.

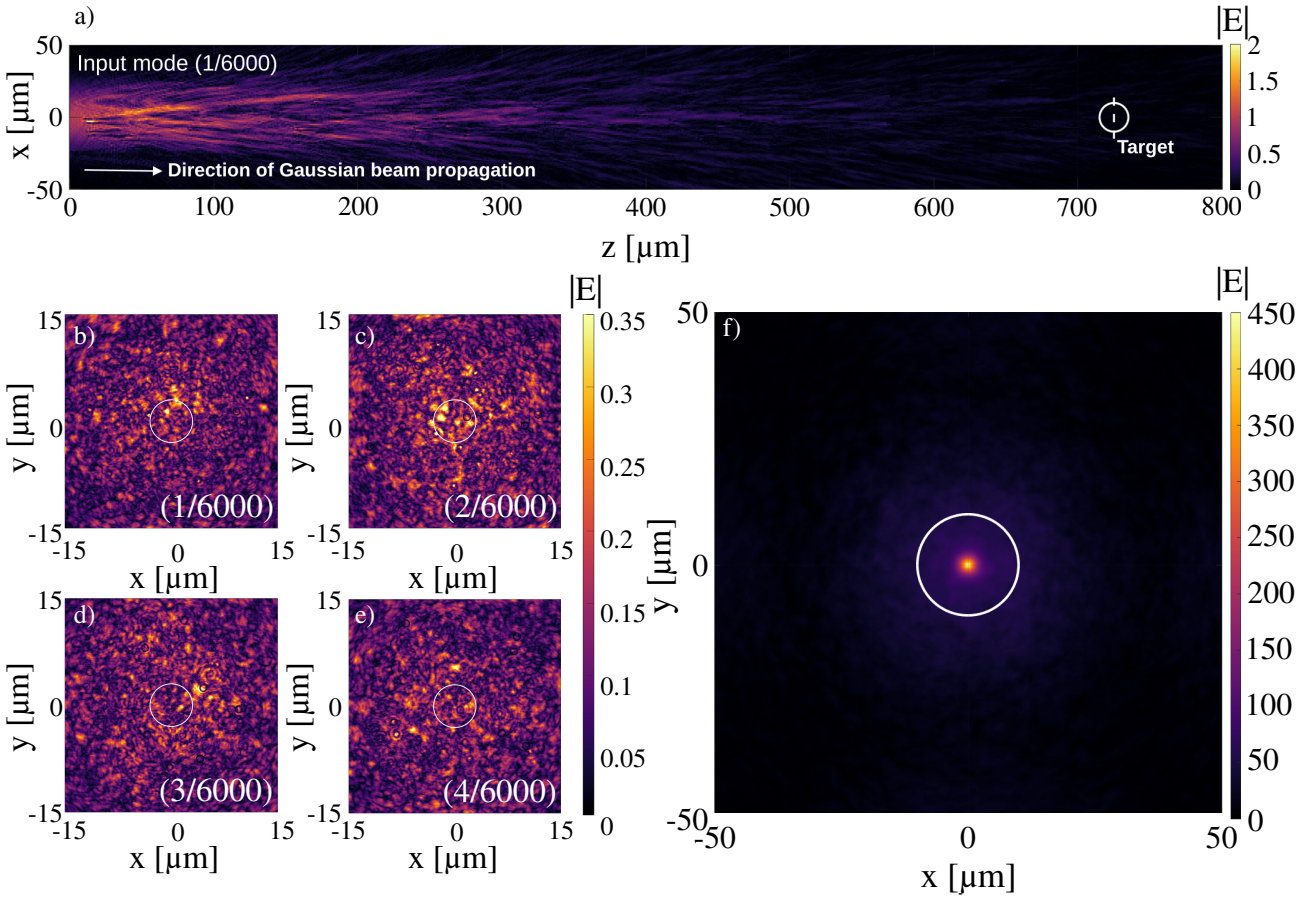

Figure 6.7: a) 2D cross-section of light propagating through the tissue-like medium. The light is incident on the left-hand side. The location of a target for focusing light via PAWS is shown by the white circle. A 30 μm^2 plane of interest at this target is shown by the dashed line, and shown in b). The same incident Gaussian beam is simulated propagating through different discrete particle instances of the same tissue-like media, and the resultant field patterns are shown across b-e for four select instances. f) shows the focus generated by optimising the phase of all 6000 input modes.

As expected, a bright focus, the size of a single speckle, is produced. The electric field magnitude of this focus is significantly higher than the magnitude of the incident Gaussian beam and the unoptimised scattered fields. The focus itself is perfectly smooth. This is a consequence of using multiple domains as input modes - effectively averaging out the aberrations observed in the individual domains.

To further characterise the generated focus, a side-view profile of the optical focus shown in Figure 6.7f is shown in Figure 6.8 (corresponding to the *xz*-plane through the centre of the focal region).

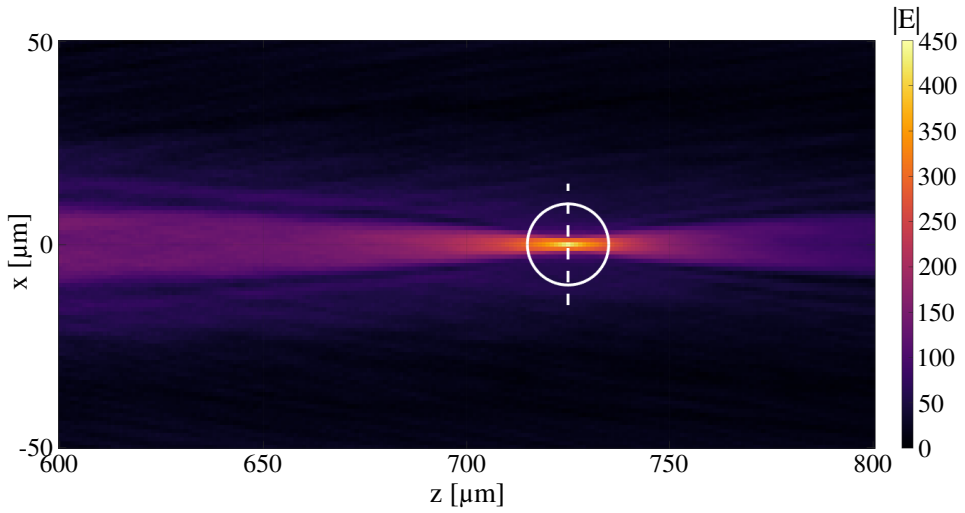

Figure 6.8: Side-view (*xz*-plane) profile of the optical intensity distribution at the focus generated via wavefront shaping using 6000 input modes. The focal region is smooth and symmetric, in contrast to the irregular foci observed in previous titanium dioxide simulations. This smoothness arises due to the averaging over multiple uncorrelated input modes derived from independent realisations of the scattering medium.

The profile reveals that the focus varies smoothly in both axial and transverse directions, exhibiting a symmetric envelope about the *z*-axis. This behaviour is in contrast to previous visualisations of the focused light field for a titanium dioxide medium generated using angular spectrum modelling of the input modes (see Figure 5.4). The titanium dioxide field displayed strong aberrations and no symmetry. In this earlier simulation, input modes were defined using an angular spectrum across a single instance of the medium.

In the present model, however, each input mode is essentially a distinct random instance of the scattering medium. As such, the contributions from medium-specific correlations are ultimately averaged out.

6.5 Modelling photoacoustic wavefront shaping

6.5.1 Motivation

Modelling PAWS was chosen as a final demonstration of the computational framework because it exemplifies both the strengths and intended applications of the method. *In silico* modelling of PAWS is challenging in that it requires accurate modelling of coherent light propagation deep inside tissue, while being efficient enough to model enough input modes to overcome the N/M limitations inherent to acoustically contained focuses. Experimental investigation of PAWS is challenging as it is inherently an indirect, guidestar-assisted method of focusing light. These difficulties are further exacerbated by acoustic, thermal and tissue motion challenges.

By applying the discrete-particle/T-matrix framework to PAWS, this section illustrates not only that the model can reproduce known theoretical scaling but also that it can ultimately serve as a practical testbed for probing the limits of WFS-guided biomedical techniques. In this way, PAWS provides a rigorous, physically realistic benchmark for the framework and motivates its adoption in studies of *in vivo* light control.

6.5.2 Background

Biological tissue scatters light, limiting the penetration depth of various therapeutic and diagnostic optical and NIR techniques (see Section 2.1.3). A technique that could compensate for the deleterious effects of scattering is WFS [7]. WFS involves spatially structuring the incident light field so as to control the interference patterns produced in the medium. In principle, this allows an optical focus to be generated in or through scattering media, including biological tissue. By focusing light in

tissue, WFS could enable increasing the penetration depth of a range of biomedical techniques.

The ability to focus light through a static scattering phantom is well established experimentally [7]. However, focusing inside *in vivo* tissue is significantly more challenging. This is because the light field inside a tissue cannot be directly resolved, necessitating the use of indirect measures of the underlying field distribution - so-called guidestars [35]. One possible guidestar involves meaning the PA signal - ultrasound waves generated when light is absorbed by tissue [4]. The process of using the PA signal to shape light into medium is known as PAWS [37].

Like WFS, PAWS has been experimentally demonstrated to focus light through scattering media [37, 57]. However, focusing light inside tissue using PAWS is significantly more challenging. A significant challenge is the high sensitivity and spatial resolution requirements of a PAWS system. Recall N/M theory from Section 5.1.3, where N is the number of input modes (e.g. elements on an SLM) and M is the number of output modes (e.g. speckle grains light is simultaneously focused into). When focusing light into tissue, factors such as the tissue decorrelation time will limit the number of controllable input modes. Moreover, the number of independent speckles inside a PAWS feedback signal is a function of the acoustic resolution of the detector. This reduces the signal-to-noise ratio of any PAWS feedback signal, making iterative WFS challenging.

It is currently challenging to make predictions to guide experimental design and explore the requirements of a hypothetical PAWS setup. Existing computational models are typically either too simplistic to represent the required physics (e.g., contain no deterministic phase information) or else too computationally expensive (e.g., requiring a $< \lambda/2$ discretisation of the medium) to simulate propagation through large enough volumes of tissue, and consequently be of use in investigating PAWS.

To address this challenge, the computational framework constructed in Chapters 3 and 4, and used to simulate WFS in Chapter 5, was applied to simulate the focusing of light using a PA feedback signal.

The framework was already applied to simulate the focusing of light into a single speckle grain 725 µm deep into an 800 µm thick tissue-like medium. To model PAWS, the process of focusing light was repeated using a target region of various sizes, illustrative of PAWS experiments relying on acoustically limited feedback from sensors of different spatial resolutions. By providing a simulation platform for studying PAWS, this model could pave the way to developing systems that can focus light in tissue.

6.5.3 Results

To provide a simple illustration of how the model might enable parametric studies relevant to PAWS, the process of focusing light into the tissue-like medium in Figure 6.7 was repeated with a 1 µm radial circular (rather than point-like) target region in the same plane of interest. The resulting electric field magnitude distribution across the transverse target plane was plotted in Figure 6.9.

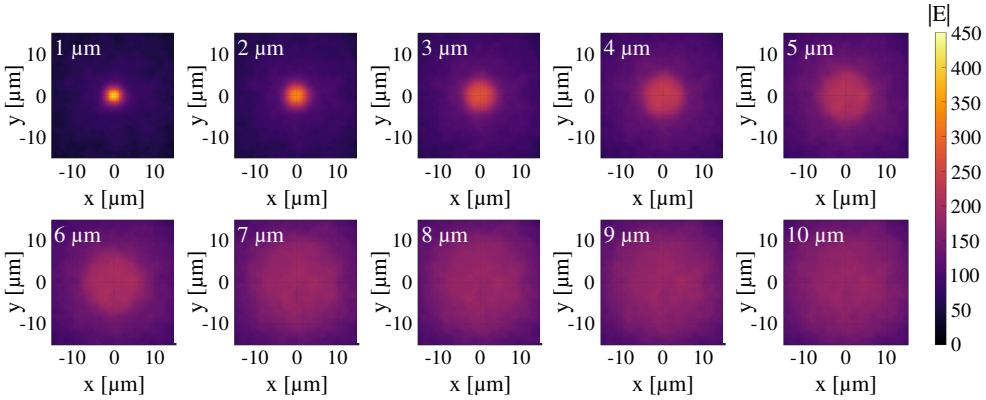

Figure 6.9: Transverse (*xy*-plane) intensity profiles of the optimised optical focus inside the tissue-like medium for target region radii ranging from 1 µm to 10 µm. Each subplot shows a 30 x30 μm^3 field of view centred on the target region. As the target region increases in size, the resulting optical focus becomes broader and less intense, consistent with theoretical expectations that increased output mode count (M) reduces focal enhancement.

As expected, a focus is formed that is larger and less intense, but still smoothly varying, owing to the averaging effect inherent to the random medium method of modelling input modes.

The above experiment was repeated using a range of target regions with different diameters, in the range 1–50 μm. The resulting focal enhancements - defined as the intensity of the optimised foci relative to the average intensity of the unoptimised speckles — were calculated and plotted in Figure 6.10.

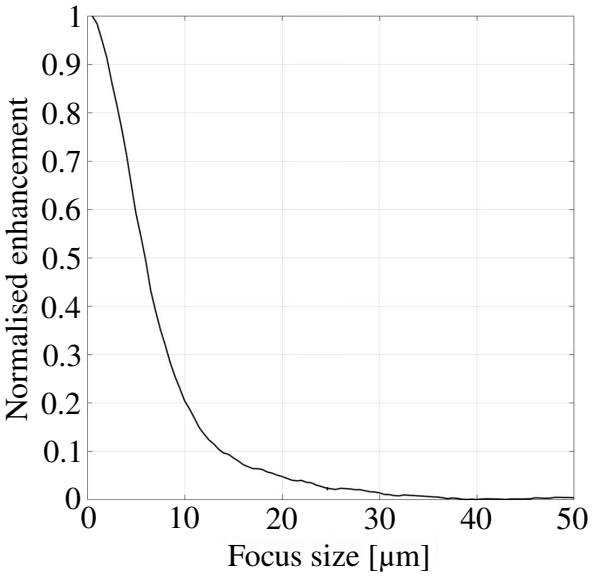

Figure 6.10: Normalised enhancement of optical foci at various target sizes.

As expected, the enhancement decreased as the size of the focal region was increased. The trend in enhancement shown in Figure 6.10 was analysed by fitting the data with a $1/r^2$ model, where r represents the radius of the target region. This model fit strongly to the data, capturing the observed reduction in enhancement as the focal area increased. The $1/r^2$ scaling arises because the number of speckle grains contributing to the target region grows proportionally to its area, i.e., πr^2. The light that is concentrated into any single speckle grain decreases as the target area expands.

6.5.4 Discussion

Throughout this thesis, a computational framework for simulating light propagation through bespoke scattering media has been developed and validated. This framework was demonstrated by modelling the focusing of light into tissue via PAWS and conducting a preliminary investigation of the method.

The computational framework has a few notable features that make it well-suited to such an investigation. As discussed in Chapter 4, the discrete particle domains have been rigorously constructed and validated, building confidence in the replication of macroscopic tissue-like optical properties *in silico*. Moreover, the T-matrix method provides an accurate, efficient and complete calculation of scattering through this medium, as shown in Chapter 3. Because a subwavelength discretisation of the domain is not required (as it is in other full-wave optical models), the method is computationally efficient in terms of time and memory. This allows it to be scaled to model tissue volumes that are large, and thus to study the focusing of light in deep tissue.

The framework was demonstrated by simulating light propagation through an 800 μm thick tissue-like scattering medium, focusing light in this medium via WFS, and performing a parametric study of the impact of spatial resolution in a simplified version of PAWS. The latter demonstrations were intended to be illustrative and were thus simplified in several ways. The main simplification was the use of random medium modelling. This method of modelling the input modes as a summation of light fields produced by multiple instances of the same tissue-like medium is inherently non-physical. A more physically rigorous approach to model WFS would involve decomposing the incident light field into an angular spectrum of plane waves incident at various angles (see Section 5.2.2). While non-physical, this approach removes the impact of medium-specific correlations such as memory effects and other confounding factors.

In the parametric PAWS study, a second simplification was related to the size of the focal zone. Specifically, although the size of this zone varied, it was always assumed to lie in a 2D plane within the medium. By contrast, in experimental PAWS systems, PA feedback signals will be confined to 3D volumes (determined by the spatial resolution of the PA sensor). Although the simulation framework developed here can be extended to evaluate the electric field magnitude within volumetric regions (see Figure 5.7), preliminary attempts to focus light into such 3D zones revealed a limitation: the number of input modes used was insufficient to generate high-contrast volumetric foci.

In vivo, several mechanisms may mitigate this scaling and enable useful focusing despite the resolution constraints of acoustic detection. Most simply, increasing the resolution of the acoustic sensor would reduce the effective focal volume. Moreover, if the speckle field inside the medium is elongated or axially symmetric (such as in the case shown in Figure 5.7 where the speckle grains are stretched along the optical axis), then fewer independent speckle grains occupy a given volume, reducing the number of input modes required to achieve a strong focus. Another relevant consideration is the hypothetical concept of photoacoustic sparsity, wherein the absorbing chromophores (see Section 2.1.2) are distributed sparsely within the medium. Even if the acoustic resolution is limited, the sparsity can allow the shaped light to be selectively guided to sub-acoustic diffraction-limited regions within the target. All of these effects rely on spatial correlations within the speckle field, and as such, necessitate the use of angular spectrum modelling of the input modes.

A final simplification in the current work was the assumption that PA signals would be generated in direct proportion to the sum of the speckle intensity within the intended focal region of interest. A more comprehensive model could be constructed by incorporating the actual response functions of ultrasonic transducers or coupling the present model to an acoustic model, such as K-wave [196], to model the acoustic aspects of PAWS.

6.6 Chapter summary

This chapter extended the discrete-particle/T-matrix framework to model light propagation and WFS in tissue-like media. The key contributions are as follows.

First, light propagation through ~ 1 mm of tissue-like material was modelled with a focused Gaussian input, revealing depth-dependent speckle formation and attenuation. The statistics of this developing speckle were analysed. These results establish that the framework can generate physically consistent internal fields in geometries relevant to biomedical optics.

Second, light was modelled focusing into a 200 μm^3 tissue-like volume using WFS. Binary-amplitude control produced a focus consistent with sub-TMFP propagation - more representative of adaptive optics. Nevertheless, modelling light propagation and focusing inside shallow, weakly scattering tissue remains of interest to certain biomedical imaging methodologies, such as OCT or aberration correction in microscopy.

Third, in deep tissue, a novel random-medium input strategy was introduced to enable focusing after one TMFP, while removing medium-specific correlations. Full-phase optimisation of 6000 uncorrelated input modes yielded a smooth, speckle-sized focus at ~ 725 μm depth, demonstrating that the framework can be used to model light focusing in deep tissues.

Fourth, the framework was applied to undertake a preliminary parametric simulation of PAWS. By varying the acoustic target size, enhancement trends were quantified and shown to decrease with increasing region radius, consistent with an approximate $1/r^2$ behaviour expected by theory.

Overall, this chapter demonstrates how the framework developed in Chapters 3 and 4 can be used for practically relevant WFS studies in biological tissue.

Chapter 7

General conclusions

Biological tissue strongly scatters visible and NIR light, resulting in a significant reduction in intensity and a loss of coherence over depth. As a result, various therapeutic and imaging modalities are constrained to image superficial tissues. One method to facilitate increased light delivery into deep tissue is WFS - a technique in which the incident light is spatially modulated to control its propagation, thereby allowing researchers to focus light at arbitrary locations inside or through tissue.

Simulating WFS in biological tissue is constrained by methods that are either too computationally intensive to model large enough volumes or too incomplete to model underlying deterministic scattering and interference processes accurately. To address the challenge, a rigorous and efficient simulation framework has been developed by coupling together a discrete-particle model of turbid media with a T-matrix method of calculating the light fields.

7.1 Summary of contributions

In Chapter 3, the first component of the framework was established - a T-matrix framework capable of simulating coherent light propagation through discrete particle media. Multiple T-matrix solvers were implemented and evaluated, identifying unreported bugs and numerical artefacts. The method was validated through comparison with Mie theory and FDTD simulation.

In Chapter 4, the second component of the framework was developed: a method for generating discrete particle domains with bespoke optical properties. This method was validated at multiple scales using IAD, Monte Carlo and angular memory effect simulations, confirming correct scattering statistics and higher-order correlations. A discrete particle database of over 25 million domains was constructed to make the future design of scattering media easier. Novel optimisation strategies were introduced to increase the computational efficiency of the framework (optimising sphere design and creating the "photons retained" metric for determining simulation width).

In Chapter 5, the angular spectrum method was coupled with the existing framework to create a method of modelling WFS that is the closest computational analogue to experimental WFS. The seminal Vellekoop and Mosk experiment was replicated *in silico*, generating foci through titanium dioxide layers with enhancements consistent with theory. This demonstration was extended to focus light into the medium, explore various strategies for shaping the incident wavefront, and generate multiple foci. A preliminary investigation of foci correlations was undertaken.

In Chapter 6, the framework was applied to focus light inside tissue-like domains via WFS. Depth-dependent speckle formation was simulated in $\sim$1 mm deep-tissue media and statistically analysed. A random-medium method of modelling input modes was introduced to remove medium-specific correlations. This method was used to achieve deep-tissue focusing ($\sim$725 μm, $\sim$1 TMFP). Consequently, a preliminary parametric study of PAWS was performed, showing enhancement trends scale inversely with target region size. These studies established the feasibility of computationally exploring WFS inside biological tissue.

7.2 Future directions

Improved discrete particle domains

The current discrete particle domains use monodisperse spherical scatterers with fixed refractive indices. While this enables scattering media with target optical properties to be designed via Mie theory, biological tissues are inherently more complex. Future work could expand the domain generation process to incorporate polydisperse size distributions [115], irregularly shaped particles, and multilayered or anisotropic configurations. Additionally, incorporating motion (e.g., Brownian motion or blood flow) would enable simulation of dynamic decorrelation phenomena and the investigation of WFS in biological tissue.

Wavefront shaping with *in vivo* constraints

To bridge the gap between *in silico* modelling and *in vivo* reality, future simulations should incorporate experimental constraints. These include more accurate SLM modelling by considering pixel cross-talk, dead zones, and realistic modulation speeds. Likewise, detector characteristics such as dynamic range and signal-to-noise ratio could be modelled, as has been done in other simulations of WFS [102]. By embedding these constraints, simulated performance metrics can be more directly compared with experimental results and used to guide hardware design.

Digital optical phase conjugation

While this thesis focused primarily on feedback-based shaping, future work could simulate DOPC, a powerful alternative strategy based on time reversal. Simulating DOPC requires calculating the backward propagation of the conjugated scattered field and evaluating how well the conjugated wave reconstructs a focus within the domain. This requires being able to represent the complex incident field in VSWF, something known as defining the beam shape coefficients of the field. This has been implemented in some generalised Lorenz-Mie theory codes like Absphere [169], but has not yet been integrated with the T-matrix method.

Evaluation of shaping algorithms

The framework developed here could be used to benchmark different WFS algorithms. Iterative approaches (e.g., stepwise sequential, partition-based, genetic algorithms), transmission matrix inversion, and model-based or machine learning methods could be compared in terms of convergence speed, robustness to noise, and focus enhancement. Existing computational attempts to quantify algorithm performance used non-physical modes of light propagation [51], which would struggle to model the newer deep-learning-based shaping algorithms.

Multi-target focus generation

Simulations presented in this thesis primarily targeted single optical foci. Future work should extend the preliminary work presented in this thesis, investigating the generation of multiple simultaneous foci. Statistical correlations between input phase maps and output intensity patterns for multi-target shaping can be quantified, potentially enabling new methods of shaping light into multi-target foci.

Measuring the angular memory effect in tissue-like media

The AME and related correlations offer a pathway to rapid scanning and focus translation. Future work should systematically investigate how the AME range varies as a function of domain optical properties. Attempts to simulate the AME using non-physical random phase screens struggled to match experimental data, which suggests that the AME range is higher than expected in highly anisotropic media [97].

Photoacoustic wavefront shaping

Photoacoustic-guided shaping was only explored under simplified assumptions. Future simulations should incorporate realistic acoustic feedback by coupling optical propagation with acoustic modelling tools such as k-Wave [196]. Simulations should also be repeated using angular spectrum propagation to preserve correlations within the medium and facilitate accurate focusing into volumes. These studies could be used to clarify the spatial resolution and sensitivity requirements of a PAWS system to achieve meaningful focus enhancement in biological tissue.

Expanding the T-matrix framework

While CELES and MSTM provided a reasonable foundational basis for this work, existing T-matrix implementations are limited for the applications of modelling WFS and other coherent phenomena. Future development should include the implementation of beam shape coefficients to allow the simulation of generalised incident fields beyond angular spectrum decomposition. The parameter space (particularly high-density regimes) should be more extensively validated against other full-wave methods. Ultimately, a curated dataset of fully characterised T-matrix domains could be generated and shared, supporting reproducibility and enabling benchmarking for the wider WFS and optical modelling communities.

7.3 Synopsis

This thesis has developed a rigorous and efficient computational framework capable of simulating coherent light propagation through tissue-like scattering media. By coupling a discrete particle representation of turbid media with the T-matrix method, it was possible to model coherent phenomena such as WFS with high fidelity. The proposed modelling framework enables full-field access to amplitude and phase information within deep tissue, allowing investigations beyond the reach of existing experimental or numerical techniques. These capabilities open the door to a broad range of future applications in optical imaging, therapy, and computational optics.

Appendix A

Research outputs

The following peer-reviewed publications and conference proceedings were produced during the course of this PhD:

- Bewick, Jake A. J., et al. *Rigorously simulating light transmission and wavefront shaping in turbid media with a T-matrix method. [Under review].*
- Bewick, Jake A. J., et al. *A computational framework for investigating the feasibility of focusing light in biological tissue via photoacoustic wavefront shaping.* Photons Plus Ultrasound: Imaging and Sensing 2023. SPIE, 2023.
- Bewick, Jake, et al. *Full-wave simulation of focusing light through scattering layers using the T-matrix method.* Adaptive Optics and Wavefront Control for Biological Systems IX. SPIE, 2023.
- Bewick, Jake A. J., et al. *Simulating optical memory effects and the scanning of foci using wavefront shaping in tissue-like scattering media.* European Conference on Biomedical Optics. Optica Publishing Group, 2023.
- Bewick, Jake A. J., et al. *Efficient full-wave simulation of wavefront shaping to focus light through biological tissue.* Optics and the Brain. Optica Publishing Group, 2022.
- Bewick, Jake A. J., et al. *Scalable full-wave simulation of coherent light propagation through biological tissue.* 2021 IEEE Photonics Conference (IPC). IEEE, 2021.

Appendix B

Colophon

This document was written in LaTeX using Overleaf and compiled with pdfLaTeX. References were managed with BibTeX.

Post-processing, data analysis, and Figure generation were performed using MATLAB. Vector illustrations and diagrams were prepared using INKSCAPE, and 3D renderings were produced with BLENDER.

Optical modelling was performed using a range of specialised solvers. The T-matrix calculations were carried out using both MSTM (Multi-Sphere T-Matrix) [160] and CELES (CUDA-accelerated Electromagnetic scattering for Large Ensembles of Spheres) [129].

For the validation simulations:

- Monte Carlo simulations were performed using VALOMC [187].
- Optical property measurements were performed using Inverse adding-doubling (IAD) [180].
- Finite-difference time-domain simulations were performed using TDMS [170].

For single particle scattering calculation, a range of Mie theory solvers were used, including:

- Matzler's MIE SCATTERING code [178],
- Kuan Fang Ren's ABSPHERE [169],
- Scott Prahl's online OMLC MIE CALCULATOR [177],
- Peter Munro's MIE CODE [168].

All figures were rendered as vector graphics or publication-quality images. Figure composition and annotation were done in INKSCAPE.

Simulations were run on local workstations (including ZEUS and MNEMOSYNE) and UCL's MYRIAD computing clusters.

Bibliography

[1] Jerome C. Mertz. *Introduction to Optical Microscopy*. Cambridge university press, Cambridge New York, 2nd ed edition, 2019. GSCC: 0000583 2025-06-09T13:46:10.135Z 1.74.

[2] H Owen-Reece, M Smith, C E Elwell, and J C Goldstone. Near infrared spectroscopy. *British Journal of Anaesthesia*, 82(3):418–426, March 1999. GSCC: 0000418 2025-06-09T13:47:17.762Z 0.

[3] David Huang, Eric A. Swanson, Charles P. Lin, Joel S. Schuman, William G. Stinson, Warren Chang, Michael R. Hee, Thomas Flotte, Kenton Gregory, Carmen A. Puliafito, and James G. Fujimoto. Optical coherence tomography. *Science*, 254(5035):1178–1181, November 1991. GSCC: 0019379 2025-06-09T13:47:55.898Z 11.07.

[4] Paul Beard. Biomedical photoacoustic imaging. *Interface Focus*, 1(4):602–631, August 2011. GSCC: 0002557 2025-06-09T13:42:20.787Z 3.54.

[5] T. J. Dougherty, C. J. Gomer, B. W. Henderson, G. Jori, D. Kessel, M. Korbelik, J. Moan, and Q. Peng. Photodynamic therapy. *JNCI Journal of the National Cancer Institute*, 90(12):889–905, June 1998. GSCC: 0007162 2025-06-09T13:49:38.068Z 5.09.

[6] Karl Deisseroth. Optogenetics. *Nature Methods*, 8(1):26–29, January 2011. GSCC: 0002612 2025-06-09T13:48:56.450Z 0.

[7] I. M. Vellekoop and A. P. Mosk. Focusing coherent light through opaque strongly scattering media. *Optics Letters*, 32(16):2309, August 2007. GSCC: 0002188 2025-06-09T13:44:43.903Z 2.35.

[8] Yuecheng Shen, Yan Liu, Cheng Ma, and Lihong V. Wang. Focusing light through biological tissue and tissue-mimicking phantoms up to 9.6 cm in thickness with digital optical phase conjugation. *Journal of Biomedical Optics*, 21(8):085001, August 2016. GSCC: 0000077 2025-06-09T13:44:46.758Z 0.17.

[9] Donald B. Conkey, Antonio M. Caravaca-Aguirre, Jake D. Dove, Hengyi Ju, Todd W. Murray, and Rafael Piestun. Super-resolution photoacoustic imaging through a scattering wall. *Nature Communications*, 6(1):7902, August 2015. GSCC: 0000140 2025-06-10T12:57:26.472Z 0.27.

[10] Youngwoon Choi, Changhyeong Yoon, Moonseok Kim, Taeseok Daniel Yang, Christopher Fang-Yen, Ramachandra R. Dasari, Kyoung Jin Lee, and Wonshik Choi. Scanner-free and wide-field endoscopic imaging by using a single multimode optical fiber. *Physical Review Letters*, 109(20):203901, November 2012. GSCC: 0000697 2025-06-10T12:56:40.429Z 1.06.

[11] Ori Katz, Pierre Heidmann, Mathias Fink, and Sylvain Gigan. Non-invasive single-shot imaging through scattering layers and around corners via speckle correlations. *Nature Photonics*, 8(10):784–790, October 2014. GSCC: 0001278 2025-06-09T13:47:23.844Z 0.

[12] Zizheng Cao, Xuebing Zhang, Gerwin Osnabrugge, Juhao Li, Ivo M. Vellekoop, and Antonius M. J. Koonen. Reconfigurable beam system for non-line-of-sight free-space optical communication. *Light: Science & Applications*, 8(1):69, July 2019. GSCC: 0000140 2025-06-09T13:50:12.043Z 0.46.

[13] Ravitej Uppu, Tom A W Wolterink, Sebastianus A Goorden, Bin Chen, Boris Škorić, Allard P Mosk, and Pepijn W H Pinkse. Asymmetric cryp-

tography with physical unclonable keys. *Quantum Science and Technology*, 4(4):045011, October 2019. GSCC: 0000034 2025-06-09T13:42:01.135Z 0.12.

[14] Gerwin Osnabrugge, Roarke Horstmeyer, Ioannis N. Papadopoulos, Benjamin Judkewitz, and Ivo M. Vellekoop. Generalized optical memory effect. *Optica*, 4(8):886, August 2017. GSCC: 0000251 2025-06-09T13:45:05.002Z 0.62.

[15] Shachar Resisi, Yehonatan Viernik, Sebastien M. Popoff, and Yaron Bromberg. Wavefront shaping in multimode fibers by transmission matrix engineering. *APL Photonics*, 5(3):036103, March 2020. GSCC: 0000081 2025-06-10T12:59:40.152Z 0.29.

[16] Pim Venderbosch, Reinier Van Der Meer, Michiel De Goede, Ben Kassenberg, Henk Snijders, Jörn Epping, Caterina Taballione, Hans Van Den Vlekkert, Jelmer J. Renema, and Pepijn W.H. Pinkse. Observation of open scattering channels. In *Optica Advanced Photonics Congress 2022*, page IM4C.4, Maastricht,Limburg, 2022. Optica Publishing Group. GSCC: 0000002 2025-06-09T13:47:41.866Z 0.01.

[17] Pritam Pai, Jeroen Bosch, Matthias Kühmayer, Stefan Rotter, and Allard P. Mosk. Scattering invariant modes of light in complex media. *Nature Photonics*, 15(6):431–434, June 2021. GSCC: 0000063 2025-06-10T12:56:46.515Z 0.

[18] Jonghee Yoon, Minji Lee, KyeoReh Lee, Nury Kim, Jin Man Kim, Jongchan Park, Hyeonseung Yu, Chulhee Choi, Won Do Heo, and YongKeun Park. Optogenetic control of cell signaling pathway through scattering skull using wavefront shaping. *Scientific Reports*, 5(1):13289, August 2015. GSCC: 0000073 2025-06-09T13:48:49.279Z 0.14.

[19] Lihong V. Wang and Hsin-I Wu. *Biomedical Optics: Principles and Imaging*. Wiley, 1 edition, July 2009. GSCC: 0002471 2025-06-09T13:42:17.387Z 2.98.

[20] Valery V. Tuchin. Tissue optics and photonics: Biological tissue structures. *Journal of Biomedical Photonics & Engineering*, 1(1):3–21, March 2015. GSCC: 0000151 2025-06-11T18:20:41.826Z 0.28.

[21] Steven L Jacques. Optical properties of biological tissues: A review. *Physics in Medicine and Biology*, 58(11):R37–R61, June 2013. GSCC: 0004896 2025-06-09T13:48:17.522Z 7.81.

[22] Craig F. Bohren and Donald R. Huffman. *Absorption and Scattering of Light by Small Particles*. Wiley, 1 edition, April 1998. GSCC: 0035314 2025-06-09T13:41:31.787Z 24.94.

[23] Stefan W. Hell and Jan Wichmann. Breaking the diffraction resolution limit by stimulated emission: stimulated-emission-depletion fluorescence microscopy. *Optics Letters*, 19(11):780, June 1994.

[24] Eric Betzig, George H. Patterson, Rachid Sougrat, O. Wolf Lindwasser, Scott Olenych, Juan S. Bonifacino, Michael W. Davidson, Jennifer Lippincott-Schwartz, and Harald F. Hess. Imaging intracellular fluorescent proteins at nanometer resolution. *Science*, 313(5793):1642–1645, September 2006.

[25] M. G. L. Gustafsson. Surpassing the lateral resolution limit by a factor of two using structured illumination microscopy. *Journal of Microscopy*, 198(2):82–87, May 2000.

[26] T. Dertinger, R. Colyer, G. Iyer, S. Weiss, and J. Enderlein. Fast, background-free, 3D super-resolution optical fluctuation imaging (SOFI). *Proceedings of the National Academy of Sciences*, 106(52):22287–22292, December 2009.

[27] James B. Pawley. *Handbook of Biological Confocal Microscopy*. Springer, New York, 3rd ed edition, 2006.

[28] Winfried Denk, James H. Strickler, and Watt W. Webb. Two-Photon Laser Scanning Fluorescence Microscopy. *Science*, 248(4951):73–76, April 1990. GSCC: 0012715 2025-06-10T12:58:58.835Z 6.93.

[29] Joseph A. Izatt, Eric A. Swanson, James G. Fujimoto, Michael R. Hee, and Gabrielle M. Owen. Optical coherence microscopy in scattering media. *Optics Letters*, 19(8):590, April 1994.

[30] T Durduran, R Choe, W B Baker, and A G Yodh. Diffuse optics for tissue monitoring and tomography. *Reports on Progress in Physics*, 73(7):076701, July 2010.

[31] Sylvain Gigan. Optical microscopy aims deep. *Nature Photonics*, 11(1):14–16, January 2017.

[32] Dennis E.J.G.J. Dolmans, Dai Fukumura, and Rakesh K. Jain. Photodynamic therapy for cancer. *Nature Reviews Cancer*, 3(5):380–387, May 2003. GSCC: 0007824 2025-06-09T13:49:42.745Z 6.78.

[33] Feng Zhang, Viviana Gradinaru, Antoine R Adamantidis, Remy Durand, Raag D Airan, Luis De Lecea, and Karl Deisseroth. Optogenetic interrogation of neural circuits: technology for probing mammalian brain structures. *Nature Protocols*, 5(3):439–456, March 2010. GSCC: 0000944 2025-06-09T13:48:53.439Z 0.

[34] Ivo M. Vellekoop. Feedback-based wavefront shaping. *Optics Express*, 23(9):12189, May 2015. GSCC: 0000485 2025-06-09T13:44:36.355Z 0.92.

[35] Roarke Horstmeyer, Haowen Ruan, and Changhuei Yang. Guidestar-assisted wavefront-shaping methods for focusing light into biological tissue. *Nature Photonics*, 9(9):563–571, September 2015. GSCC: 0000693 2025-06-09T13:45:16.417Z 0.

[36] I. M. Vellekoop, E. G. Van Putten, A. Lagendijk, and A. P. Mosk. Demixing light paths inside disordered metamaterials. *Optics Express*, 16(1):67, 2008. GSCC: 0000282 2025-06-09T13:43:35.268Z 0.31.

[37] Puxiang Lai, Lidai Wang, Jian Wei Tay, and Lihong V. Wang. Photoacoustically guided wavefront shaping for enhanced optical focusing in scattering media. *Nature Photonics*, 9(2):126–132, February 2015. GSCC: 0000369 2025-06-09T13:49:28.230Z 0.

[38] Ori Katz, Eran Small, Yefeng Guan, and Yaron Silberberg. Noninvasive nonlinear focusing and imaging through strongly scattering turbid layers. *Optica*, 1(3):170, September 2014. GSCC: 0000233 2025-06-09T13:47:28.556Z 0.42.

[39] Zahid Yaqoob, Demetri Psaltis, Michael S. Feld, and Changhuei Yang. Optical phase conjugation for turbidity suppression in biological samples. *Nature Photonics*, 2(2):110–115, February 2008. GSCC: 0000922 2025-06-09T13:48:10.750Z 0.

[40] Ivo M. Vellekoop, Meng Cui, and Changhuei Yang. Digital optical phase conjugation of fluorescence in turbid tissue. *Applied Physics Letters*, 101(8):081108, August 2012. GSCC: 0000204 2025-06-09T13:43:54.936Z 0.30.

[41] Chia-Lung Hsieh, Ye Pu, Rachel Grange, Grégoire Laporte, and Demetri Psaltis. Imaging through turbid layers by scanning the phase conjugated second harmonic radiation from a nanoparticle. *Optics Express*, 18(20):20723, September 2010. GSCC: 0000287 2025-06-09T13:45:38.026Z 0.37.

[42] Zhipeng Yu, Jiangtao Huangfu, Fangyuan Zhao, Meiyun Xia, Xi Wu, Xufeng Niu, Deyu Li, Puxiang Lai, and Daifa Wang. Time-reversed magnetically controlled perturbation (TRMCP) optical focusing inside scattering media. *Scientific Reports*, 8(1):2927, February 2018. GSCC: 0000046 2025-06-10T12:58:31.471Z 0.12.

[43] Yan Liu, Puxiang Lai, Cheng Ma, Xiao Xu, Alexander A. Grabar, and Lihong V. Wang. Optical focusing deep inside dynamic scattering media with near-infrared time-reversed ultrasonically encoded (TRUE) light. *Nature Communications*, 6(1):5904, January 2015. Publisher: Nature Publishing Group.

[44] S. M. Popoff, G. Lerosey, R. Carminati, M. Fink, A. C. Boccara, and S. Gigan. Measuring the transmission matrix in optics: An approach to the study and control of light propagation in disordered media. *Physical Review Letters*, 104(10):100601, March 2010. GSCC: 0002052 2025-06-09T13:46:58.585Z 2.57.

[45] Sébastien Popoff, Geoffroy Lerosey, Mathias Fink, Albert Claude Boccara, and Sylvain Gigan. Image transmission through an opaque material. *Nature Communications*, 1(1):81, September 2010.

[46] Yunzhe Li, Yujia Xue, and Lei Tian. Deep speckle correlation: a deep learning approach toward scalable imaging through scattering media. *Optica*, 5(10):1181–1190, October 2018. Publisher: Optica Publishing Group.

[47] Alex Turpin, Ivan Vishniakou, and Johannes d Seelig. Light scattering control in transmission and reflection with neural networks. *Optics Express*, 26(23):30911–30929, November 2018. Publisher: Optica Publishing Group.

[48] Alexandra d'Arco, Fei Xia, Antoine Boniface, Jonathan Dong, and Sylvain Gigan. Physics-based neural network for non-invasive control of coherent light in scattering media. *Optics Express*, 30(17):30845–30856, August 2022. Publisher: Optica Publishing Group.

[49] I.M. Vellekoop and A.P. Mosk. Phase control algorithms for focusing light through turbid media. *Optics Communications*, 281(11):3071–3080, June 2008. GSCC: 0000577 2025-06-09T13:49:13.366Z 0.

[50] J.V. Thompson, B.H. Hokr, and V.V. Yakovlev. Optimization of focusing through scattering media using the continuous sequential algorithm. *Journal*

of Modern Optics, 63(1):80–84, January 2016. GSCC: 0000043 2025-06-09T13:48:42.995Z 0.09.

[51] Zahra Fayyaz, Nafiseh Mohammadian, M. Reza Rahimi Tabar, Rayyan Manwar, and Kamran Avanaki. A comparative study of optimization algorithms for wavefront shaping. *Journal of Innovative Optical Health Sciences*, 12(04):1942002, July 2019. GSCC: 0000047 2025-06-09T13:40:52.295Z 0.

[52] Donald B. Conkey, Albert N. Brown, Antonio M. Caravaca-Aguirre, and Rafael Piestun. Genetic algorithm optimization for focusing through turbid media in noisy environments. *Optics Express*, 20(5):4840, February 2012. GSCC: 0000480 2025-06-09T13:45:08.693Z 0.69.

[53] Minghua Xu and Lihong V. Wang. Photoacoustic imaging in biomedicine. *Review of Scientific Instruments*, 77(4):041101, April 2006. GSCC: 0003342 2025-06-09T13:49:17.911Z 3.34.

[54] Lihong V. Wang and Song Hu. Photoacoustic tomography: *In vivo* imaging from organelles to organs. *Science*, 335(6075):1458–1462, March 2012. GSCC: 0004656 2025-06-09T13:49:22.472Z 6.75.

[55] Puxiang Lai, Lidai Wang, Jian Wei Tay, and Lihong V. Wang. Nonlinear photoacoustic wavefront shaping (PAWS) for single speckle-grain optical focusing in scattering media, 2014. GSCC: 0000021 2025-06-09T13:47:31.740Z 0.04 Version Number: 1.

[56] Thomas Chaigne, Jérôme Gateau, Ori Katz, Emmanuel Bossy, and Sylvain Gigan. Light focusing and two-dimensional imaging through scattering media using the photoacoustic transmission matrix with an ultrasound array. *Optics Letters*, 39(9):2664, May 2014. GSCC: 0000056 2025-06-09T13:46:17.024Z 0.10.

[57] T. Chaigne, O. Katz, A. C. Boccara, M. Fink, E. Bossy, and S. Gigan. Controlling light in scattering media non-invasively using the photoacoustic

transmission matrix. *Nature Photonics*, 8(1):58–64, January 2014. GSCC: 0000319 2025-06-09T13:43:13.402Z 0.

[58] James G. Fujimoto, Costas Pitris, Stephen A. Boppart, and Mark E. Brezinski. Optical coherence tomography: An emerging technology for biomedical imaging and optical biopsy. *Neoplasia*, 2(1-2):9–25, January 2000. GSCC: 0001610 2025-06-09T13:48:00.953Z 0.

[59] A F Fercher, W Drexler, C K Hitzenberger, and T Lasser. Optical coherence tomography - principles and applications. *Reports on Progress in Physics*, 66(2):239–303, February 2003. GSCC: 0000587 2025-06-09T13:47:59.017Z 0.50.

[60] Hyeonseung Yu, Jaeduck Jang, Jaeguyn Lim, Jung-Hoon Park, Wooyoung Jang, Ji-Yeun Kim, and YongKeun Park. Depth-enhanced 2-D optical coherence tomography using complex wavefront shaping. *Optics Express*, 22(7):7514, April 2014. GSCC: 0000062 2025-06-09T13:43:38.881Z 0.11.

[61] Hyeonseung Yu, Peter Lee, KyeoReh Lee, Jaeduck Jang, Jaeguyn Lim, Wooyoung Jang, Yong Jeong, and YongKeun Park. *In vivo* deep tissue imaging using wavefront shaping optical coherence tomography. *Journal of Biomedical Optics*, 21(10):101406, February 2016. GSCC: 0000037 2025-06-09T13:45:46.945Z 0.08.

[62] Jong Uk Kim, Hyun Choi, YongKeun Park, and Jonghwa Shin. Finite-difference time-domain analysis of increased penetration depth in optical coherence tomography by wavefront shaping. *Biomedical Optics Express*, 9(8):3883, August 2018. GSCC: 0000012 2025-06-09T13:44:40.128Z 0.03.

[63] Peter A. Santi. Light sheet fluorescence microscopy: A review. *Journal of Histochemistry & Cytochemistry*, 59(2):129–138, February 2011. GSCC: 0000573 2025-06-09T13:46:36.317Z 0.

[64] Joel Kubby, Sylvain Gigan, and Meng Cui, editors. *Wavefront Shaping for Biomedical Imaging*. Cambridge University Press, 1 edition, May 2019. GSCC: 0000048 2025-06-10T12:59:32.639Z 0.15.

[65] H. I. C. Dalgarno, T. Čižmár, T. Vettenburg, J. Nylk, F. J. Gunn-Moore, and K. Dholakia. Wavefront corrected light sheet microscopy in turbid media. *Applied Physics Letters*, 100(19):191108, May 2012. GSCC: 0000046 2025-06-10T12:59:24.535Z 0.07.

[66] Jale Schneider and Christof M. Aegerter. Dynamic light sheet generation and fluorescence imaging behind turbid media. *Journal of the European Optical Society-Rapid Publications*, 14(1):7, December 2018. GSCC: 0000007 2025-06-09T13:44:04.300Z 0.

[67] Jayan Mannath and Matthew Banks. Emerging technologies in endoscopic imaging. *F1000 Medicine Reports*, 4, February 2012. GSCC: 0000014 2025-06-09T13:44:12.196Z 0.02.

[68] Ioannis N. Papadopoulos, Salma Farahi, Christophe Moser, and Demetri Psaltis. Focusing and scanning light through a multimode optical fiber using digital phase conjugation. *Optics Express*, 20(10):10583, May 2012. GSCC: 0000517 2025-06-09T13:44:42.610Z 0.76.

[69] Ioannis N. Papadopoulos, Salma Farahi, Christophe Moser, and Demetri Psaltis. High-resolution, lensless endoscope based on digital scanning through a multimode optical fiber. *Biomedical Optics Express*, 4(2):260, February 2013. GSCC: 0000419 2025-06-09T13:45:25.953Z 0.65.

[70] Donggyu Kim, Jungho Moon, Moonseok Kim, Taeseok Daniel Yang, Jaisoon Kim, Euiheon Chung, and Wonshik Choi. Pixelation-free and real-time endoscopic imaging through a fiber bundle, 2013. GSCC: 0000010 2025-06-09T13:49:49.240Z 0.02 Version Number: 1.

[71] Benjamin Keenlyside, Dylan Marques, Maxim Cherkashin, Edward Zhang, Peter Munro, Paul Beard, and James Guggenheim. Wavefront shaping

through multimode fibres to enable endoscopic photoacoustic tomography. In Thomas G. Bifano, Sylvain Gigan, and Na Ji, editors, *Adaptive Optics and Wavefront Control for Biological Systems VII*, page 14, Online Only, United States, March 2021. SPIE. GSCC: 0000005 2025-06-10T12:59:46.367Z 0.02.

[72] Omer Tzang, Eyal Niv, Sakshi Singh, Simon Labouesse, Greg Myatt, and Rafael Piestun. Wavefront shaping in complex media with a 350 kHz modulator via a 1D-to-2D transform. *Nature Photonics*, 13(11):788–793, November 2019. GSCC: 0000149 2025-06-10T12:59:36.793Z 0.

[73] Muhammad Mohsin Qureshi, Joshua Brake, Hee-Jae Jeon, Haowen Ruan, Yan Liu, Abdul Mohaimen Safi, Tae Joong Eom, Changhuei Yang, and Euiheon Chung. *In vivo* study of optical speckle decorrelation time across depths in the mouse brain. *Biomedical Optics Express*, 8(11):4855, November 2017. GSCC: 0000088 2025-06-09T13:45:49.957Z 0.22.

[74] Lief Fenno, Ofer Yizhar, and Karl Deisseroth. The development and application of optogenetics. *Annual Review of Neuroscience*, 34(1):389–412, July 2011. GSCC: 0002297 2025-06-10T12:57:50.740Z 3.17.

[75] Matthew R. Banghart, Matthew Volgraf, and Dirk Trauner. Engineering light-gated ion channels. *Biochemistry*, 45(51):15129–15141, December 2006. GSCC: 0000167 2025-06-09T13:44:14.356Z 0.17.

[76] A. Ashkin, J. M. Dziedzic, J. E. Bjorkholm, and Steven Chu. Observation of a single-beam gradient force optical trap for dielectric particles. *Optics Letters*, 11(5):288, May 1986. GSCC: 0009609 2025-06-09T13:47:39.290Z 4.71.

[77] Michael A. Taylor, Muhammad Waleed, Alexander B. Stilgoe, Halina Rubinsztein-Dunlop, and Warwick P. Bowen. Enhanced optical trapping via structured scattering. *Nature Photonics*, 9(10):669–673, October 2015. GSCC: 0000111 2025-06-09T13:44:17.745Z 0.

[78] Michael A. Taylor. Optimizing phase to enhance optical trap stiffness. *Scientific Reports*, 7(1):555, April 2017. GSCC: 0000018 2025-06-09T13:48:46.046Z 0.04.

[79] Max Born, Emil Wolf, A. B. Bhatia, P. C. Clemmow, D. Gabor, A. R. Stokes, A. M. Taylor, P. A. Wayman, and W. L. Wilcock. *Principles of Optics: Electromagnetic Theory of Propagation, Interference and Diffraction of Light*. Cambridge University Press, 7 edition, October 1999. GSCC: 0081501 2025-06-09T13:49:59.910Z 60.87.

[80] Jung-Hoon Park, Chunghyun Park, Yong-Hoon Cho, and YongKeun Park. Scattering super-lens: subwavelength light focusing and imaging via wavefront shaping in complex media. In *Asia Communications and Photonics Conference 2014*, page ATh4H.4, Shanghai, 2014. OSA. GSCC: 0000004 2025-06-10T12:56:53.812Z 0.01.

[81] I. M. Vellekoop, A. Lagendijk, and A. P. Mosk. Exploiting disorder for perfect focusing. *Nature Photonics*, 4(5):320–322, May 2010. GSCC: 0000929 2025-06-09T13:44:30.967Z 0.

[82] Bahram Javidi, Artur Carnicer, Masahiro Yamaguchi, Takanori Nomura, Elisabet Pérez-Cabré, María S Millán, Naveen K Nishchal, Roberto Torroba, John Fredy Barrera, Wenqi He, Xiang Peng, Adrian Stern, Yair Rivenson, A Alfalou, C Brosseau, Changliang Guo, John T Sheridan, Guohai Situ, Makoto Naruse, Tsutomu Matsumoto, Ignasi Juvells, Enrique Tajahuerce, Jesús Lancis, Wen Chen, Xudong Chen, Pepijn W H Pinkse, Allard P Mosk, and Adam Markman. Roadmap on optical security. *Journal of Optics*, 18(8):083001, August 2016. GSCC: 0000476 2025-06-09T13:50:29.076Z 1.03.

[83] Sebastianus A. Goorden, Marcel Horstmann, Allard P. Mosk, Boris Škorić, and Pepijn W. H. Pinkse. Quantum-secure authentication of a physical un-

clonable key. *Optica*, 1(6):421, December 2014. GSCC: 0000224 2025-06-09T13:50:03.695Z 0.41.

[84] W. K. Wootters and W. H. Zurek. A single quantum cannot be cloned. *Nature*, 299(5886):802–803, October 1982. GSCC: 0007879 2025-06-09T13:41:24.047Z 0.

[85] Meihua Liao, Dajiang Lu, Wenqi He, and Xiang Peng. Optical cryptanalysis method using wavefront shaping. *IEEE Photonics Journal*, 9(1):1–13, February 2017. GSCC: 0000012 2025-06-09T13:48:04.550Z 0.

[86] Vincent W. S. Chan. Free-space optical communications. *Journal of Lightwave Technology*, 24(12):4750–4762, December 2006. GSCC: 0001040 2025-06-09T13:44:52.286Z 0.

[87] Nadège Kaina, Matthieu Dupré, Geoffroy Lerosey, and Mathias Fink. Shaping complex microwave fields in reverberating media with binary tunable metasurfaces. *Scientific Reports*, 4(1):6693, October 2014. GSCC: 0000265 2025-06-10T12:57:03.714Z 0.48.

[88] Marzieh Najafi, Bernhard Schmauss, and Robert Schober. Intelligent reflecting surfaces for free space optical communications, 2020. GSCC: 0000127 2025-06-09T13:45:53.196Z 0.45 Version Number: 2.

[89] Yan Liu, Cheng Ma, Yuecheng Shen, Junhui Shi, and Lihong V. Wang. Focusing light inside dynamic scattering media with millisecond digital optical phase conjugation. *Optica*, 4(2):280, February 2017. GSCC: 0000185 2025-06-09T13:44:45.442Z 0.43.

[90] Sylvain Gigan, Ori Katz, Hilton B De Aguiar, Esben Ravn Andresen, Alexandre Aubry, Jacopo Bertolotti, Emmanuel Bossy, Dorian Bouchet, Joshua Brake, Sophie Brasselet, Yaron Bromberg, Hui Cao, Thomas Chaigne, Zhongtao Cheng, Wonshik Choi, Tomáš Čižmár, Meng Cui, Vincent R Curtis, Hugo Defienne, Matthias Hofer, Ryoichi Horisaki, Roarke Horstmeyer,

Na Ji, Aaron K LaViolette, Jerome Mertz, Christophe Moser, Allard P Mosk, Nicolas C Pégard, Rafael Piestun, Sebastien Popoff, David B Phillips, Demetri Psaltis, Babak Rahmani, Hervé Rigneault, Stefan Rotter, Lei Tian, Ivo M Vellekoop, Laura Waller, Lihong Wang, Timothy Weber, Sheng Xiao, Chris Xu, Alexey Yamilov, Changhuei Yang, and Hasan Yılmaz. Roadmap on wavefront shaping and deep imaging in complex media. *Journal of Physics: Photonics*, 4(4):042501, October 2022. GSCC: 0000177 2025-06-09T13:50:33.804Z 1.26.

[91] Abhilash Thendiyammal, Gerwin Osnabrugge, Tom Knop, and Ivo M. Vellekoop. Model-based wavefront shaping microscopy. *Optics Letters*, 45(18):5101–5104, September 2020. Publisher: Optica Publishing Group.

[92] Gerwin Osnabrugge, Saroch Leedumrongwatthanakun, and Ivo M. Vellekoop. A convergent Born series for solving the inhomogeneous Helmholtz equation in arbitrarily large media. *Journal of Computational Physics*, 322:113–124, October 2016.

[93] Allard Mosk. Open channels in scattering media: See the light inside. In *Frontiers in Optics 2016*, page FW2D.3, Rochester, New York, 2016. OSA. GSCC: 0000000 2025-06-16T12:45:06.572Z 0.00.

[94] Shechao Feng, Charles Kane, Patrick A. Lee, and A. Douglas Stone. Correlations and fluctuations of coherent wave transmission through disordered media. *Physical Review Letters*, 61(7):834–837, August 1988. Publisher: American Physical Society.

[95] Isaac Freund, Michael Rosenbluh, and Shechao Feng. Memory effects in propagation of optical waves through disordered media. *Physical Review Letters*, 61(20):2328–2331, November 1988. GSCC: 0000955 2025-06-09T13:47:03.225Z 0.50.

[96] Jacopo Bertolotti, Elbert G. Van Putten, Christian Blum, Ad Lagendijk, Willem L. Vos, and Allard P. Mosk. Non-invasive imaging through opaque

scattering layers. *Nature*, 491(7423):232–234, November 2012. GSCC: 0001343 2025-06-09T13:47:21.401Z 0.

[97] Sam Schott, Jacopo Bertolotti, Jean-Francois Léger, Laurent Bourdieu, and Sylvain Gigan. Characterization of the angular memory effect of scattered light in biological tissues. *Optics Express*, 23(10):13505, May 2015. GSCC: 0000210 2025-06-09T13:42:38.046Z 0.40.

[98] Benjamin Judkewitz, Roarke Horstmeyer, Ivo M. Vellekoop, Ioannis N. Papadopoulos, and Changhuei Yang. Translation correlations in anisotropically scattering media. *Nature Physics*, 11(8):684–689, August 2015. Publisher: Nature Publishing Group.

[99] Jake Bewick, Peter R. T. Munro, Simon Arridge, and James Guggenheim. Simulating optical memory effects and the scanning of foci using wavefront shaping in tissue-like scattering media. In Maciej Wojtkowski, Yoshiaki Yasuno, and Benjamin J. Vakoc, editors, *Optical Coherence Imaging Techniques and Imaging in Scattering Media V*, page 53, Munich, Germany, August 2023. SPIE. GSCC: 0000000 2025-06-16T12:44:34.684Z 0.00.

[100] Zahra Fayyaz, Nafiseh Mohammadian, and Mohammad R. N. Avanaki. Comparative assessment of five algorithms to control an SLM for focusing coherent light through scattering media. In Alexander A. Oraevsky and Lihong V. Wang, editors, *Photons Plus Ultrasound: Imaging and Sensing 2018*, page 229, San Francisco, United States, February 2018. SPIE. GSCC: 0000005 2025-06-09T13:42:44.595Z 0.01.

[101] Chen Bar, Marina Alterman, Ioannis Gkioulekas, and Anat Levin. A Monte Carlo framework for rendering speckle statistics in scattering media. *ACM Transactions on Graphics*, 38(4):1–22, August 2019. GSCC: 0000051 2025-06-09T13:41:03.235Z 0.17.

[102] Jiamiao Yang, Jingwei Li, Sailing He, and Lihong V. Wang. Angular-spectrum modeling of focusing light inside scattering media by optical phase

conjugation. *Optica*, 6(3):250, March 2019. GSCC: 0000062 2025-06-09T13:41:49.809Z 0.19.

[103] Renhao Liu, Yu Sun, Jiabei Zhu, Lei Tian, and Ulugbek S. Kamilov. Recovery of continuous 3D refractive index maps from discrete intensity-only measurements using neural fields. *Nature Machine Intelligence*, 4(9):781–791, September 2022. Publisher: Nature Publishing Group.

[104] Larry Andrews and Ronald Phillips. Propagation Through Random Phase Screens. PM152:647–667, September 2005. Publisher: SPIE.

[105] Joseph F. Benzoni, Sarben Sarkar, and David Sherrington. Random phase screens. *JOSA A*, 4(1):17–26, January 1987. Publisher: Optica Publishing Group.

[106] Malchiel Haskel and Adrian Stern. Modeling optical memory effects with phase screens. *Optics Express*, 26(22):29231, October 2018. GSCC: 0000012 2025-06-11T18:22:14.703Z 0.03.

[107] S. A. Prahl. A Monte Carlo model of light propagation in tissue. page 1030509, Berlin, Germany, January 1989. GSCC: 0001224 2025-06-09T13:41:08.110Z 0.64.

[108] Valery V. Tuchin, Lihong V. Wang, and Dmitry A. Zimnyakov. *Optical Polarization in Biomedical Applications*. Biological and Medical Physics, Biomedical Engineering. Springer Berlin Heidelberg, Berlin, Heidelberg, 2006. GSCC: 0000466 2025-06-09T13:48:13.452Z 0.46.

[109] J. M. Schmitt and G. Kumar. Turbulent nature of refractive-index variations in biological tissue. *Optics Letters*, 21(16):1310, August 1996. GSCC: 0000441 2025-06-10T12:58:51.480Z 0.29.

[110] Howard R. Gordon. Light scattering and absorption by randomly-oriented cylinders: Dependence on aspect ratio for refractive indices applicable for

marine particles. *Optics Express*, 19(5):4673, February 2011. GSCC: 0000033 2025-06-09T13:46:24.976Z 0.04.

[111] Tom Rother, Karsten Schmidt, Jochen Wauer, Valery Shcherbakov, and Jean-Francois Gayet. Light scattering on Chebyshev particles of higher order. *Applied Optics*, 45(23):6030, August 2006. GSCC: 0000060 2025-06-09T13:46:32.597Z 0.06.

[112] H. C. van de Hulst. *Light Scattering by Small Particles*. Dover Publications, New York, 1981. GSCC: 0021510 2025-06-09T13:46:28.773Z 9.28.

[113] G.C. Beck, N. Akgün, A. Rück, and R. Steiner. Design and characterisation of a tissue phantom system for optical diagnostics. *Lasers in Medical Science*, 13(3):160–171, October 1998. GSCC: 0000078 2025-06-09T13:43:41.123Z 0.06.

[114] S Arridge, P Van Der Zee, D T Delpy, and M Cope. Particle sizing in the Mie scattering region: singular-value analysis. *Inverse Problems*, 5(5):671–689, October 1989. GSCC: 0000028 2025-06-09T13:49:02.839Z 0.02.

[115] Joseph M. Schmitt and Gitesh Kumar. Optical scattering properties of soft tissue: a discrete particle model. *Applied Optics*, 37(13):2788, May 1998. GSCC: 0000618 2025-06-09T13:48:32.950Z 0.44.

[116] P. Sumithra and D. Thiripurasundari. Review on computational electromagnetics. *Advanced Electromagnetics*, 6(1):42, March 2017. GSCC: 0000105 2025-06-09T13:50:25.092Z 0.24.

[117] Kane Yee. Numerical solution of initial boundary value problems involving maxwell's equations in isotropic media. *IEEE Transactions on Antennas and Propagation*, 14(3):302–307, May 1966. GSCC: 0022846 2025-06-09T13:47:34.749Z 0.

[118] Allen Taflove, Susan C. Hagness, and Melinda Piket-May. Computational Electromagnetics: The Finite-Difference Time-Domain Method. In *The*

Electrical Engineering Handbook, pages 629–670. Elsevier, 2005. GSCC: 0024778 2025-06-16T12:44:48.647Z 23.20.

[119] David B. Davidson. *Computational Electromagnetics for RF and Microwave Engineering*. Cambridge University press, Cambridge, réimpr. edition, 2005. GSCC: 0000799 2025-06-09T13:43:01.291Z 0.75.

[120] Jean-Pierre Berenger. A perfectly matched layer for the absorption of electromagnetic waves. *Journal of Computational Physics*, 114(2):185–200, October 1994. GSCC: 0014661 2025-06-09T13:41:15.662Z 0.

[121] Q.H. Liu. The pseudospectral time-domain (PSTD) method: A new algorithm for solutions of Maxwell's equations. In *IEEE Antennas and Propagation Society International Symposium 1997. Digest*, volume 1, pages 122–125, Montreal, Que., Canada, 1997. IEEE. GSCC: 0000091 2025-06-10T12:58:08.164Z 0.06.

[122] Q. H. Liu. The PSTD algorithm: A time-domain method requiring only two cells per wavelength. *Microwave and Optical Technology Letters*, 15(3):158–165, June 1997. GSCC: 0000674 2025-06-10T12:58:12.939Z 0.46.

[123] Krishnaswamy Sankaran. Are you using the right tools in computational electromagnetics? *Engineering Reports*, 1(3):e12041, October 2019. GSCC: 0000036 2025-06-09T13:41:56.448Z 0.

[124] Jin-Fa Lee, R. Lee, and A. Cangellaris. Time-domain finite-element methods. *IEEE Transactions on Antennas and Propagation*, 45(3):430–442, March 1997. GSCC: 0000615 2025-06-10T12:58:24.846Z 0.

[125] A. Bondeson, Thomas Rylander, and Pär Ingelström. *Computational Electromagnetics*. Number 51 in Texts in applied mathematics. Springer, New York, N.Y. [London], 2005. GSCC: 0000105 2025-06-09T13:42:57.163Z 0.10.

[126] Martin Costabel. Principles of boundary element methods. *Computer Physics Reports*, 6(1-6):243–274, August 1987. GSCC: 0000139 2025-06-09T13:49:57.527Z 0.

[127] Daniel Mackowski. The Extension of Mie Theory to Multiple Spheres. In Wolfram Hergert and Thomas Wriedt, editors, *The Mie Theory: Basics and Applications*, pages 223–256. Springer, Berlin, Heidelberg, 2012.

[128] P.C. Waterman. Matrix formulation of electromagnetic scattering. *Proceedings of the IEEE*, 53(8):805–812, 1965. GSCC: 0001538 2025-06-09T13:46:47.333Z 0.49.

[129] Amos Egel, Lorenzo Pattelli, Giacomo Mazzamuto, Diederik S. Wiersma, and Uli Lemmer. CELES: CUDA-accelerated simulation of electromagnetic scattering by large ensembles of spheres. *Journal of Quantitative Spectroscopy and Radiative Transfer*, 199:103–110, September 2017. GSCC: 0000126 2025-06-09T13:42:34.078Z 0.

[130] Nail A. Gumerov and Ramani Duraiswami. Computation of scattering from clusters of spheres using the fast multipole method. *The Journal of the Acoustical Society of America*, 117(4):1744–1761, April 2005. GSCC: 0000083 2025-06-09T13:42:51.535Z 0.08.

[131] Michael I. Mishchenko, Larry D. Travis, and Daniel W. Mackowski. T-matrix computations of light scattering by nonspherical particles: A review. *Journal of Quantitative Spectroscopy and Radiative Transfer*, 55(5):535–575, May 1996. GSCC: 0001535 2025-06-10T12:57:34.939Z 0.

[132] Thomas Wriedt and Ute Comberg. Comparison of computational scattering methods. *Journal of Quantitative Spectroscopy and Radiative Transfer*, 60(3):411–423, September 1998. GSCC: 0000115 2025-06-09T13:42:49.521Z 0.

[133] Caigang Zhu and Quan Liu. Review of Monte Carlo modeling of light transport in tissues. *Journal of Biomedical Optics*, 18(5):050902, May 2013. GSCC: 0000465 2025-06-09T13:50:20.915Z 0.74.

[134] Joseph W. Goodman. *Introduction to Fourier Optics*. Roberts & Co, Englewood, Colo, 3rd ed edition, 2005. GSCC: 0032258 2025-06-09T13:46:05.987Z 30.23 OCLC: ocm56632414.

[135] Swapnil Mache and Ivo M. Vellekoop. Domain decomposition of the modified Born series approach for large-scale wave propagation simulations, March 2025. arXiv:2410.02395 [physics].

[136] Michael I. Mishchenko, Larry D. Travis, and Daniel W. Mackowski. T-matrix method and its applications to electromagnetic scattering by particles: A current perspective. *Journal of Quantitative Spectroscopy and Radiative Transfer*, 111(11):1700–1703, July 2010.

[137] M.I. Mishchenko and P.A. Martin. Peter Waterman and T-matrix methods. *Journal of Quantitative Spectroscopy and Radiative Transfer*, 123:2–7, July 2013.

[138] Michael I. Mishchenko, Li Liu, and Daniel W. Mackowski. T-matrix modeling of linear depolarization by morphologically complex soot and soot-containing aerosols. *Journal of Quantitative Spectroscopy and Radiative Transfer*, 123:135–144, July 2013. GSCC: 0000074 2025-06-11T18:21:20.213Z 0.

[139] Claudio Scarchilli, Alberto Adriani, Francesco Cairo, Guido Di Donfrancesco, Carlo Buontempo, Marcel Snels, Maria Luisa Moriconi, Terry Deshler, Niels Larsen, Beiping Luo, Konrad Mauersberger, Joelle Ovarlez, Jim Rosen, and Jochen Schreiner. Determination of polar stratospheric cloud particle refractive indices by use of in situ optical measurements and T-matrix calculations. *Applied Optics*, 44(16):3302–3311, June 2005. Publisher: Optica Publishing Group.

[140] Stephan Havemann and Anthony J. Baran. Calculation of the phase matrix elements of elongated hexagonal ice columns using the T-matrix method. *Journal of Quantitative Spectroscopy and Radiative Transfer*, 89(1):87–96, November 2004.

[141] Rosalba Saija, Maria Antonia Iatì, Ferdinando Borghese, Paolo Denti, Santi Aiello, and Cesare Cecchi-Pestellini. Beyond Mie Theory: The Transition Matrix Approach in Interstellar Dust Modeling. *The Astrophysical Journal*, 559(2):993, October 2001.

[142] Gen Ito, Michael I. Mishchenko, and Timothy D. Glotch. Radiative-Transfer Modeling of Spectra of Planetary Regoliths Using Cluster-Based Dense Packing Modifications. *Journal of Geophysical Research: Planets*, 123(5):1203–1220, 2018. _eprint: https://agupubs.onlinelibrary.wiley.com/doi/pdf/10.1029/2018JE005532.

[143] Michael I. Mishchenko. Comprehensive thematic T-matrix reference database: a 2017–2019 update. *Journal of Quantitative Spectroscopy and Radiative Transfer*, 242:106692, February 2020. GSCC: 0000062 2025-06-11T18:21:59.947Z 0.

[144] Michael I. Mishchenko, Gorden Videen, Nikolai G. Khlebtsov, and Thomas Wriedt. Comprehensive T-matrix reference database: A 2012–2013 update. *Journal of Quantitative Spectroscopy and Radiative Transfer*, 123:145–152, July 2013. GSCC: 0000041 2025-06-11T18:21:52.120Z 0.

[145] Michael I. Mishchenko, Gorden Videen, Victor A. Babenko, Nikolai G. Khlebtsov, and Thomas Wriedt. Comprehensive T-matrix reference database: A 2004–06 update. *Journal of Quantitative Spectroscopy and Radiative Transfer*, 106(1-3):304–324, July 2007. GSCC: 0000093 2025-06-11T18:21:37.029Z 0.

[146] G. Gouesbet. Latest achievements in generalized Lorenz-Mie theories: A commented reference database. *Annalen der Physik*, 526(11-12):461–489, December 2014. GSCC: 0000048 2025-06-09T13:46:12.335Z 0.

[147] Michael I. Mishchenko, Nadezhda T. Zakharova, Nikolai G. Khlebtsov, Gorden Videen, and Thomas Wriedt. Comprehensive thematic T-matrix reference database: A 2015–2017 update. *Journal of Quantitative Spectroscopy and Radiative Transfer*, 202:240–246, November 2017. GSCC: 0000048 2025-06-11T18:21:56.985Z 0.

[148] Michael I. Mishchenko, Nadia T. Zakharova, Gorden Videen, Nikolai G. Khlebtsov, and Thomas Wriedt. Comprehensive T-matrix reference database: A 2007–2009 update. *Journal of Quantitative Spectroscopy and Radiative Transfer*, 111(4):650–658, March 2010. GSCC: 0000075 2025-06-11T18:21:53.985Z 0.

[149] Michael I. Mishchenko, Nadezhda T. Zakharova, Nikolai G. Khlebtsov, Gorden Videen, and Thomas Wriedt. Comprehensive thematic T-matrix reference database: A 2014–2015 update. *Journal of Quantitative Spectroscopy and Radiative Transfer*, 178:276–283, July 2016. GSCC: 0000038 2025-06-11T18:21:50.688Z 0.

[150] Nadezhda T. Zakharova, Gorden Videen, and Nikolai G. Khlebtsov. Comprehensive T-matrix reference database: A 2009–2011 update. *Journal of Quantitative Spectroscopy and Radiative Transfer*, 113(14):1844–1852, September 2012. GSCC: 0000029 2025-06-11T18:21:47.842Z 0.

[151] Michael I. Mishchenko, Gorden Videen, Nikolai G. Khlebtsov, Thomas Wriedt, and Nadia T. Zakharova. Comprehensive T-matrix reference database: A 2006–07 update. *Journal of Quantitative Spectroscopy and Radiative Transfer*, 109(8):1447–1460, May 2008. GSCC: 0000071 2025-06-11T18:21:43.083Z 0.

[152] Michael I. Mishchenko, Nadezhda T. Zakharova, Nikolai G. Khlebtsov, Thomas Wriedt, and Gorden Videen. Comprehensive thematic T-matrix reference database: A 2013–2014 update. *Journal of Quantitative Spectroscopy and Radiative Transfer*, 146:349–354, October 2014. GSCC: 0000062 2025-06-11T18:21:34.094Z 0.

[153] W.R.C. Somerville, B. Auguié, and E.C. Le Ru. smarties: User-friendly codes for fast and accurate calculations of light scattering by spheroids. *Journal of Quantitative Spectroscopy and Radiative Transfer*, 174:39–55, May 2016. GSCC: 0000067 2025-06-10T12:57:14.463Z 0.

[154] G. Gouesbet, J.A. Lock, and G. Gréhan. Generalized Lorenz–Mie theories and description of electromagnetic arbitrary shaped beams: Localized approximations and localized beam models, a review. *Journal of Quantitative Spectroscopy and Radiative Transfer*, 112(1):1–27, January 2011. GSCC: 0000210 2025-06-09T13:45:01.538Z 0.

[155] Yu-lin Xu and Bo Å.S. Gustafson. A generalized multiparticle Mie-solution: further experimental verification. *Journal of Quantitative Spectroscopy and Radiative Transfer*, 70(4-6):395–419, August 2001. GSCC: 0000199 2025-06-09T13:40:59.023Z 0.

[156] Thomas Wriedt. Mie Theory: A Review. In Wolfram Hergert and Thomas Wriedt, editors, *The Mie Theory*, volume 169, pages 53–71. Springer Berlin Heidelberg, Berlin, Heidelberg, 2012. GSCC: 0000326 2025-06-09T13:47:06.535Z 0.46 Series Title: Springer Series in Optical Sciences.

[157] Daniel W. Mackowski and Michael I. Mishchenko. Calculation of the T-matrix and the scattering matrix for ensembles of spheres. *Journal of the Optical Society of America A*, 13(11):2266, November 1996. GSCC: 0000954 2025-06-09T13:42:28.445Z 0.64.

[158] Daniel W. Mackowski. Calculation of total cross sections of multiple-sphere clusters. *Journal of the Optical Society of America A*, 11(11):2851, November 1994. GSCC: 0000515 2025-06-09T13:42:30.463Z 0.32.

[159] Michael I. Mishchenko, Larry D. Travis, and Andrew Lacis. *Scattering, Absorption, and Emission of Light by Small Particles*. Cambridge Univ. Press, Cambridge, 1. publ edition, 2002. GSCC: 0003457 2025-06-10T12:56:55.741Z 2.82.

[160] D.W. Mackowski and M.I. Mishchenko. A multiple sphere T-matrix Fortran code for use on parallel computer clusters. *Journal of Quantitative Spectroscopy and Radiative Transfer*, 112(13):2182–2192, September 2011. GSCC: 0000525 2025-06-09T13:41:13.153Z 0.

[161] W. J. Wiscombe. Improved Mie scattering algorithms. *Applied Optics*, 19(9):1505, May 1980. GSCC: 0002225 2025-06-09T13:45:44.437Z 0.95.

[162] D.W. Mackowski and L. Kolokolova. Application of the multiple sphere superposition solution to large–scale systems of spheres via an accelerated algorithm. *Journal of Quantitative Spectroscopy and Radiative Transfer*, 287:108221, September 2022. GSCC: 0000015 2025-06-09T13:41:52.763Z 0.

[163] Johannes Markkanen and Alex J. Yuffa. Fast superposition T-matrix solution for clusters with arbitrarily-shaped constituent particles. *Journal of Quantitative Spectroscopy and Radiative Transfer*, 189:181–188, March 2017. GSCC: 0000093 2025-06-09T13:44:32.769Z 0.

[164] Johannes Markkanen, Jessica Agarwal, Timo Väisänen, Antti Penttilä, and Karri Muinonen. Interpretation of the Phase Functions Measured by the OSIRIS Instrument for Comet 67P/Churyumov–Gerasimenko. *The Astrophysical Journal Letters*, 868(1):L16, November 2018. Publisher: The American Astronomical Society.

[165] Yuna G. Kwon, Stefano Bagnulo, Johannes Markkanen, Ludmilla Kolokolova, Jessica Agarwal, Manuela Lippi, and Zuri Gray. The Pre-perihelion Evolution of the Activity of Comet C/2017 K2 (Pan-STARRS) during the Water Ice-line Crossover. *The Astronomical Journal*, 168(4):164, September 2024. Publisher: The American Astronomical Society.

[166] Yu Skorov, V Reshetnyk, J Markkanen, S Mottola, W Macher, O Mokhtari, N Thomas, M Küppers, and P Hartogh. Properties of the gas escaping from a non-isothermal porous dust surface layer of a comet. *Monthly Notices of the Royal Astronomical Society*, 527(4):12268–12283, February 2024.

[167] Joseph W. Goodman. *Statistical Optics*. Wiley series in pure and applied optics. John Wiley & Sons Inc, Hoboken, New Jersey, second edition edition, 2015. GSCC: 0008276 2025-06-10T12:57:24.152Z 15.19.

[168] Pawel Ossowski, Andrea Curatolo, David D. Sampson, and Peter R. T. Munro. Accurate Representation of Microscopic Scatterers in Realistic Simulation of OCT Image Formation. In *2018 IEEE Photonics Conference (IPC)*, pages 1–2, September 2018. ISSN: 2575-274X.

[169] Ming Jian Cheng, Yuan Cong Cao, Kuan Fang Ren, Huan Zhang, and Li Xin Guo. Generalized Lorenz-Mie theory and simulation software for structured light scattering by particles. *Frontiers in Physics*, 12, February 2024. Publisher: Frontiers.

[170] Peter R. T. Munro. TDMS: an open source time domain Maxwell solver for simulating optical coherence tomography image formation. In Maciej Wojtkowski, Yoshiaki Yasuno, and Benjamin J. Vakoc, editors, *Optical Coherence Imaging Techniques and Imaging in Scattering Media V*, page 32, Munich, Germany, August 2023. SPIE. GSCC: 0000001 2025-06-11T18:21:04.811Z 0.01.

[171] P. Török, P. R. T. Munro, and Em E. Kriezis. High numerical aperture vectorial imaging in coherent optical microscopes. *Optics Express*, 16(2):507–523, January 2008. Publisher: Optica Publishing Group.

[172] A N Bashkatov, E A Genina, V I Kochubey, and V V Tuchin. Optical properties of human skin, subcutaneous and mucous tissues in the wavelength range from 400 to 2000 nm. *Journal of Physics D: Applied Physics*, 38(15):2543–2555, August 2005. GSCC: 0002190 2025-06-09T13:48:21.585Z 2.11.

[173] Alexey N. Bashkatov, Elina A. Genina, and Valery V. Tuchin. Optical properties of skin, subcutaneous, and muscle tissues: A review. *Journal of Innovative Optical Health Sciences*, 04(01):9–38, January 2011.

[174] W.F. Cheong, S.A. Prahl, and A.J. Welch. A review of the optical properties of biological tissues. *IEEE Journal of Quantum Electronics*, 26(12):2166–2185, December 1990. GSCC: 0004093 2025-06-09T13:41:21.395Z 0.

[175] Julia L. Sandell and Timothy C. Zhu. A review of *in-vivo* optical properties of human tissues and its impact on PDT. *Journal of Biophotonics*, 4(11-12):773–787, November 2011.

[176] Steven Jacques. Generic tissue optical properties, February 2015.

[177] Scott Prahl. Mie Scattering Calculator.

[178] Christian Matzler. MATLAB functions for Mie scattering and absorption. *IAP Res Rep*, 8, July 2002.

[179] Brian W. Pogue and Michael S. Patterson. Review of tissue simulating phantoms for optical spectroscopy, imaging and dosimetry. *Journal of Biomedical Optics*, 11(4):041102, 2006. GSCC: 0001116 2025-06-09T13:50:22.959Z 1.10.

[180] Scott A. Prahl. Everything I think you should know about Inverse Adding-Doubling. *Oregon Medical Laser Center, St. Vincent Hospital*, 1344:1–74, 2011. GSCC: 0000185 2025-06-09T13:44:25.937Z 0.25.

[181] Scott A. Prahl, Martin J. C. Van Gemert, and Ashley J. Welch. Determining the optical properties of turbid media by using the adding–doubling method. *Applied Optics*, 32(4):559, February 1993. GSCC: 0001208 2025-06-09T13:43:43.854Z 0.72.

[182] Jason R. Cook, Richard R. Bouchard, and Stanislav Y. Emelianov. Tissue-mimicking phantoms for photoacoustic and ultrasonic imaging. *Biomedical Optics Express*, 2(11):3193–3206, November 2011. Publisher: Optica Publishing Group.

[183] Janek Gröhl, Thomas R. Else, Lina Hacker, Ellie V. Bunce, Paul W. Sweeney, and Sarah E. Bohndiek. Moving Beyond Simulation: Data-Driven Quantitative Photoacoustic Imaging Using Tissue-Mimicking Phantoms. *IEEE Transactions on Medical Imaging*, 43(3):1214–1224, March 2024.

[184] Tamara L. Troy and Suresh N. Thennadil. Optical properties of human skin in the near infrared wavelength range of 1000 to 2200 nm. *Journal of Biomedical Optics*, 6(2):167–176, April 2001. Publisher: SPIE.

[185] J. R. DeVore. Refractive indices of Rutile and Sphalerite. *Journal of the Optical Society of America*, 41(6):416, June 1951. GSCC: 0001122 2025-06-09T13:50:14.996Z 0.29.

[186] Yugong Wu, Zhigang Fan, and Yuzhu Lu. Bulk and interior packing densities of random close packing of hard spheres. *Journal of Materials Science*, 38(9):2019–2025, May 2003.

[187] Aleksi A Leino, Aki Pulkkinen, and Tanja Tarvainen. ValoMC: a Monte Carlo software and MATLAB toolbox for simulating light transport in biological tissue. *OSA Continuum*, 2(3):957, March 2019. GSCC: 0000109 2025-06-10T12:59:20.105Z 0.33.

[188] Steven L. Jacques. Origins of Tissue Optical Properties in the UVA, Visible, and NIR Regions. In *Advances in Optical Imaging and Photon Migra-*

tion (1996), paper OPC364, page OPC364. Optica Publishing Group, March 1996.

[189] I. M. Vellekoop and A. P. Mosk. Universal optimal transmission of light through disordered materials. *Physical Review Letters*, 101(12):120601, September 2008. GSCC: 0000498 2025-06-10T12:59:15.520Z 0.57.

[190] Zhipeng Yu, Huanhao Li, and Puxiang Lai. Wavefront Shaping and Its Application to Enhance Photoacoustic Imaging. *Applied Sciences*, 7(12):1320, December 2017. Publisher: Multidisciplinary Digital Publishing Institute.

[191] Ori Katz, Eran Small, and Yaron Silberberg. Looking around corners and through thin turbid layers in real time with scattered incoherent light. *Nature Photonics*, 6(8):549–553, August 2012. GSCC: 0000663 2025-06-09T13:46:38.129Z 0.

[192] J. M. Schmitt, R. T. Wall, G. X. Zhou, and E. C. Walker. Multilayer model of photon diffusion in skin. *Journal of the Optical Society of America A*, 7(11):2141, November 1990. GSCC: 0000315 2025-06-11T18:20:36.955Z 0.17.

[193] Jung-Hoon Park, Zhipeng Yu, KyeoReh Lee, Puxiang Lai, and YongKeun Park. Perspective: Wavefront shaping techniques for controlling multiple light scattering in biological tissues: Toward *in vivo* applications. *APL Photonics*, 3(10):100901, October 2018. GSCC: 0000095 2025-06-09T13:49:09.508Z 0.27.

[194] D. W. Mackowski. The extension of the Multiple Sphere T Matrix code to include multiple plane boundaries and 2-D periodic systems. *Journal of Quantitative Spectroscopy and Radiative Transfer*, 290:108292, November 2022.

[195] Marco Leonetti. Speckle Autocorrelation, September 2025.

[196] Bradley E. Treeby and B. T. Cox. k-Wave: MATLAB toolbox for the simulation and reconstruction of photoacoustic wave fields. *Journal of Biomedical Optics*, 15(2):021314, 2010.